5-2007

Adaptive Treatment of van der Waals Interactions in Empirical Bond-Order Potentials with Application to Junction Formation in Carbon Nanotubes

Aibing Liu
Clemson University, aliu@clemson.edu

ADAPTIVE TREATMENT OF VAN DER WAALS INTERACTIONS IN EMPIRICAL BOND-ORDER POTENTIALS WITH APPLICATION TO JUNCTION FORMATION IN CARBON NANOTUBES

A Dissertation
Presented to
the Graduate School of
Clemson University

In Partial Fulfillment
of the Requirements for the Degree
Doctor of Philosophy
Chemistry

---

by
Aibing Liu
May 2007

Accepted by:
Dr. Steven J. Stuart, Committee Chair
Dr. Arkady Kholodenko
Dr. Robert Latour
Dr. Brian Dominy

ABSTRACT

Molecular dynamics (MD) simulation of reactive condensed-phase hydrocarbon systems is a challenging research area. The AIREBO potential is particularly useful in this area because it can simulate bond breaking and bond forming during chemical reactions. It also includes non-bonded interactions for systems with significant intermolecular interactions.

The first part of this dissertation describes a method to adaptively incorporate van der Waals interaction of carbon atoms into the AIREBO force field. In bond-order potentials, the covalent bonding interactions adapt to the local chemical environment, allowing bonded interactions to change in response to local chemical changes. Non-bonded interactions should adjust to their chemical environment as well, although this adaptivity has been somewhat limited in previous implementations. Here the AIREBO potential is extended to include an adaptive Lennard-Jones potential, allowing the van der Waals radius and well depth to vary adaptively in response to chemical reactions. The resulting potential energy surface and its gradient remain continuous, allowing it to be used for dynamics simulations. This new potential is parameterized for hydrocarbons, and is fit to the energetics and densities of a variety of condensed phase molecular hydrocarbons. The resulting model is more accurate for modeling aromatic and other unsaturated hydrocarbon species, for which the original AIREBO potential had some deficiencies. Testing on compounds not used in the fitting procedure shows that the new model performs substantially better in predicting heats of vaporization and pressures (or densities) of condensed-phase molecular hydrocarbons.

The second part of this dissertation describes the investigation of nanotube welding by ion bombardment. Nanotube technology has found many applications in recent years. Junctions between heterostructured nanotubes are of particular interest be-

cause of their possible application in nanoscale devices. Simulation is performed on the formation of junctions by Ar ion irradiation of nanotubes using the AIREBO force field. Two groups of nanotubes are used in this research. One includes larger nanotubes of diameter 13 Å, another includes smaller nanotubes of diameter about 7-8 Å. Nanotube junction formation under different bombardment ion energies is explored. In both large and small nanotubes, junctions can be formed by ion irradiation. It is found that for large nanotubes, high energy impacts are needed in order to form junctions. Smaller nanotubes are badly damaged by high energy ions. The different types of defects created by ion impact are also investigated. Cross-links in the nanotube intersection are used as a primary index of junction formation. A comparison of longer relaxation and cooling times is also performed. The evaluation of conductivity of nanotube junctions during simulation is explored. For (10,0) nanotubes, conductance across the junction becomes non-zero after the first impact for 330 eV energy impact.

DEDICATION

I dedicate this thesis to my loving wife. Without her support and understanding, this work would not have been completed.

ACKNOWLEDGEMENTS

Working in a Ph.D program is certainly not an easy task. Fortunately, I got a lot of help from the people around me.

I would like to thank my advisor, Dr. Stuart, for guiding me to this interesting research field, and handing me the tools to a higher level of thinking. He give me the freedom of choosing my interest area and kept me on track of research. He works with me when I am in need, and helps me out of dead ends. I have learned a lot from him in this long process.

I also want to thank members of our research group. I really enjoyed working with each one of you, especially Brad Dickson. During this period of Ph.D program, Brad helped me in understanding new ideas. Discussions with him really open up my mind. A lot of tips in research and writing are learned from Brad. Yang Li, the system administrator, solved computer related problems and saved me much time.

Dr. Vincent Meunier from Oak Ridge National Lab has also played an important role in my thesis. Most of the conductivity work has been done with his help. He gave me good advice on how to process data. It has been a pleasure working with Dr. Meunier.

I would like to express my gratitude to my parents, who are always believe in me, always supportive to my life. They always encourage me to reach a higher level.

Finally to my wife, who did all little things in life. Without her support, it would be impossible to accomplish this.

TABLE OF CONTENTS

Table of Contents (Continued)

LIST OF TABLES

LIST OF FIGURES

List of Figures (Continued)

Figure Page

List of Figures (Continued)

Figure Page

List of Figures (Continued)

Figure Page

Figure Page

CHAPTER 1
INTRODUCTION

Molecular Dynamics Simulation

Molecular dynamics (MD) is a computer simulation technique. It uses classical mechanics to calculate the force between particles in a system. The first thing a molecular dynamics simulation needs is a force field or potential describing interactions. The force field could be as simple as the hard sphere model, or as complex as quantum calculation. The choice depends on what system is investigated and what accuracy the simulation needs. After choosing an appropriate potential, the simulation system needs to be set up. Every particle in the system is assigned a coordination (x,y,z) and a velocity (v_x, v_y, v_z). Knowing position of particles, the potential energy (V) can be calculated from the force field. The force on each particle is determined from the gradient of the potential energy:

$$F_i = -\frac{\partial V}{\partial x_i} \tag{1.1}$$

where F_i is the force on atom i. According to Newton's law of motion, the acceleration of each particle is the derivative of the force:

$$a_i = \frac{F_i}{m_i} \tag{1.2}$$

In a small time step, the acceleration and velocity of particle can be seen as constant. Thus after one time step Δt, the new coordination of the particle is:

$$x_{i+1} = x_i + v_i \cdot \Delta t \tag{1.3}$$

The new velocity of particle becomes

$$v_{i+1} = v_i + a_i \cdot \Delta t \tag{1.4}$$

From this new set of coordination and velocity, the calculation can go on to the next step until the end of simulation. Usually the time step used in MD simulation is less than 1 fs.

AIREBO Force Field

The AIREBO force field was developed by Steven Stuart and Judith Harrison in 2000[1]. It is a further developentment of the reactive empirical bond-order potential (REBO). The REBO potential is used in simulations of hydrocarbon systems. The difference between REBO potential and molecular mechanics potentials lies in that chemical reactions can be simulated in REBO potential. Bond breaking and bond forming are described by a Tersoff-type potential[5, 6].

The bond-order potential, originally proposed by Tersoff, provides a method for classical simulations of covalently reactive systems, such as silicon and carbon. In these potentials, the interaction between two atoms is represented as the combination of a repulsive and an attractive interaction,

$$V_{ij}(r) = V_{ij}^R + b_{ij} V_{ij}^A, \tag{1.5}$$

where the relative strength of these two terms is controlled by the bond order, b_{ij}. The bond order is a many-body term that depends on the local chemical environment, including coordination numbers and bond angles, and enables the strength of the covalent bond between atoms i and j to vary adaptively in response to changes in the bonding environment. As with embedded-atom models[7], each individual bond weakens as the atoms participating in the bond acquire more neighbors, since their valence electrons are divided among more bonding interactions. However, the bond-order potentials also treat the dependence of the bond energy upon the angular distribution of neighbors — a term which is crucial for the directional bonding found in covalent materials.

This approach has been particularly fruitful for modeling carbon and hydrocarbons, and there have been a number of parameterizations of bond-order potentials for hydrocarbon systems. Following the original Tersoff model[8], Brenner developed

the REBO model[9], which has been widely used. Pettifor has shown that the potential energy expressions used in these empirical bond-order models is equivalent to one that can be derived from orthogonal tight-binding models in the second-moment approximation[10], and has developed analytical bond-order potentials that go beyond this approximation[11].

The REBO potential has been used successfully in simulation of many different materials and processes, including carbon nanotubes[12], tribology of diamond surfaces[13], and fullerenes[14]. But the REBO potential is not suitable for every hydrocarbon system. It does not include intermolecular interactions, making it a poor choice for systems with significant intermolecular interactions. This includes liquid and thin film systems.

The AIREBO model extends the REBO model to include non-bonded interactions, including van der Waals terms. These intermolecular interactions are crucial for modeling condensed-phase molecular systems, or the non-covalent interactions between layers in graphitic materials. The AIREBO potential has been used in simulation of friction on alkane monolayer[15], amorphous carbon[16], and hydrogen adsorption on nanotubes[17].

Van der Waals Interaction

The van der Waals interaction is the dispersion force and repulsion force between non-bonded atoms and molecules. It is the main force between particles in noble gases and non-polar compounds. It holds molecules together in the liquid state. Without van der Waals interaction, noble gases would not liquify.

The Lennard-Jones(LJ) potential is one of the approximate models of the van der Waals interaction. It was proposed by John Lennard-Jones of Bristol University in 1931[18]. The most common mathematical form of the LJ potenial is in equation 1.6:

$$V(r) = 4\epsilon \left[\left(\frac{\sigma}{r}\right)^{12} - \left(\frac{\sigma}{r}\right)^{6} \right] \tag{1.6}$$

It is also called the 12-6 potential. The parameter ϵ is the depth of the potential well, while σ is related to the size of the atom. The r^{-12} term models the repulsive

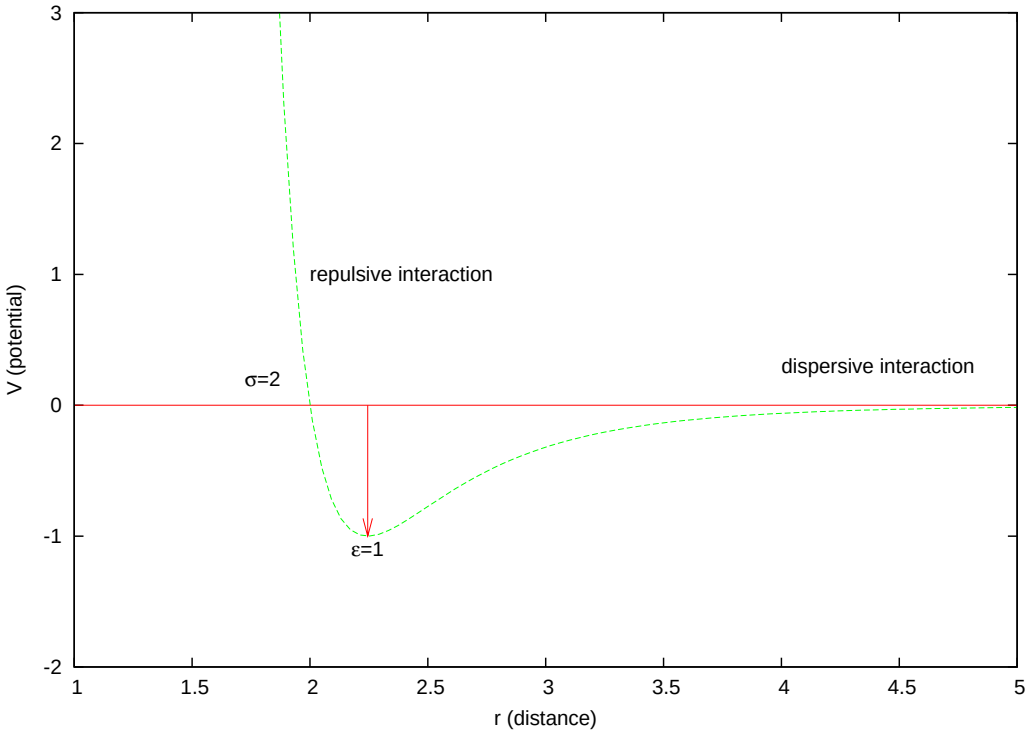

Figure 1.1 Lennard-Jones potential with $\sigma = 2$ and $\epsilon = 1$.

interaction in short diatance. It increases rapidly as the distance between molecules shorten. This repulsive interaction originates from electronic orbital overlap. It is the result of Pauli exclusion principle. The r^{-6} term models the dispersive interaction at long distance. The dispersion force is also called the London force. It is the attractive force between molecules. Dispersion force arises from the fluctuation of dipole moments and multipole moments. This is weak interaction,but it keeps particles close in condensed phase. The advantage of the LJ equation lies in its simplicity and efficiency in calculation because r^{12} is the square of r^6.

A graph of this potential is shown in Fig. 1.1.

Introduction to Carbon Nanotube

One of the biggest discovery in the 1990s was carbon nanotube materials. These were first discovered by Iijima in 1991[19]. There are two types of nanotubes: single wall nanotube (SWNT) and multi wall nanotube (MWNT). The first nanotube found is MWNT. SWNT was discovered two years later[20, 21]. Since then, great progress has been made in the past fifteen years. Due to their unique properties, nanotubes

have become a central area of chemistry research. A carbon nanotube can be visualized as a sheet of graphite rolled into a cylinder. Depending on how it is rolled, it is named following this method. As shown in Figure 1.2 (a), the naming of nanotube is determined by two vectors: a_1 and a_2 shown in blue. The composite vector rolling the sheet is a summation of these two vertors:

$$C = n\vec{a}_1 + m\vec{a}_2 \tag{1.7}$$

when $n = m$, the nanotube is named (n,n), an armchair nanotube. When $m = 0$, it is (n,0), a zigzag nanotube. In all the other cases, they are chiral nanotubes. Graph b, c, d in Figure 1.2 are examples of these three type of nanotubes.

One of the interesting features of carbon nanotubes is their electronic properties. Carbon nanotubes can be metallic or semiconducting, depending on their diameters and the helicity of the arrangement of graphene rings in their walls.[22] Zigzag (n,0) SWNTs have two types of electronic behaviour depending on the value of n: they are metallic if $n/3$ is an integer or semiconducting otherwise. Chiral (n,m) SWNTs are similar to the zigzag nanotubes: metallic when $(2n+m)/3$ is integer and otherwise semiconducting. All armchair (n,n) SWNTs are metallic. The band gap for the semiconducting nanotubes decreases with increasing diameter d.

In the following chapters, two simulations using AIREBO force field was conducted. In chapter 2, an adaptive treatment of van der Waals interaction in LJ 12-6 form was developed. An improvment in liquid property prediction was observed in testing compounds. In chapter 3, nanotube junction formation simulation was condcuted using AIREBO force field. Effect of ion bombardment energy on junction formation and conductivity of nanotube junctions were investigated.

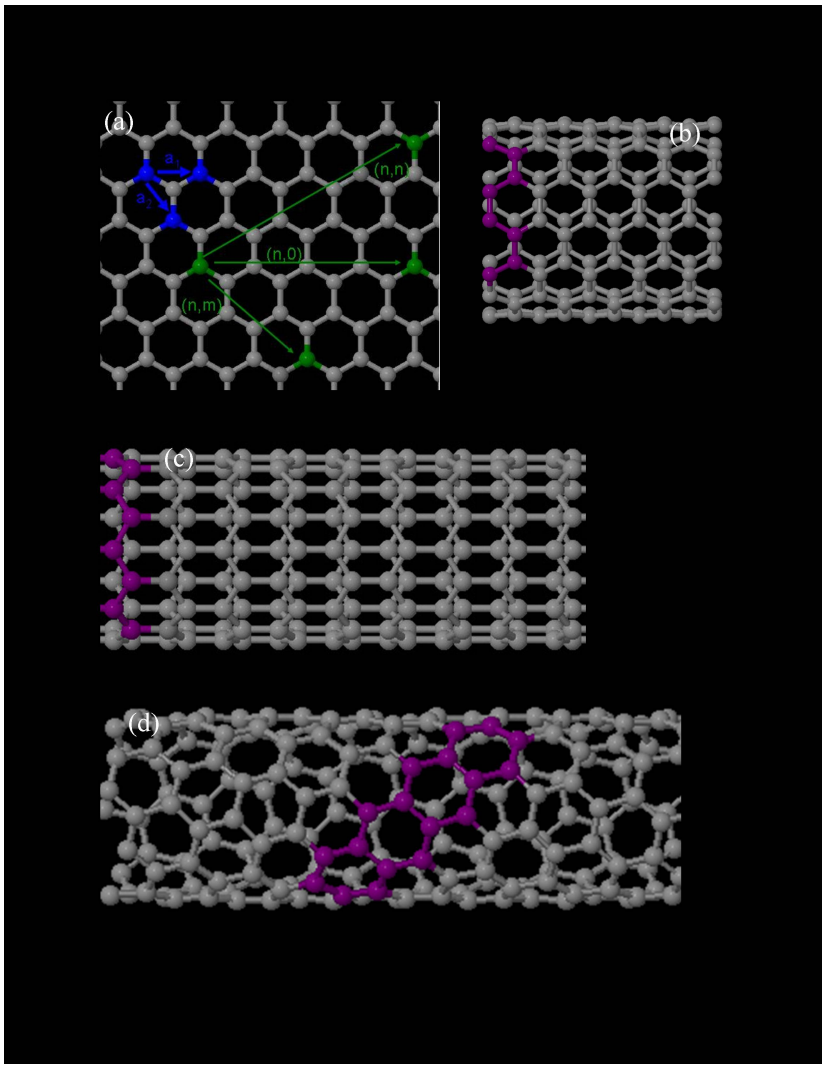

Figure 1.2 Different nanotubes. (a) shows the naming of nanotubes based on how they are rolled from a graphene sheet. (b) is an example of a armchair nanotube (n,n). (c) is an example of a zigzag nanotube (n,0). (d) is a chiral nanotube(n,m).

CHAPTER 2

ADAPTIVE TREATMENT OF VAN DER WAALS INTERACTIONS

Introduction

The van der Waals interactions are treated adaptively in the AIREBO potential, allowing the interaction to be switched off smoothly as the chemical environment changes and a non-bonded pair becomes bonded[1]. But although the strength of the van der Waals interactions responds adaptively to the local environment, the form of that interaction does not. I.e., the van der Waals radius and magnitude of the dispersion interaction do not vary with changes in hybridization to reflect changes to the size or polarizability of the electrons which give rise to the van der Waals interaction; a single parameterization of the van der Waals energy expression is used for all interactions. Consequently, the van der Waals interactions in the original AIREBO potential are not as transferable across different hydrocarbon hybridizations as would be desired. Here we describe an extension of the AIREBO potential to allow the parameterization of the van der Waals interaction to change adaptively with the chemical environment of the interacting atoms. This is done by having the coefficients of the Lennard-Jones 12-6 expression for the van der Waals interaction depend parametrically on the coordination number of the interacting atoms.

The rest of this chapter is organized as follows. In section we present the modifications to the AIREBO model. Section describes the details of the fitting procedure used to reparameterize the potential. Finally, in section we discuss the application of this potential to some hydrocarbons not included in the fitting database.

Model

The van der Waals interactions represent the combination of attractive dispersion interactions and repulsive exchange interactions. There are many functional forms used to represent these van der Waals interactions in molecular simulations; the form used in the AIREBO potential is the Lennard-Jones (LJ) 12-6 form,

$$V_{ij}^{\mathrm{LJ}}(r) = 4\epsilon_{ij}\left[\left(\frac{\sigma_{ij}}{r_{ij}}\right)^{12} - \left(\frac{\sigma_{ij}}{r_{ij}}\right)^{6}\right] \tag{2.1}$$

where r_{ij} is the distance between atoms i and j, and V_{ij} is the potential energy of their interaction. The computational advantages of using this form (only two parameters, no unphysical turnover, computational efficiency) outweighed the increased accuracy that can be obtained from different functional forms.[23] The infinitely repulsive r^{-12} core has been replaced by more physically realistic potentials with finite cores when using AIREBO for high-energy collisions.[24] This repulsive core — whether infinite or merely strong — is treated adaptively in the AIREBO potential, so that the repulsive interactions are diminished between reactive or covalently bound atoms, but is undiminished for chemically saturated atoms. The total van der Waals interaction included in the potential is thus

$$E_{ij} = \alpha V_{ij}^{\mathrm{LJ}}(r) \tag{2.2}$$

where the many-body term α is a function not only of the bond distance r, but also the bond order between i and j, as well as the position of all first neighbors bonded to atoms i and j.[1] Neither the LJ 12-6 functional form nor the means of making the repulsive interactions adaptive is modified in the current work. Rather, we confine our attention to the variability of the LJ ϵ and σ parameters (or the underlying polarization and radius of the electron cloud) with chemical environment.

The σ_{ij} and ϵ_{ij} parameters characterize the van der Waals interaction between atom types i and j. These determine many of the material properties for soft, molecular systems, such as their cohesive energy, boiling point, density, etc. Consequently, most *non-reactive* force fields, such as CHARMM[25], UFF[26], AMBER[27], MM3[28] and COMPASS[29, 30], utilize different ϵ and σ values for different "types"

of carbon atoms. These atom types can be distinguished by their hybridization state (sp^2 vs. sp^3 carbon) or by their bonding environment (an sp^2 carbon in a carbonyl group or an alkene bond or a conjugated system), and can extend to dozens of different atom types for a single atomic number. The physical basis for distinguishing between atoms in different chemical environments is, of course, that the chemical environment influences the electronic distribution on the atom, and the size and polarizability of this electron could affect the exchange and dispersion interactions. In a reactive potential such as AIREBO, however, hybridization state and bonding environment are free to change, and all carbon atoms must be treated with the same potential. Consequently, the original AIREBO potential used only a single σ and ϵ value for each atom, neglecting any variation in the shape of the van der Waals potential with bonding environment. In the original AIREBO potential, the σ_{CC} and ϵ_{CC} parameters were obtained by fitting to the interlayer spacing and elastic constant of graphite, while σ_{HH} and ϵ_{HH} were determined by fitting to the pair correlation function of liquid-state methane and ethane. (The heterogeneous parameters, σ_{HC} and ϵ_{HC}, are determined from the Lorentz-Berthelot combining rules.[31]) One result of this fitting procedure has been that the AIREBO potential provides a better description of the saturated molecular hydrocarbons for which it was fit than for unsaturated species. For example, the fine detail in the liquid structure of ethylene is not reproduced well by the AIREBO model (see Figure 2.1).

If the performance of the AIREBO potential is to be improved in this regard, it is necessary to allow the shape of the van der Waals potential to adapt in response to changes in the local bonding environment. The approach taken here is to treat the σ_{CC} and ϵ_{CC} terms as functionally dependent on the bonding environment, rather than as unvarying constants. In the nonpolar, hydrocarbon systems for which AIREBO has been parameterized, the electron distribution on the s-valent hydrogen atom is assumed not to change substantially in different environments, and so the σ_{HH} and ϵ_{HH} values remain constant. At a mininum, the LJ parameters for carbon should depend on the hybridization state of the carbon atom, which determines to a large degree the size and character of the atom's electron distribution. In addi-

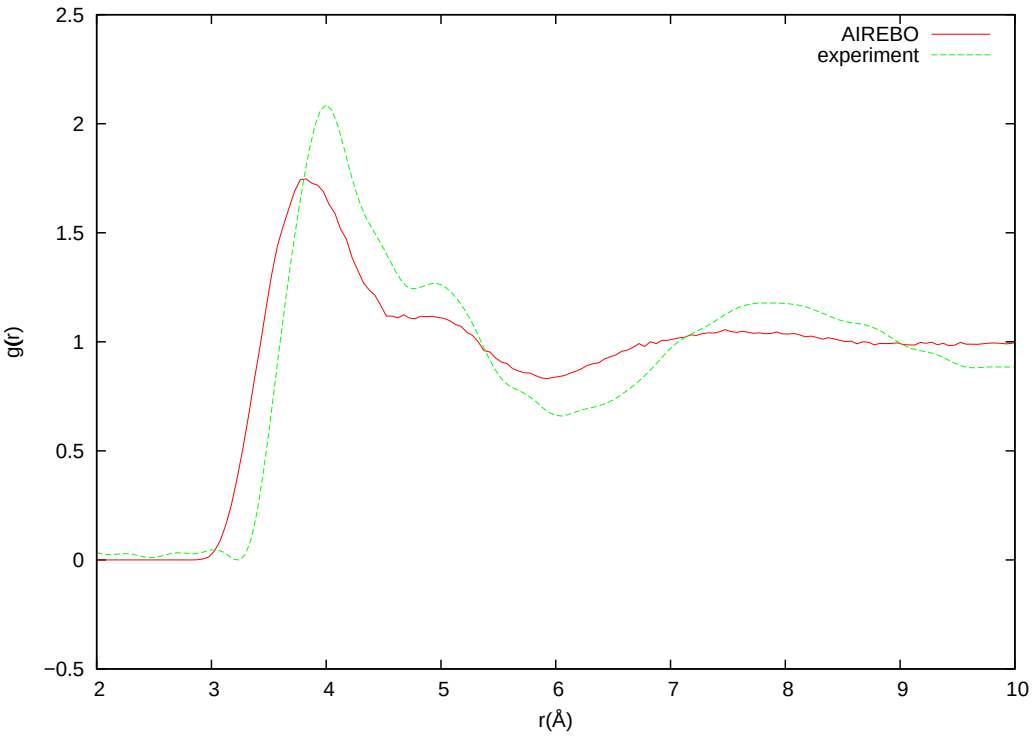

Figure 2.1 Carbon-carbon pair correlation function g_{CC} for liquid ethylene at 106 K. Experimental result from Ref.[2]

tion, these parameters should also depend on the type of atoms to which the carbon atom is bonded. Bonds with different polarity and different length will give rise to different nonbonded interactions. Although both C–C and C–H bonds are nonpolar, they have very different lengths. Thus, since the bond order potentials use coordination number as a proxy for hybridization state, the σ and ϵ values for carbon can be assumed to depend on the number of carbon and hydrogen neighbors of the carbon atom in question: $\sigma_C(N^C, N^H)$ and $\epsilon_C(N^C, N^H)$,rather than constant values that are independent of their bonding environment. A physical basis could also be provided for even more complex features of the chemical environment, such as the number and identity of second neighbors. This approach may prove to be necessary with the introduction of heteroatoms, as is the case with many classical, nonreactive force fields.[25, 27, 28] However, these effects are neglected in the current model. It might be expected that the LJ parameters should also depend on the degree of local conjugation; the π-bonding electrons on an unsaturated carbon may give rise to very

different van der Waals interactions depending on whether they are localized and relatively nonpolarizable, as in an olefin, or delocalized and more polarizable, as in benzene or graphite. A dependence of the LJ parameters on local conjugation was considered, but was found not to be necessary. The parameters for conjugated and nonconjugated sp^2 carbons were found to be quite similar, as described below, so the extra complexity of this additional environmental dependence was abandoned.

In these reactive, bond-order potentials, the coordination numbers N^C and N^H are not integer quantities, as in a nonreactive potential, but take on fractional values, varying smoothly over the course of a reaction.[9, 1] Consequently, the functions $\sigma_C(N^C, N^H)$ and $\epsilon_C(N^C, N^H)$ need to be defined for non-integer arguments. It is highly impractical to fit such a function for LJ parameter values at non-integer values of N^C and N^H, both because there is no unambiguous method of assigning non-integer coordination numbers to a partially dissociated bond, and because there are no appropriate experimental or even *ab initio* data which can be used to fit the van der Waals interactions for such transient and unstable systems. Consequently, we have chosen to implement the functional dependence of the Lennard-Jones parameters on coordination number via a bicubic spline,[32] in which a knowledge of the function (and some of its derivatives) at integer knot points can be used to generate a smooth function that can be interpolated for non-integer arguments. The integer knot points correspond to stable molecular species, for which the function can be parameterized with experimental data.

Thus we take

$$\sigma_C(N^C, N^H) = \sum_{k=0}^{3} \sum_{l=0}^{3} c_{kl}^{\sigma} (N^C)^k (N^H)^l \tag{2.3}$$

and

$$\epsilon_C(N^C, N^H) = \sum_{k=0}^{3} \sum_{l=0}^{3} c_{kl}^{\epsilon} (N^C)^k (N^H)^l. \tag{2.4}$$

where the $\{c_{kl}^{\sigma}\}$ and $\{c_{kl}^{\epsilon}\}$ coefficients are defined within a rectangular region in which $N_{min}^C < N^C < N_{max}^C$ and $N_{min}^H < N^H < N_{max}^H$; i.e., within a region bounded by four spline knot points at $(N^C, N^H) = (N_{min}^C, N_{min}^H)$, (N_{min}^C, N_{max}^H), (N_{max}^C, N_{min}^H), and (N_{max}^C, N_{max}^H). The sixteen coefficients $\{c_{kl}\}$ in Eqs 2.3 and 2.4 can thus be

determined by specifying the value of the function and three of its derivatives at each of the four knot points. In a different region, the function σ_C or ϵ_C is determined similarly, but with a different set of coefficients. The continuity of the function and its gradient are ensured at the boundary through the shared spline knot points at that boundary. Here we use integer values of N^C and N^H as the knot points, and require that

$$\frac{\partial \sigma_C}{\partial N^C} = \frac{\partial \sigma_C}{\partial N^H} = \frac{\partial^2 \sigma_C}{\partial N^C \partial N^H} = 0 \tag{2.5}$$

and

$$\frac{\partial \epsilon_C}{\partial N^C} = \frac{\partial \epsilon_C}{\partial N^H} = \frac{\partial^2 \epsilon_C}{\partial N^C \partial N^H} = 0 \tag{2.6}$$

at each of the knot points. This is done to ensure that there are no forces arising from a nonzero slope such as $\frac{\partial \sigma_C}{\partial N^C}$ for stable molecules with integer coordination numbers, and also because of a lack of experimental information that correlates to these derivatives. The values of σ_C and ϵ_C at knot points (integer number of bonded neighbors) are obtained by fitting to the cohesive energies and density for liquids of small molecular hydrocarbons, as described in the following section. To do this fitting, we make use of the fact that for a stable, nonreactive system (such as a hydrocarbon liquid at sub-pyrolytic temperatures) the coordination number for each atom is an integer, and the van der Waals interactions in the liquids are determined only by the σ and ϵ values at the knot points. Thus these simulations can be performed without knowledge of all of the coefficients in Eqs. 2.3 and 2.4, and thus before the σ_C and ϵ_C values have been obtained at all knot points.

The strength of the reactive bond-order potentials, however, lies in their ability to simulate chemical reactions. During these reactions, the coordination numbers will be non-integer and the bicubic splines will be evaluated away from the knot points. Thus the full Lennard-Jones interaction is evaluated as in Eq. 2.1, where the interatomic σ_{ij} and ϵ_{ij} parameters are obtained from the single-atom values using the Lorentz-Berthelot combining rules[31],

$$\sigma_{ij} = \frac{1}{2}(\sigma_i + \sigma_j) \tag{2.7}$$

and

$$\epsilon_{ij} = \sqrt{\epsilon_i \epsilon_j}, \tag{2.8}$$

and σ_C and ϵ_C are now calculated from Eqs. 2.3 and 2.4 for the case where i or j is a carbon atom.

One important difference worth mentioning is that for COMPASS and all non-reactive force fields, the type of carbon will not change during simulation. But for AIREBO simulations, which usually involve reactions, carbons in the system will not always remain the same. There is only one carbon type. But in different chemical environments, carbons have different LJ parameters.

Equations 2.3 and 2.4 thus represent the only modification to the AIREBO potential in the current work, and the coefficients needed to parameterize this equation are obtained in the following section. It is worth commenting also on how this minor change affects the calculation of forces under the new potential. The forces are calculated from the negative gradient of the potential in the usual manner, so that the force on atom m in the Cartesian direction β ($\beta = x$, y, or z) is

$$F_{i\beta}^{\mathrm{LJ}} = -\frac{\partial}{\partial \beta_i} \sum_m \sum_{n<m} V_{mn}^{\mathrm{LJ}}, \tag{2.9}$$

where V_{mn}^{LJ} is given by Eq. 2.1 and we are ignoring all of the contributions to the force from non-van der Waals terms in the potential. The Lennard-Jones potential as traditionally implemented is a function only of the interatomic distance, so the Lennard-Jones contribution to the force is evaluated simply as

$$F_{i\beta}^{\mathrm{LJ}} = -\sum_{j \neq i} \frac{\partial V_{ij}^{\mathrm{LJ}}}{\partial r_{ij}} \frac{\partial r_{ij}}{\partial \beta_i}. \tag{2.10}$$

In the new model, however, the van der Waals potential depends on the atomic positions not only explicitly through the i–j bond length, but also implicitly via the ϵ and σ parameters. Thus the force becomes

$$F_{i\beta}^{\mathrm{LJ}} = -\sum_{n<m} \left[\frac{\partial V_{mn}^{\mathrm{LJ}}}{\partial r_{mn}} \frac{\partial r_{mn}}{\partial \beta_i} + \frac{\partial V_{mn}^{\mathrm{LJ}}}{\partial \sigma_{mn}} \frac{\partial \sigma_{mn}}{\partial \beta_i} + \frac{\partial V_{mn}^{\mathrm{LJ}}}{\partial \epsilon_{mn}} \frac{\partial \epsilon_{mn}}{\partial \beta_i} \right]. \tag{2.11}$$

Now, because of the dependence of σ_{mn} and ϵ_{mn} on the coordination numbers of atoms m and n, the double sum must run not only over all pairs of atoms involving the atom

i in question, but also over all pairs k–j where k is at least partially bonded to i (such that displacing i will change the coordination number of k and thus alter σ_{kj} and ϵ_{kj}). Please see appendix A for a detailed discussion of the derivatives included in Eq. 2.11.

Parameterization

Simulation Details

In order to perform the parameterization, molecular dynamics simulations were performed for a variety of small molecular hydrocarbons in the liquid state. These compounds ranged from one to four carbons in size, and included both saturated hydrocarbons, as well as unsaturated carbons with sp and sp^2 hybridization, including both conjugated and non-conjugated molecules. A complete list of the nine molecules used to do the fitting is provided in Table 2.1. Each molecular dynamics simulation consisted of 128 molecules in a periodic simulation cell at the experimental density, except for one case (methane) where 256 molecules were used in order that the side length of the periodic cell would exceed twice the LJ cutoff ($3\sigma_{CC}$). When experimental data for the enthalpy of vaporization were available, the simulations were performed at the experimental boiling point of the system, T_b (or 298 K, if $T_b > 298$ K, as for benzene). If $\Delta_{\text{vap}}H$ was not available at T_b, the simulation was performed at 298 K. The specific temperatures used for each compound, along with the experimental density and $\Delta_{\text{vap}}H$, are provided in Table 2.1. The simulations were performed in the canonical (NVT) ensemble, using the Langevin thermostat[33]. Long-range corrections[34] were used to account for the van der Waals energy contributions beyond the LJ cutoff of 3σ. The simulations were run for a minimum of 100 ps after equilibration at the desired temperature, although frequently for as long as 200 ps in order to obtain adequate statistical averaging of the system pressure. The simulated properties used to fit the LJ potential are the pressure, P, and the enthalpy of vaporization, $\Delta_{\text{vap}}H$. Because the systems are simulated at the correct experimental density at ambient pressure, a well-parameterized potential should give a pressure of 1 bar, while the target value for Δ_{vap} is obtained from experiment. The pressure is

compound	T(K)	ρ (g cm^{-3})	experiment	AIREBO[1]			this work		
			$\Delta H_{\rm vap}$ (kJ/mol)	$\Delta H_{\rm vap}$ (kJ/mol)	err(%)	P(bar)	$\Delta H_{\rm vap}$ (kJ/mol)	err(%)	P(bar)
benzene	298	0.8765[a]	33.83[a]	28.84	-14.75	1070	33.64	-0.56	-4.6
methane	111.7	0.4228[a]	8.17[a]	9.55	16.89	-381	8.15	-0.24	-19.9
ethane	184.6	0.5446[a]	14.69[a]	16.26	10.61	476	14.7	0	15.3
ethylene	169.45	0.5678[a]	13.54[a]	12.5	-7.68	399	13.54	0	15.3
acetylene	189.6	0.613[a]	16.95[b]	8.9	-47.49	851	16.9	-0.29	26.3
propane	231.1	0.584[b]	19.04[a]	19.45	2.15	451	18.99	-0.26	64.9
propadiene	240	0.6575[a]	18.42[b]	17.52	-4.88	417	18.46	0.22	0.01
isobutane	262	0.5934[b]	21.30[a]	22.32	4.78	204	21.31	0.05	-2.56
MAD					13.6	531.1		0.20	18.6

[a]Reference[35]
[b]Reference[36]

Table 2.1 Heats of vaporization and pressures as calculated with the new potential, with the original AIREBO potential[1], and as reported experimentally. The experimental pressure of each system at the specified state point is 1 bar. The mean absolute deviation (MAD) from experiment is provided for both properties.

calculated using the internal virial, while $\Delta_{\rm vap}H$ is calculated from the equilibrium energies of separate simulations of a single gas-phase molecule and an N-molecule simulation of the liquid at the same temperature,

$$\Delta_{\rm vap}H = NU(g) - U(l) + RT \tag{2.12}$$

where it has been assumed that the gas is ideal and the molar volume of the liquid is negligible compared to that of the gas.

Parameterization

In the original AIREBO potential, the LJ parameters for carbon were obtained from the properties of graphite. Thus we take these values, unmodified, as the LJ parameters for graphitic carbon, with $(N^C, N^H) = (3, 0)$, as well as for sp^2 carbon in a benzene-like environment of $(N^C, N^H) = (2, 1)$. At this point the only two remaining parameters needed in an unreactive simulation of liquid benzene are the values of σ_H and $\epsilon_{\rm H}$. These two parameters were modified to obtain the best fit to the experimental values of $\Delta_{\rm vap}H$ and P for benzene. Because the strong and monotonic dependence of energetic properties such as $\Delta_{\rm vap}H$ on ϵ and PV properties such as the pressure (or density) on σ, this optimization is relatively straightforward and results

in an unambiguous pair of (σ_H,ϵ_H) values. The values of σ and ϵ for hydrogen are 2.538 Å and 28.8 K, respectively. These values are assumed to apply for H atoms in any chemical environment.

Next, the values of (σ_C,ϵ_C) were determined in a like fashion, for one type of stable bonding environment at a time. This was done first for molecules containing carbon in only a single bonding environment: methane, ethane, ethylene and acetylene. Next, with (σ_C, ϵ_C) values in hand for the specific spline knots corresponding to these bonding environments, these values could be used in order to parameterize (σ_C, ϵ_C) values for additional spline knots using molecules such as propane or isobutene, which contain carbon in more than one different bonding environment. In all cases, each pair of experimental values of $\Delta_{\text{vap}}H$ and P for a specific liquid was used to fit only a single pair of (σ_C, ϵ_C) values at one knot point. The resulting parameter values are tabulated in Table 2.2.

The values of the heat of vaporization and pressure (at the experimental density) obtained during the parameterization procedure for the compounds used in the fitting process are presented in Table 2.1, along with the results obtained using the published AIREBO potential.[1] Because these properties were explicitly used during the fitting procedure, it is no surprise that they are well reproduced, with a mean absolute deviation (MAD) of 0.2% in the heat of vaporization and 20 bar in the pressure. The AIREBO values are presented merely as an illustration of the accuracy of the potential when not using adaptive LJ parameters, with MAD of 13% in the heat of vaporization and over 500 bar in the pressure.

Although the parameterization using the compounds in Table 2.1 is straightforward, there were some difficulties in the fitting process. One of these is that not all of the desired spline knot points can be easily parameterized from existing data. In some cases, the bonding environment corresponding to the knot point may be realistic, but the experimental or *ab initio* data may be hard to obtain. Such is the case for $N^C = 1$ and $N^H = 0$, corresponding to a C_2 dimer. This species exists, and is an important component in many reactive simulations, such as sputtering, but it is too reactive to exist in a condensed phase from which the van der Waals parame-

N_C	N_H	σ(Å)	$\epsilon(K)$	fitting compound
0	0	3.58	167.7	
0	1	4.13	75.1	
0	2	3.99	34.8	
0	3	3.12	15.6	
0	4	3.7	5.1	methane
1	0	3.05	157.14	
1	1	3.60	64.54	acetylene
1	2	3.46	24.3	ethylene
1	3	2.59	50.8	ethane
1	4	3.17	40.3	
2	0	2.85	125.6	propadiene
2	1	3.40	33.0	benzene
2	2	3.00	48.7	propane
2	3	2.13	75.2	
2	4	2.71	64.7	
3	0	3.40	33.0	
3	1	2.70	82.7	isobutane
3	2	2.30	98.4	
3	3	1.43	124.9	
3	4	2.01	114.4	
4	0	2.35	104.5	
4	1	1.65	154.2	
4	2	1.25	169.9	
4	3	0.38	196.4	
4	4	0.96	185.9	

Table 2.2 Knot values characterizing the bicubic spline for ϵ_C and σ_C at integer values of N^C and N^H. All derivatives of ϵ_C and σ_c with respect to N^C and N^H are zero at these knot points. The values were obtained by fitting to the specified compound, if present, or by extrapolation from nearby parameter values.

ters could be inferred. It is possible to imagine a series of *ab initio* calculations on a pair of C_2 dimers from which their van der Waals interaction potential could be obtained, although it would not be trivial to decouple this interaction from the covalent bonding interaction. The simpler approach used here is to arbitrarily specify values of σ_C and ϵ_C that preserve the general contour of the bicubic spline surface. Thus the parameters for the carbon dimer $(N^C, N^H = 1, 0)$ were obtained by linear extrapolation from the values for acetylene (1,1), propadiene (2,0), and benzene (2,1). In other cases, the bonding environment corresponding to one of the desired spline

knots may not be physically realistic. Such is the case for overcoordinated forms of carbon, such as $(N^C, N^H) = (2,3)$. Although there are no stable molecular species with this bonding configuration, such geometries may appear as transient states during energetic collisions. Furthermore, the parameter values at five-coordinate knot points may be needed to obtain values at non-integer coordination numbers, e.g. during an S_N2 reaction, even if the total coordination number never exceeds four during the reaction. Here it is difficult even to conceive of a realistic *ab initio* calculation that could provide realistic LJ parameters for such species. In this case also, the approach taken is to extrapolate from nearby parameter values. All extrapolated values chosen in this manner are specified in Table 2.2. It should be emphasized that although the LJ parameters obtained in this manner are somewhat arbitrary, they have little effect on any realistic simulations. They control the van der Waals interactions only for highly reactive or transient species, for which the interactions are primarily determined by covalent bonding. Finally, one additional case that presented difficulties during the parameterization was $(N^C, N^H) = (4,0)$. Although this case could in principle have been parameterized using neopentane (and knowledge of the $(N^C, N^H) = (1,3)$ parameters derived from ethane), we were unable to find parameters that exactly reproduced the pressure and $\Delta_{\text{vap}}H$ for this system. This is presumably because the density and cohesive energy of liquid neopentane depend very little on the van der Waals interactions of the buried central carbon, which interacts very little with neighboring molecules. But for this same reason, the properties of any simulation will be likewise very insensitive to the values of the LJ parameters chosen at this knot point. The parameter value at $(N^C, N^H) = (4,0)$ is extropolated from the simulation determined parameter value at (0,4), (1,3), (2,2), and (3,1).

Once the values of σ_C and ϵ_C are determined at all of the knot points, and the derivatives at these knot points are specified using Eqs. 2.5 and 2.6, it is straightforward to invert Eqs. 2.3 and 2.4 in order to obtain the coefficients c_{kl}^{σ} and c_{kl}^{ϵ} in each domain of the spline. The result of this procedure is shown in Figures 2.2 and 2.3, which show the variation of σ and ϵ with changes in the local coordination number.

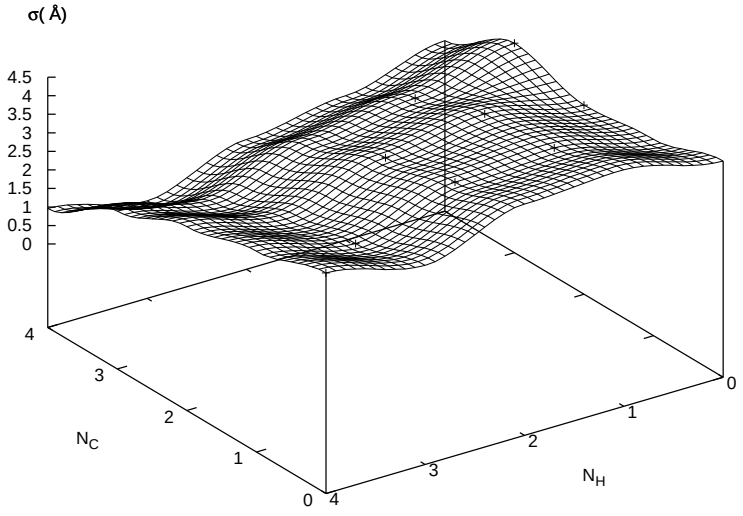

Figure 2.2 Graphical depiction of the $\sigma(N^C, N^H)$ surface. Black crosses stand for the values determined by simulation.

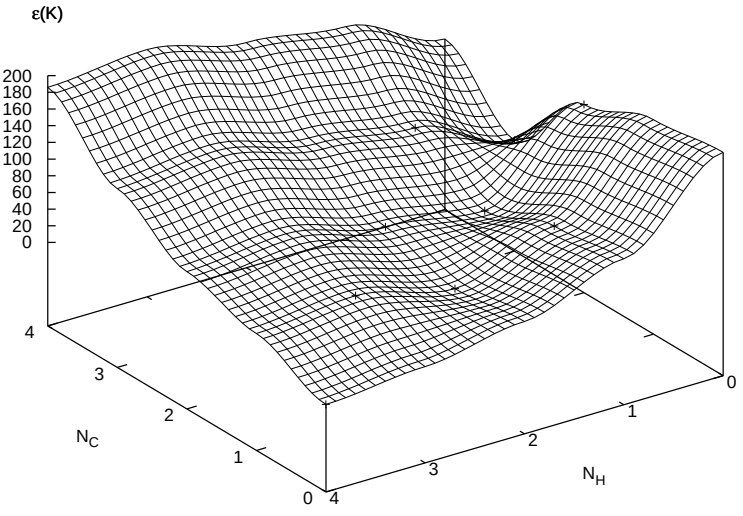

Figure 2.3 Graphical depiction of the $\epsilon(N^C, N^H)$ surface. Black crosses stand for the value determined by simulation.

Results and Discussion

The van der Waals spline knots for carbon atoms that resulted from the fitting procedure are shown in Table 2.2. The variation of the ϵ_C and σ_C parameters with coordination number is illustrated graphically in Figures 2.2 and 2.3.

In order to test the performance of the new LJ parameters, simulations were performed for a variety of compounds not used in the fitting procedure. There are 27 of these test species, consisting of straight-chain, branched, and ring compounds with between three and nine carbon atoms, including saturated and unsaturated species, including conjugated and aromatic species. The full list of 27 test species appears in Tables 2.3 and 2.4. As with the compounds used in the parameterization procedure, the heat of vaporization and pressure are calculated at the experimental density and a specified temperature (typically the boiling point). The results for the new potential, as well as the predecessor AIREBO potential are tabulated in Tables 2.3 and 2.4.

The pressures tabulated in Table 2.3 demonstrate that the PV performance of the current potential is much better than with the previous (non-adaptive) LJ parameterization. For each class of compounds (linear and branched (or ring) alkanes and alkenes, and linear alkynes) the new model shows a substantial improvement over the previous AIREBO parameterization. The MAD from the expected experimental pressure is only $\sim$ 200 bar with the new model, rather than 850 bar with AIREBO. The improvement is particularly good for alkynes, where the mean absolute error in the pressure has been reduced to about 7% of its previous value.

A distribution of errors in the pressure is presented in Figure 2.4. This distribution shows that both potentials tend to overestimate the pressure for hydrocarbons near the normal boiling point, but both the mean and the variance are lower with the new potential. Whereas pressure errors of 0.5 to 2 kbar are common with AIREBO, the largest pressure error observed with the new model on the 27-species test set was 500 bar.

The cohesive energies of liquid molecular hydrocarbons are also improved with the new potential, as can be seen from the heat of vaporization data presented in Table 2.4. The only class of compounds for which the new potential is not improved

compound				P (bar)	
		T(K)	ρ (g cm^{-3})	AIREBO[1]	this work
alkanes	butane	272.7	0.6011[b]	489	88.2
	cyclohexane	298	0.7739[a]	1447	76
	hexane	298	0.6606[a]	706	74.3
	octane	298	0.6986[a]	918	210
	MAD			890	112
	RMSD			980	130
alkenes	Z-butene	276.84	0.6213[b]	538.6	106
	propene	225.46	0.6100[a]	-495	70
	E-butene	274.2	0.6041[b]	372	6.3
	Z-2-pentene	309.8	0.6503[b]	-277	244
	1,2-butadiene	284	0.6760[a]	1426	222
	1,3-butadiene	269	0.6506[a]	704	236
	toluene	298	0.8668[b]	1133	240
	MAD			707	161
	RMSD			823	188
branched alkanes	2,3-dimethylpentane	298	0.6908[a]	692	291
	2,3-dimethylbutane	298	0.6616[a]	503	258.5
	3-methylpentane	298	0.6598[a]	617	168.7
	2-methylhexane	298	0.6787[a]	696	168.2
	2-methylheptane	298	0.698[a]	790	210
	isopentane	301.1	0.6201[a]	418	210
	3-methylhexane	298	0.687[a]	771	204.6
	MAD			641	216
	RMSD			655.7	220
branched alkenes	2-methyl-1,3-butadiene	298	0.679[a]	794	423
	2,3-dimethyl-2-butene	293	0.708[a]	768	321
	trans-1-propenylbenzene	293	0.9023[a]	1596	439
	styrene	298	0.9016[a]	1266	494
	2-methyl-2-pentene	298	0.6863[a]	760	217
	isobutene	298	0.6242[b]	824	517
	MAD			1001	379
	RMSD			1061	394
alkynes	1-butyne	281.23	0.6783[a]	1356	-229
	2-butyne	298	0.691[a]	1994	-28.9
	1-pentyne	298	0.6901[a]	1295	-65
	MAD			1548	107
	RMSD			1596	152
total	MAD			850	207
	RMSD			963	250

[a]Reference[35]
[b]Reference[36]

Table 2.3 Pressures as calculated with the new potential and with the original AIREBO potential[1]. The experimental pressure of each system at the specified state point is 1 bar. The mean absolute deviation (MAD) and root mean square deviation (RMSD) from experiment are provided seperatedly for several categories of compounds.

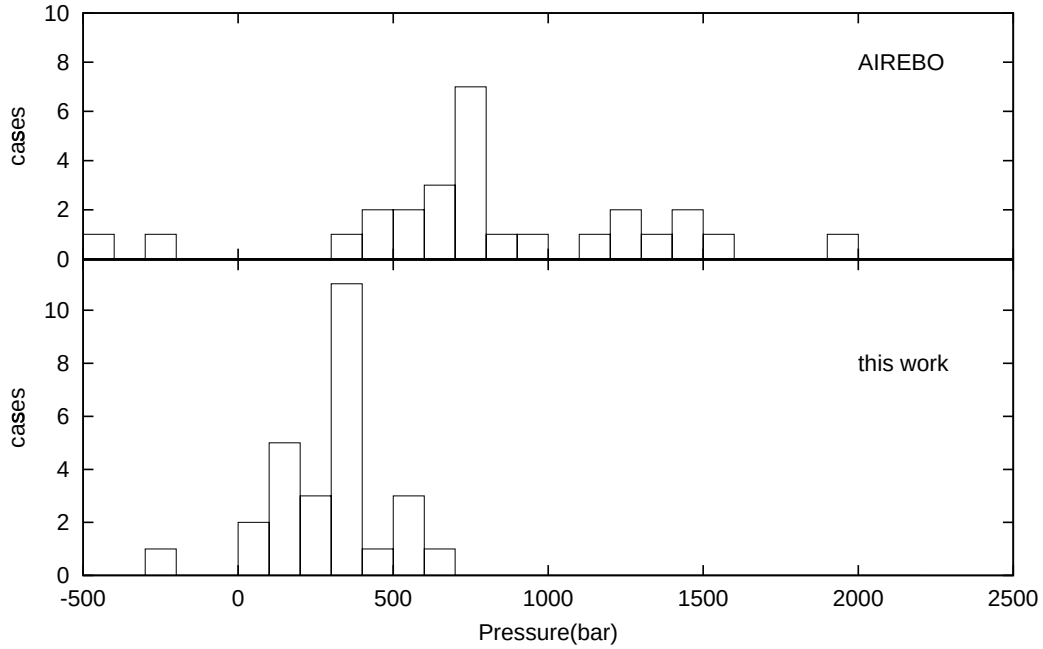

Figure 2.4 Pressure Result: Y axis is the number of test compound that fall in the slot.

is the linear alkanes, where the mean absolute deviation (MAD) in the heat of vaporization increased from 2.42 kJ/mol with the AIREBO potential to 4.08 kJ/mol with the new potential. This is perhaps not surprising, as saturated alkanes are the class of compounds for which the AIREBO potential was explicitly parameterized. For all other classes of compounds examined, the new potential provides an improved description of the cohesive energy in the liquid. The improvement is dramatic for linear alkenes, with the MAD decreasing from 3.13 kJ/mol to 0.49 kJ/mol. For the set of test molecules taken as a whole, the MAD has improved by from 3.86 kJ/mol to 1.96 kJ/mol, and now indicates a mean absolute error of less than 7% in the heat of vaporization. Because no data from this test set were included in the parameterization, and efforts have been made to ensure that the test set represents a variety of different types of small hydrocarbon molecules, these errors can be expected to be typical for additional species not analyzed here. Figure 2.5 shows the distribution of error values in the heat of vaporization with the AIREBO and new potential. This figure shows clearly that the average magnitude of the error is reduced with the new potential.

The carbon–carbon pair correlation function, $g_{CC}(r)$, is very sensitive to the van

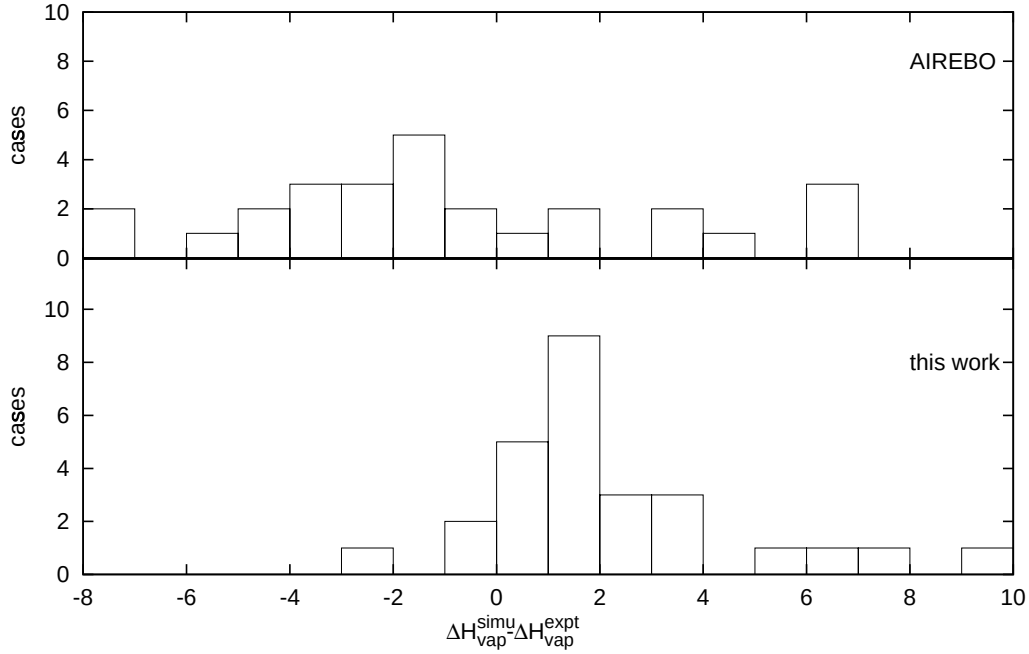

Figure 2.5 Distribution of error in the simulated heat of vaporization for 27 liquids in testset.

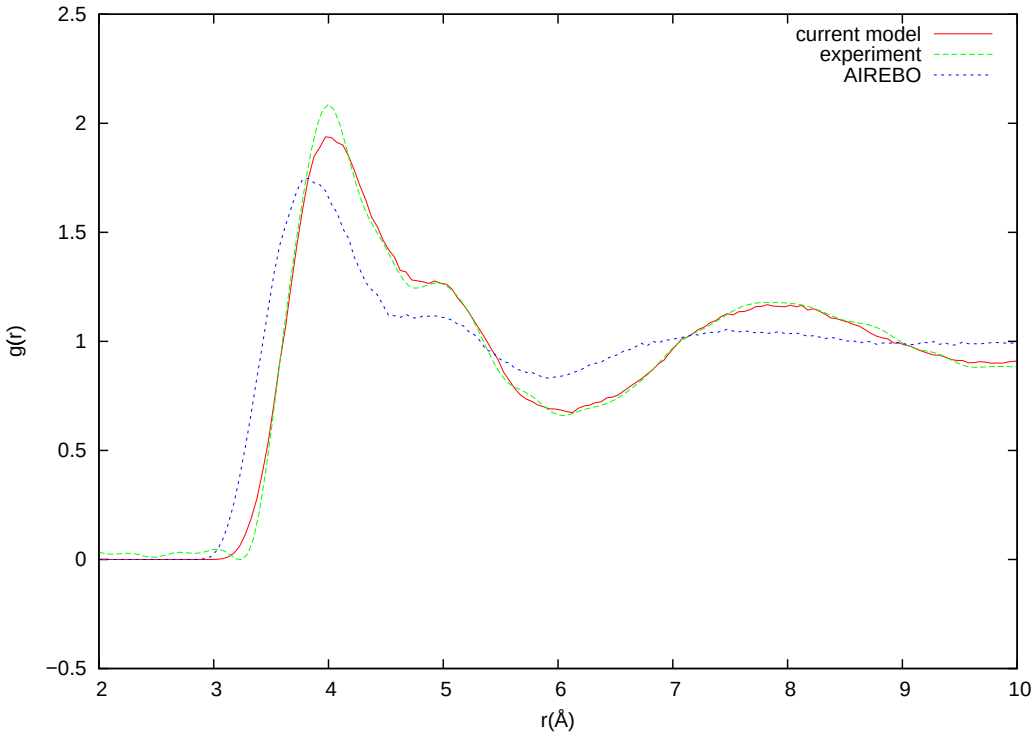

Figure 2.6 Carbon-carbon pair correlation function g_{CC} for liquid ethylene at 106 K. Experimental result from Ref.[2]

compounds	Expt	AIREBO[1]			this work		
	ΔH_{vap}	ΔH_{vap}	$\Delta(\Delta H_{\mathrm{vap}})$	%	ΔH_{vap}	$\Delta(\Delta H_{\mathrm{vap}})$	%
	(kJ/mol)	(kJ/mol)			(kJ/mol)		%
alkanes							
butane	22.44[a]	22.95	0.51	2.27	23.34	0.90	4.00
cyclohexane	33.01[a]	33.81	0.80	2.42	34.78	1.77	5.36
hexane	31.56[a]	34.39	2.83	8.96	35.98	4.42	14.0
octane	41.49[a]	47.06	5.57	13.42	50.72	9.23	22.3
MAD			2.42	6.77		4.08	11.40
RMSD			3.37	8.67		5.54	14.21
alkenes							
Z-butene	23.34[a]	20,83	-2,51	-10,7	22.18	-1.16	-4.94
propene	18.42[a]	21.57	3.15	17.1	18.64	0.22	1.20
E-butene	22.72[c]	22.04	-0.68	-2.98	22.10	-0.62	-2.73
Z-2-pentene	26.1[c]	32.09	5.99	22.9	26.81	0.71	2.73
1,2-butadiene	24.02[a]	21.48	-2.54	-10.6	24.38	0.36	1.50
1,3-butadiene	22.47[a]	19.44	-3.03	-13.5	22.18	-0.29	-1.27
toluene	38.01[a]	34.01	-4.00	-10.5	38.09	0.08	0.21
MAD			3.13	12.63		0.49	2.08
RMSD			3.52	14.08		0.61	2.59
branched alkanes							
2,3-dimethylpentane	34.26[a]	25.48	-8.78	-25.6	33.96	-0.30	-0.89
2,3-dimethylbutane	29.12[a]	23.55	-5.57	-19.1	28.52	-0.60	-2.04
3-methylpentane	30.28[b]	27.07	-3.21	-10.6	30.71	0.43	1.42
2-methylhexane	34.87[a]	36.94	2.07	5.93	39.91	5.04	14.4
2-methylheptane	39.67[a]	37.97	-1.70	-4.27	41.16	1.49	3.76
isopentane	24.79[c]	30.43	5.64	22.75	31.54	6.75	27.2
3-methylhexane	35.1[b]	31.56	-3.55	-10.1	35.97	0.87	2.47
MAD			4.35	14.06		2.21	7.46
RMSD			5.01	16.38		3.40	12.39
branched alkenes							
2-methyl-1,3-butadiene	26,8[b]	24.11	-2,69	-10.04	27.81	1.41	5.34
2,3-dimethyl-2-butene	32.51[a]	24.37	-8.14	-25.1	30.75	-1.76	-5.41
trans-1-propenylbenzene	46.4[b]	45.23	-1.17	-2.51	49.38	2.98	6.42
styrene	43.9[b]	33.62	-5.08	-13.1	43.70	-0.2	-0.45
2-methyl-2-pentene	31.6[b]	28.86	-2.74	-8.68	31.88	0.28	0.88
isobutene	22.13[a]	19.81	-2.32	-10.60	18.52	-3.61	-16.31
MAD			4.49	13.1		1.71	3.70
RMSD			5.85	15.9		2.20	4.64
alkynes							
1-butyne	24.52[a]	20.38	-4.14	-16.9	27.22	2.70	11.0
2-butyne	26,7[b]	22,69	-4,26	-15,8	27.28	0.33	1.24
1-pentyne	28.4[b]	22.18	-6.22	-21.9	30.80	2.40	8.46
MAD			4.79	17.9		1.89	7.22
RMSD			4.94	18.3		2.22	8.54
total							
MAD			3.86	12.8		1.96	6.45
RMSD			4.62	14.8		2.98	9.55

[a]Reference[35]
[b]Reference[36]
[c]Reference[37]

Table 2.4 Heat of vaporization as calculated with the new potential, with the original AIREBO potential[1], and as reported experimentally. The mean absolute deviation (MAD) and root mean square deviation (RMSD) from experiment are provided.

der Waals interactions in the liquid. The positions of the peaks are highly sensitive to the density of the fluid and the atomic radii, while the peak heights are sensitive to the strength of the nonbonded interactions, relative to kT. The $g_{CC}(r)$ data were not utilized in the parameterization of the new potential (unlike the parameterization of the AIREBO potential). Thus a comparison of pair correlation functions with experiment provides additional evidence of the success of the new potential, relative to the previous AIREBO potential. Figures 2.6 through 2.9 show the pair correlation functions for ethylene, benzene, ethane, and methane. It shows from these figures that the structure of the liquid is usually better described with the new potential. Even for systems that were explicitly used in the parameterization of the original AIREBO potential, such as methane, the pair correlation function is substantially improved with the new potential. Not all systems have better results in pair correlation functions. Figure 2.8 shows that the result for ethane is worse than the result from AIREBO potential. This is not surprising in that AIREBO parameter specifically fit to pair correlation function of ethane.

Conclusions

A new potential has been developed and implemented which enables the van der Waals interactions in a reactive bond-order potential to vary with the chemical environment. This is done by having the parameters characterizing the van der Waals interaction (σ and ϵ in the Lennard-Jones equation) for a particular atom vary smoothly and continuously with the coordination number and chemical identity of the neighbors of that atom, via a bicubic spline. This model has been parameterized using the energetics and PV behavior of a set of 8 hydrocarbon molecules. When used to simulate a set of 27 molecules that were not included in the parameterization procedure, this potential provides substantially improved results over the AIREBO potential, which does not allow for adaptive changes in the van der Waals interactions. For stable molecular species, the errors in the pressure near the boiling point were reduced from 850 under AIREBO to 207 bar with the new model. The errors in predicted heats of vaporization are reduced by approximately 30%, to below 3

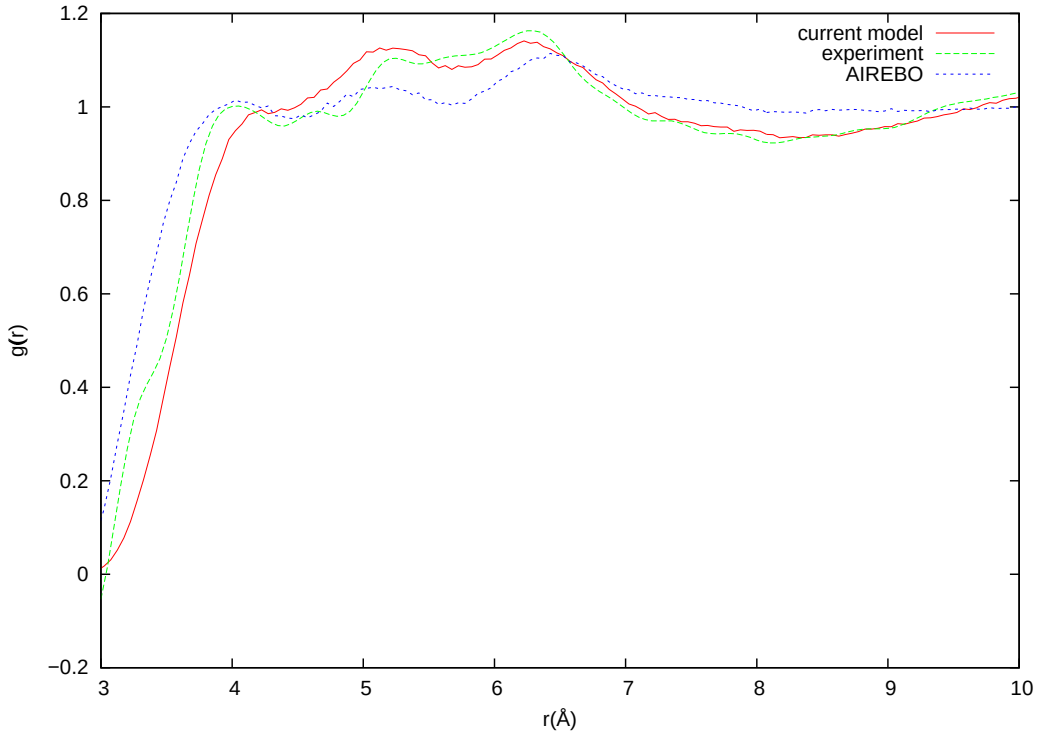

Figure 2.7 Carbon-carbon pair correlation function g_{CC} for liquid benzene at 298 K. Experimental result from Ref.[3]

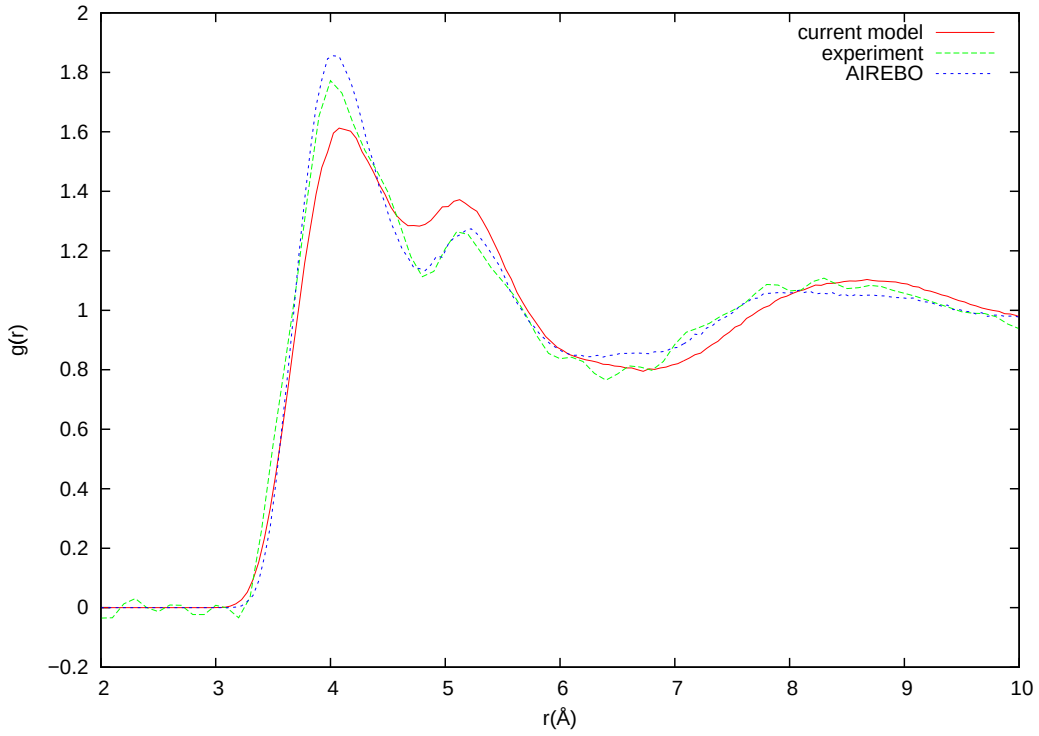

Figure 2.8 Carbon-carbon pair correlation function g_{CC} for liquid ethane at 105 K. Experimental result from Ref.[4]

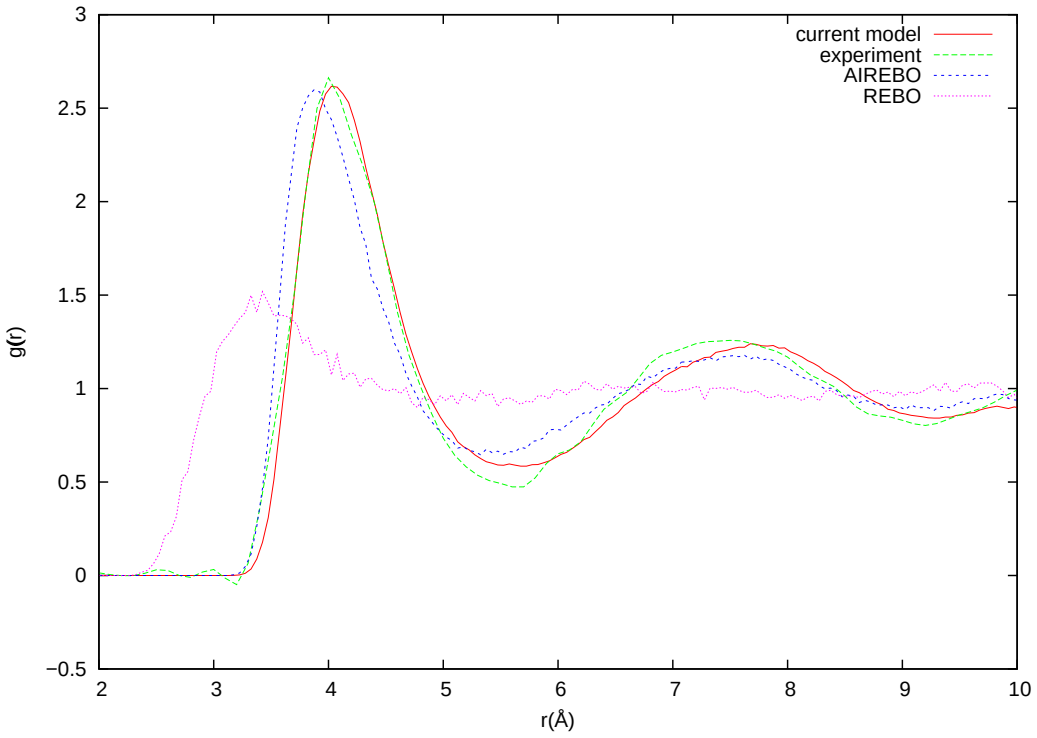

Figure 2.9 Carbon-carbon pair correlation function g_{CC} for liquid methane at 92 K. Experimental result from Ref.[2]

kJ/mol.

This potential will be most useful in simulations of chemically reactive systems. The adaptive nature of the nonbonded interactions ensures that they can adjust to changing chemical environments, and the continuous nature of the potential guarantees that the resulting forces can be evaluated and used in a dynamics simulation.

CHAPTER 3
SIMULATION OF CARBON NANOTUBE JUNCTION FORMATION WITH AIREBO POTENTIAL

Introduction

Given the fact that SWNTs can be metallic or semiconducting, junctions between different types of SWNTs can be very useful in nanoscale electronics. Simulations of the formation of nanotube junctions have been performed in recent years. These simulations include modeling electron beam welding and ion irradiation [38, 39, 40, 41, 42].

There were several reports of experiments on the formation of junctions between nanotubes. One of these was published by Terrones and coworkers.[38] In their work, they used electron beams to weld SWNTs together. The experiment was carried out in a high voltage TEM at 800 °C. Under controlled electron beam conditions, the merging of nanotubes was observed at the contact area on timescales of a few minutes. Since the junction didn't form without irradiation, they concluded that electron beam effects were responsible for the formation of junctions. They reasoned that irradiation-induced vacancies in the tubes help to form the junction. Dangling chemical bonds around the vacancies were assumed to serve as the bridge between nanotubes. Furthermore, they performed tight binding molecular dynamics simulations of the welding process. The temperature of these simulations was 1000 °C in order to accelerate the junction formation. The total simulation time was 220 ps. By the end of the simulation, a surface reconstruction had taken place and the two nanotubes had formed an X junction. They concluded that the mechanism of junction formation of nanotubes was the creation of vacancies and interstitials induced by the high energy electron beam. Thus it is possible to construct nanotube networks by welding nanotubes together with electron beams at high temperature.

Banhart also performed studies of soldering nanotubes by electron beam.[39] This study investigated soldering multiwalled carbon nanotubes by irradiating the junction with a scanning electron microscope. X and T junctions were formed.

Ni and coworkers[40] studied the ion beam modification of carbon nanotube bundles both experimentally and computationally. In the computational study, they used classical MD simulation with the REBO force field to perform the bombardment of CH_3^+ on bundled single wall nanotubes (SWNTs) and multi-wall nanotubes (MWNTs). At an incident energy of 10 eV, most of the CH_3^+ ions were absorbed while the rest were scattered from nanotubes. At 45 eV, most of the ions lost one to two hydrogen atoms in collision. About half of the large fragments adhered to the outer nanotube surface. Some of these fragments bonded to a surface carbon atom and stabilized. At 80 eV, most of the fragments penetrated the surface and modified the internal structure. The rest were adsorbed onto the outer surface. The issue of forming internanotube junctions was also investigated computationally by bombarding crossed nanotubes with low energy carbon ions. These simulations predicted the formation of bonds between nanotubes. This work confirms experimentally and computationally that ion beams can be used to functionalize, cross-link, connect and create defects in nanotubes.

Sinnott[41] simulated carbon nanotube welding using electron beam irradiation. The REBO potential was used in this study. The simulation system consisted of two nanotubes crossing each other at a 90 degree angle. Both ends of the two tubes were fixed. This study investigated the electron beam welding of the following four pairs of nanotubes: (5,5)-(5,5), (10,0)-(10,0), (8,3)-(8,3) and (5,5)-(10,0). The simulation showed that the chirality of the nanotubes has an influence on the formation of junctions. They found that (5,5)-(5,5) pairs join more smoothly than other pairs, followed by (5,5)-(10,0),(8,3)-(8,3) and (10,0)-(10,0). There was no significant difference in the bonding properties in the impact zone.

Another simulation of welding carbon nanotubes by Krasheninnikov et al. used Ar ion irradiation[42]. In their research, they simulated the Ar ion irradiation on both suspended carbon nanotubes and supported nanotubes. They also used the REBO

potential[9] to do the simulation. The temperature was 1000 K, similar to actual electron irradiation experiments. The SWNT pairs they used in their simulation were: (10,10)-(10,10), (12,0)-(10,10), (12,0)-(10,3) and (16,0)-(16,0). The optimum energy of ion was determined to be 0.4-0.6 keV. The optimum dose is in the range of (0.5-0.7)$\times 10^{15}$ cm^{-2} for nanotubes with diameters < 1 nm and 1×10^{15} cm^{-2} for larger nanotubes. High temperatures were indispensable in junction formation. They concluded that ion irradiation may be used to produce nanotube junctions. They also demonstrate that without ion irradiation, even high-pressure compression of crossed nanotubes at high temperature won't create junctions.

Simulation System

There have been several simulations of nanotube welding. But still not every aspect of the process has been investigated.

For example, the molecular dynamics simulations performed by researchers have all used the REBO potential. It is known that the REBO potential has some restrictions. One of these is that intermolecular interactions are not included. Although in some reaction systems these may not be very important, it is important in the case of nanotubes because of the large number of atoms and the nonbonded interactions between the graphitic walls of the crossed nanotubes. The new AIREBO potential with adaptive treatment of intermolecular interaction fully incorporates the van der Waals interaction and its variation during chemical reactions, making it a better choice in these simulations.

Another research area not covered by previous investigation is the electronic property changes during the junction formation. In what stage of junction formation the rectifying behavior becomes apparent is still unknown. By exploring the electronic properties of our simulation results, we can reveal some aspect of the conduction behavior of nanotube junctions.

Junction Formation Between Perfect Nanotubes

The simulation was performed to weld nanotubes placed at 90 degree angles to each other (Figures 3.1 and 3.2). Immediately beneath the bottom nanotube was an imaginary reflective surface. All atoms collided with this surface were reflected elastically

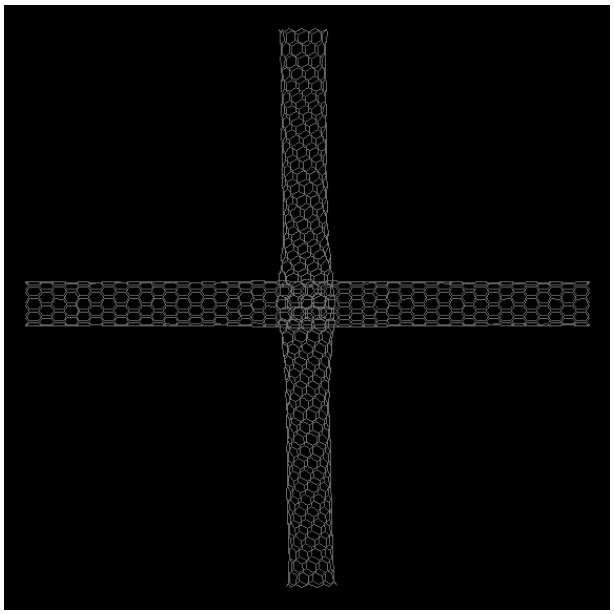

Figure 3.1 Crossed carbon nanotubes. top view: (10,0) on (10,0)

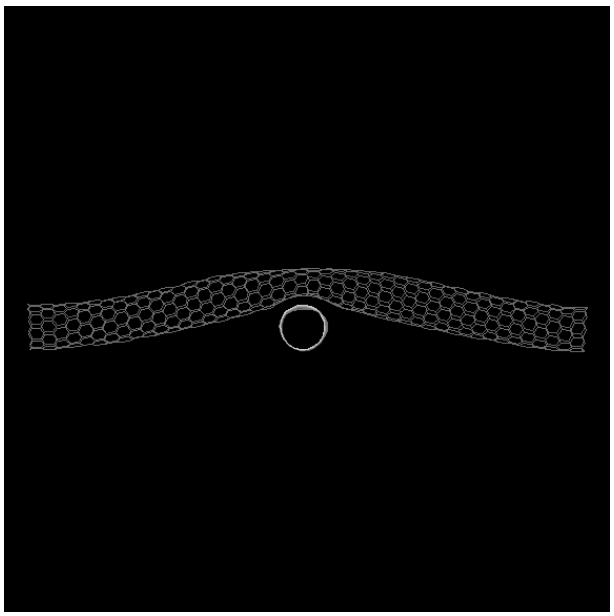

Figure 3.2 Crossed carbon nanotubes. side view: (10,0) on (10,0)

by reversing the z component of their velocity. This imaginary reflective surface was used to simulate supported nanotube welding. The advantage was that it was much computationally efficient than atomistic simulation of the substrate. Nanotubes were fully relaxed by running a simulation for 100 ps at 1000 K. Both ends of these two

nanotubes were fixed. A contact area was defined for these two nanotubes. The size of contact area was the same as the overlapping area of two nanotubes. Depending on the size of nanotubes, the side of rectangular overlap region ranges from 5 Å to 15 Å. The area of the contact region is from 20 $Å^2$ to 165 $Å^2$. From a plane 10 Å above this intersection, Ar ions were generated randomly with a velocity directed toward the nanotube overlapping area. Through this arrangement, Ar ions were guaranteed to hit some carbon atom. The damages from both nanotubes provided reconstruction material for the junction formation. At the beginning of the simulation, the system temperature was set to 1000 K. During the welding process, the temperature would increase with each impact. A Langevin thermostat[33] was used to keep the system at 1000 K after some time for the evolution of defects.

A series of different Ar ion energies was used in the simulations. The speeds of Ar ions used were 0.3, 0.4, 0.5, 0.6, and 0.7 Å/fs. The corresponding impact energies were 186 eV, 330 eV, 516 eV, 742 eV and 1010 eV. For each simulation, the ion energy is constant. A total of 20 Ar ions were generated in each simulation. Since the intersection areas were not the same in each combination, the flux and fluence were not the same for each case. The fluence is the number of impacts per unit area. And the flux is the number of impacts per unit area per unit time. Table 3.3 lists the flux and fluence for all cases. The total ion irradiation dose for each case is 20 impacts on an impact zone of 20-200 $Å^2$, or in the vicinity of (1-10)$\times 10^{15}$ ion/ cm^{-2}. By comparing number of defects created from different nanotube combinations with different ion energies, the effect of the ion impact energy on nanotube junction formation is investigated.

The simulations were performed in three steps. The first step is the ion irradiation period. In this step, an Ar ion was generated randomly in the plane parallel with the substrate. It bombarded the nanotube intersection and transfered its energy to nanotube carbons if it collided with carbon atoms in the nanotube. The time steps were very small in order to conserve energy. For low energy impact (186 eV, 330 eV), it was found that a 0.01 fs time step was good enough. For larger energy impact (516 eV, 742 eV, 1010 eV), the time steps could be as low as 0.005 fs or 0.004 fs, depending

	SWNT	diameter(Å)	S/M
large	(11,9)	13.58	S
	(10,10)	13.56	M
small	(7,5)	8.17	S
	(6,6)	8.14	M
	(10,0)	7.83	S
	(9,0)	7.05	M
	(5,5)	6.78	M

Table 3.1 Nanotubes used in the simulations. S: Semiconducting; M: Metallic

on the nanotubes. At the end of step 1, the most drastic chemical rearrangements were typically finished. This step lasted 200 fs. The second step is the defect evolution process. During this step, the impact energy was dispersed across more carbon atoms in the nanotube. Additional bond breaking and bond forming reactions are expected in this stage as more atoms are affected by collisions. In this step, many defects could be formed. It lasted 5000 fs to let the system fully evolve and the impact energy fully thermalize. The time step in this period is 0.1 fs, much longer than during the first step. The third step was the cooling of the system. A Langevin thermostat was used in this simulation. The purpose of this process is to keep the system from evaporating after repeated impacts. This process lasted 3000 fs. Because systems are not required to conserve energy when being thermostatted, the time step was 0.2 fs in the third stage. At this point, another impacting ion was generated and the three steps were repeated. During these simulations, the structure of the impact zone was explored to examine damage to the nanotubes. The number and type of defects and the conductivity of nanotube were explored after the third step.

The nanotubes used in the simulations were divided into three groups: metallic-semiconductor(MS), metallic-metallic(MM) and semiconductor-semiconductor(SS). Metallic SWNTs (9,0), (5,5), (10,10) and (6,6) were used. Semiconducting SWNTs (11,9), (7,5) and (10,0) were also used. Table 3.1 shows the diameter of the nanotubes used in the simulations.

Simulations were conducted on the 7 SWNT pairs with identical structures, i.e. (10,10)-(10,10), (11,9)-(11,9), etc. In addition, combinations of different SWNTs were

TYPE	nanotubes
SS	(7,5)-(10,0)
MM	(9,0)-(6,6)
SM	(10,10)-(11,9)
	(10,0)-(6,6)

Table 3.2 Heterostructure nanotube junctions formed in simulation

nanotube combination	area of impact zone	flux	fluence
	$Å^2$	$(10^{26})s^{-1}cm^{-2}$	$(10^{15})cm^{-2}$
(11,9)/(11,9)	144	1.69	1.39
(10,10)/(11,9)	120	2.03	1.67
(10,10)/(10,10)	165	1.48	1.21
(7,5)/(7,5)	45.5	5.36	4.39
(7,5)/(10,0)	45.5	5.36	4.39
(10,0)/(10,0)	20.9	11.7	9.56
(9,0)/(9,0)	28.4	8.6	7.05
(10,0)/9,0)	45.5	5.36	4.39
(5,5)/(5,5)	39.0	6.25	5.12
(6,6)/(9,0)	45.5	5.36	4.39
(6,6)/(10,0)	45.5	5.36	4.39
(6,6)/6,6)	51.4	4.74	3.89

Table 3.3 Flux and fluence in nanotube junction formation simulations

also simulated. For the MS type of junction formation, (10,10)-(11,9), (10,0)-(9,0), and (10,0)-(6,6) were used. For the MM type, (9,0)-(6,6) were used. For SS type junctions, (7,5)-(10,0) was used in simulation. The simulation of junction formation between identical SWNTs also revealed either MM or SS type nanotube combinations. Table 3.2 identifies the heterostructured pairs of SWNTs that were used. Thus a total of 12 different SWNT junctions were simulated.

The length of the nanotubes was 100 Å. If tubes were too long, it would require too much time to do the simulation. If they were too short, the elastic strain of the nanotubes could not be fully relaxed (see Figure 3.2).

Conductivity of Joint Nanotube

One possible application of nanotube junction is nanoscale electronic devices, such as transistor devices. So it is important to investigate electronic properties of nanotube junctions. An examination of the relationship between conductivity and nanotube

welding process is especially meaningful in determining the quality of nanotube junctions.

The current $I_{ij}(\tilde{v})$ flowing from terminal i to terminal j of the nanotube junctions with applied voltages $\tilde{v} = \{V_1, \cdots, V_n\}$ was calculated by using the Landauer formula [43]:

$$I_{ij}(\tilde{v}) = \frac{2e^2}{h} \int T_{ij}(\tilde{v}, E) \times [f_0(E - \mu_i - eV_i) - f_0(E - \mu_j - eV_j)]dE \qquad (3.1)$$

In this equation, f_0 is the Fermi-Dirac distribution, μ_i and μ_j are the chemical potential of nanotube terminal i and j. V_i and V_j are applied voltages on terminals i and j. Thus $f_0(E-\mu-eV)$ reflects the population of electrons at an excitation energy $E - \mu - eV$ for a terminal with chemical potential μ and applied voltage V. The difference in Fermi-Dirac distribution will be large for energy E at which the difference in electrochemical potential between terminal i and j results in a substantially non-equilibrium distribution of electron.

$T_{ij}(\tilde{v}, E)$ is the two-terminal transmission at energy E with applied voltages $\tilde{v}$[44]. The transmission function can be expressed in terms of the Green's function of the conductors and the coupling between conductors and leads. The Green's function is obtained from the Hamiltonian matrix of the conductor region and self-energies. The coupling between conductors and leads is expressed as a function of the advanced and retarded self-energies terms of the leads. An iterative transfer matrix procedure is used to calculate self-energies. A Slater-Koster tight-binding Hamiltonian is used in calculating the density of states. These calculations were performed after the cooling period of each impact for selected tubes. They were done in collaboration with Vincent Meunier at Oak Ridge National Lab(ORNL). This technique has been used successfully in the past to calculate the conductance and electronic properties of systems such as doped carbon nanotubes[45], and haeckelite structures[46].

For different applied voltages, the corresponding currents I_{ij} can be calculated. Using a linear fitting procedure on the $I(V)$ relationship, we can derive a scalar conductance between each pair of terminals.

Results and Discussions

Many defects can be created by high energy ion bombardment of nanotubes. They can be divided into two groups concerning nanotube welding: constructive defects and destructive defects. Constructive defects help bonding between nanotubes, thus making the nanotube junction robust. Destructive defects tend to destroy nanotube structure, making it hard to retain its shape. The degree of welding can be evaluated by the number of constructive defects created during the welding process. Conductivity of nanotube junctions can also be related to the quality of the junction formation.

Damages to Nanotube Structure

Carbon atoms in a perfect nanotube are in a sp^2 hybridization state as in a graphene sheet. When some bonds are broken, new carbon hybridization states are created. There are several types of damages caused by Ar ion bombardment. After direct impact by a high energy Ar ion, bonding between carbon atoms is weakened. If one carbon bond dissociates, the participating carbons will become sp hybridized, bonding with two carbons instead of three as in sp^2 carbon. If two bonds on the same carbon are broken, this carbon can be described by an s hybridization state, connecting with only one other carbon. This requires much more energy and the probability for a carbon losing two bonds is low. Thus number of s carbons is significantly less than sp carbons. If the collision between the incoming Ar ion and a nanotube carbon is head-on and the Ar energy is high enough, it is possible to knock the carbon entirely out of the nanotube structure. A single carbon atom without any bonds will be the collision result. These can all be viewed as destructive defects. Alternatively, sp^3 carbon can be formed when reactive carbon species bond with each other. In some rare cases, when sp^3 carbon is approached by some carbon radical, it is possible for them to briefly form sp^3d carbon. This structure is not stable and will typically decay after a short time. Figure 3.3 shows a typical distribution of defects evolving with the welding process.

Cross-link defects are especially important as constructive defects in nanotube welding. A crosslink denotes bonding between carbon atoms in the top and bot-

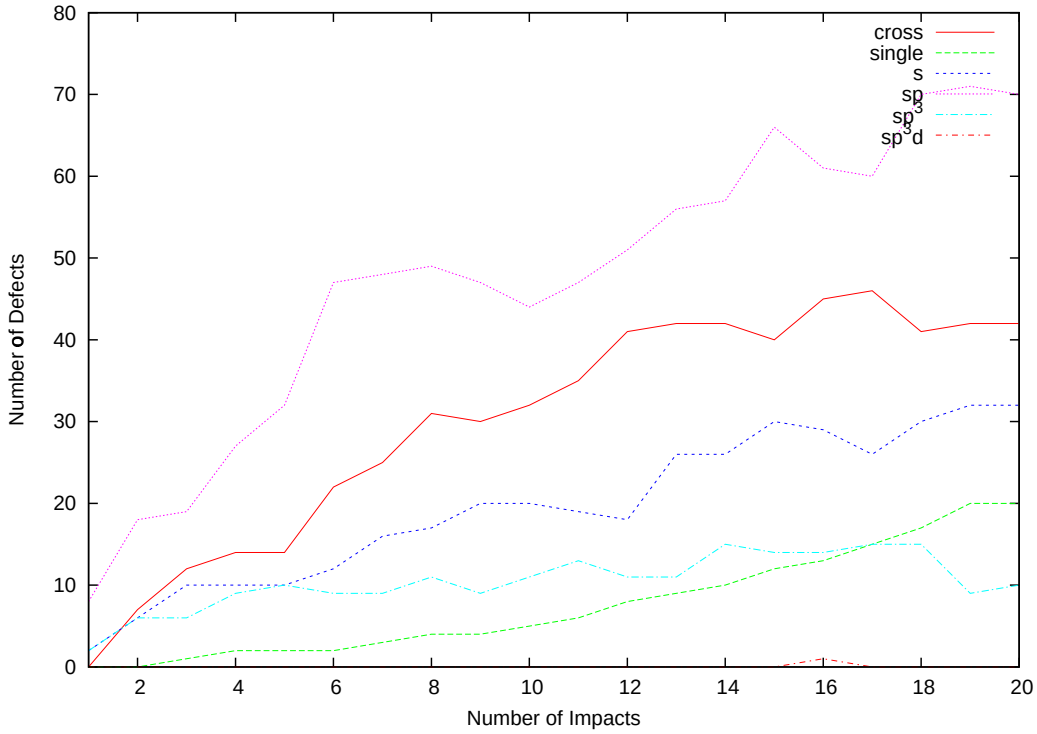

Figure 3.3 Evolution of the number of various types of defects during the carbon nanotube junction formation process for a (6,6)/(10,0) junction.

tom nanotubes. These defects are important because only cross-links can bond two nanotubes together. Initial impact by energetic particles will cause damages on one nanotube wall. Some particles may be knocked out of the nanotube structure. Loss of particles is the destructive aspect of nanotube welding. Other carbon atoms may become active species by breaking bonds. When they are close to other reactive species from another nanotube, new bonds may be formed and cross-links created.

Figure 3.4 illustrates various types of defects created by ion impact. The yellow atom (s) bonds with only one carbon. The middle red atom (sp) bonds with only two other red carbon atoms. Green and blue atoms form cross-links between the upper and bottom nanotube.

Figure 3.5 shows the change in the number of cross-links during twenty impact simulations at five different energy impact energies for the (6,6)/(10,0) pair. The number of cross-links created at the lowest energy of 186 eV steadily increases during the twenty impacts. With increase of energy, more cross-links are formed even after

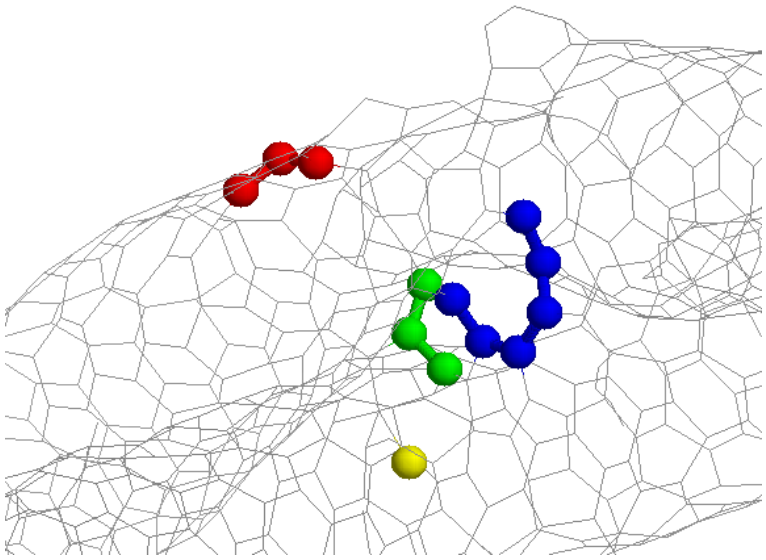

Figure 3.4 Illustration of defects during carbon nanotube junction formation for a (6,6)/(10,0) pair after 15 impacts at 186 eV.

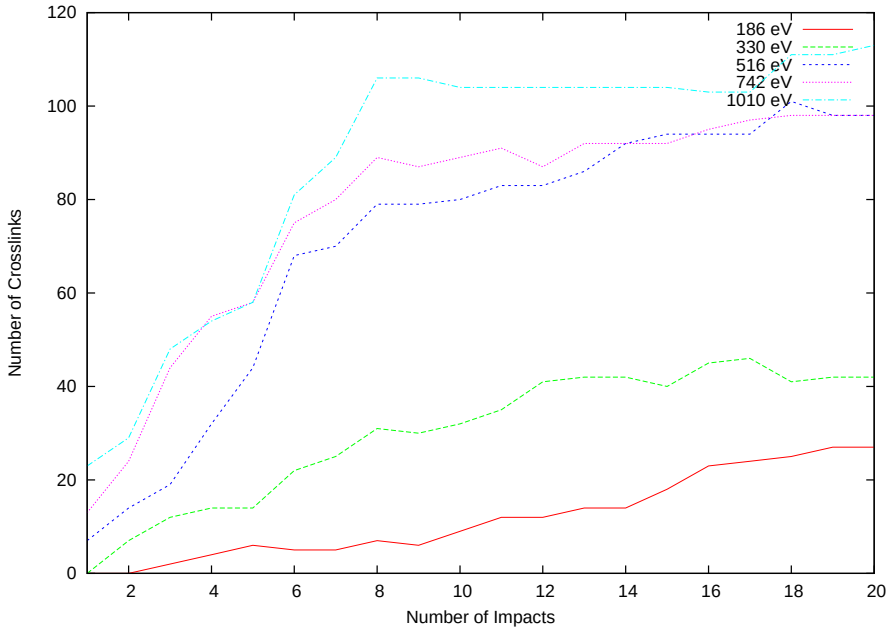

Figure 3.5 Change in number of cross-links for (6,6)/(10,0) carbon nanotube junction formation at 5 different impact energies.

the first energetic impact. Results from lower energies of 186 and 330 eV differ from those at higher energies of 516 eV, 742 eV and 1010 eV. The low energy impacts show a slow and steady increase in the number of cross-links. After 12 impacts, the 330 eV irradiation remains nearly constant at 40 cross-links. The three high impact energies 516 eV, 742 eV and 1010 eV have more cross-links than 186 eV and 330 eV. For each of these systems, the number of cross-links increased rapidly before the 8th impact. Then there is a slow increase for 516 eV and 742 eV, with a plateau of close to 100 cross-links in each case. A visual examination of the nanotube (Figure 3.6) shows that after 8 impacts, most of the intersection had been ablated by the 1010 eV impacts, leaving much less carbon atoms to form cross-links. Similar behavior can be seen for other small nanotubes.

For larger nanotubes like (10,10) and (11,9), the results are different. Figures 3.7, 3.8 and 3.9 all show a steady increase of cross-links with increasing fluence at all 5 energy levels for each of the 3 junctions between these two larger tubes. No plateau is observed at fluences up to $1.2 - 1.7 \times \text{cm}^{-2}$. Larger nanotubes have more carbon atoms in the impact zone. The energy of incoming ion is likely to be absorbed by more atoms in nanotube structure than small nanotube. The impact on each carbon atom is decreased. Thus they are less likely to be knocked out of the structure. Figure 3.10 shows that the structure of the (10,10)/(10,10) junction remains together in the impact zone after 20 impacts at energy 742 eV.

Defects in Different Nanotubes at The Same Impact Energies

The formation of various defects under the same impact energies is also investigated. Figures 3.11 through 3.15 compare the cross-link formation for all nanotubes at 5 different impact energies. One observation from these figures is that at lower energies (186 eV, 330 eV, and 516 eV, see Figures 3.11, 3.12, and 3.13), number of cross-links in larger nanotubes (i.e. (10,10) and (11,9)) is not among the largest. But at higher energies (742 eV and 1010 eV, see Figures 3.14 and 3.15), the three combinations of larger nanotubes have the most cross-links among 12 nanotube combinations. This implies that lower impact energies are not strong enough to create

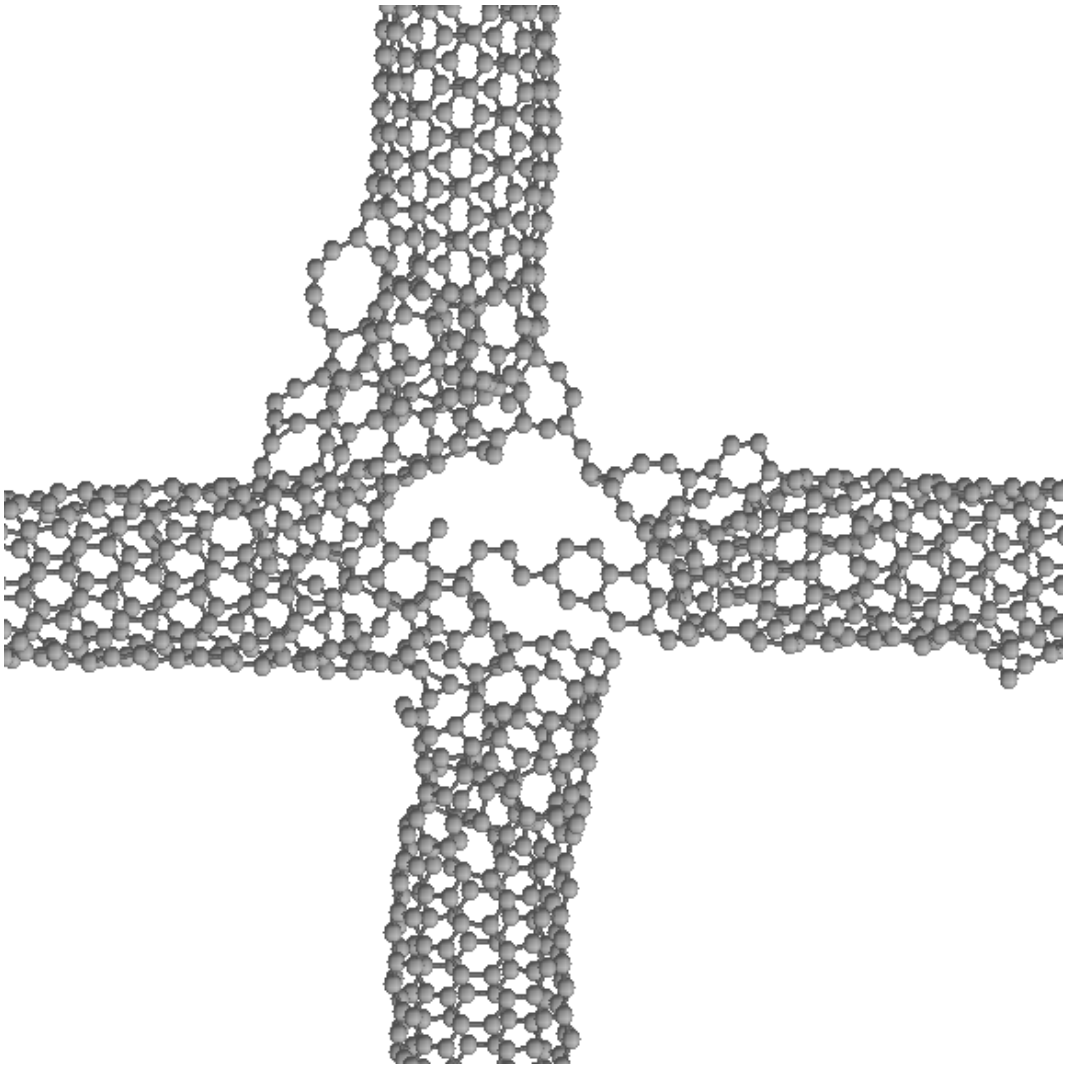

Figure 3.6 Carbon nanotube junction formation for the (6,6)/(10,0) pair after 8 impacts at energy 1010 eV.

constructive defects for large nanotubes (> 13Å). Another observation from these figures is that the plateau is between 60-100 cross-links for the smaller nanotubes. Most small nanotubes has plateau between 60-80 (see Figures 3.12, 3.13, and 3.14). This plateau is reached quite early for high impact energies and is not reached within 20 impacts for the lowest impact energy considered. The plateau starts as early as 4th impact. After plateauing, the number of cross-links fluctuates in a small range.

One special case in Figures 3.14 and 3.15 is the (10,0)/(10,0) pair. The number of cross-links for this combination is significantly lower than other small nanotubes (37 compared to 60 in Figure 3.14, 40 compared to 50 in Figure 3.15). The main reason is

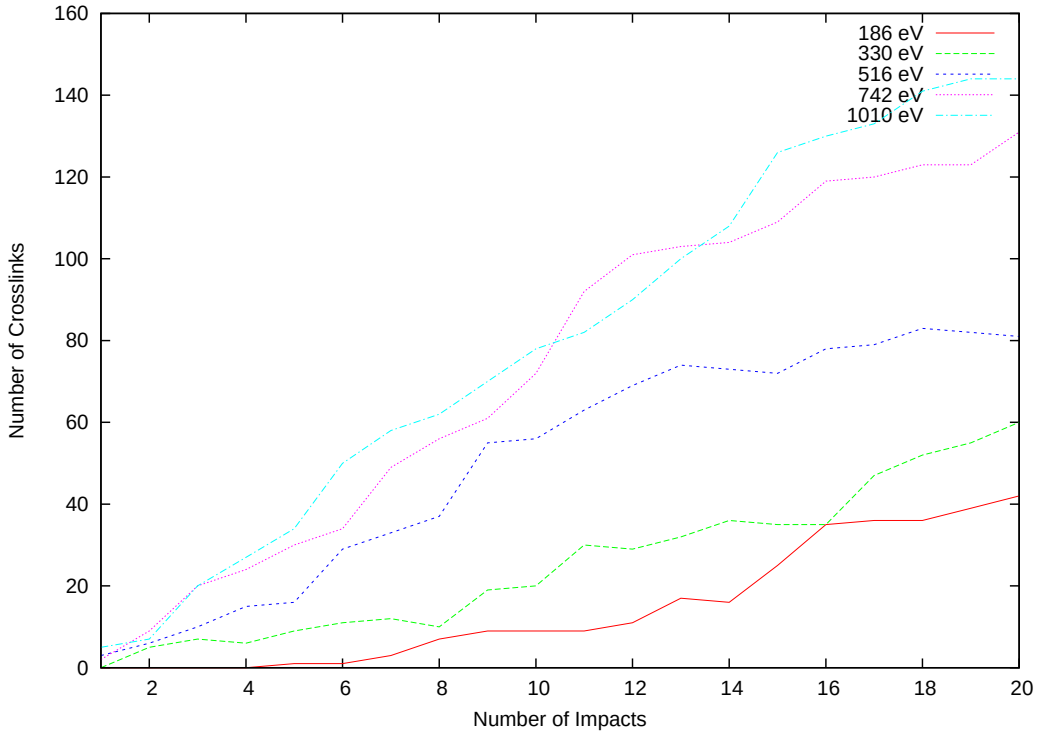

Figure 3.7 Evolution of cross-links in carbon nanotube junction formation for the (10,10)/(10,10) pair.

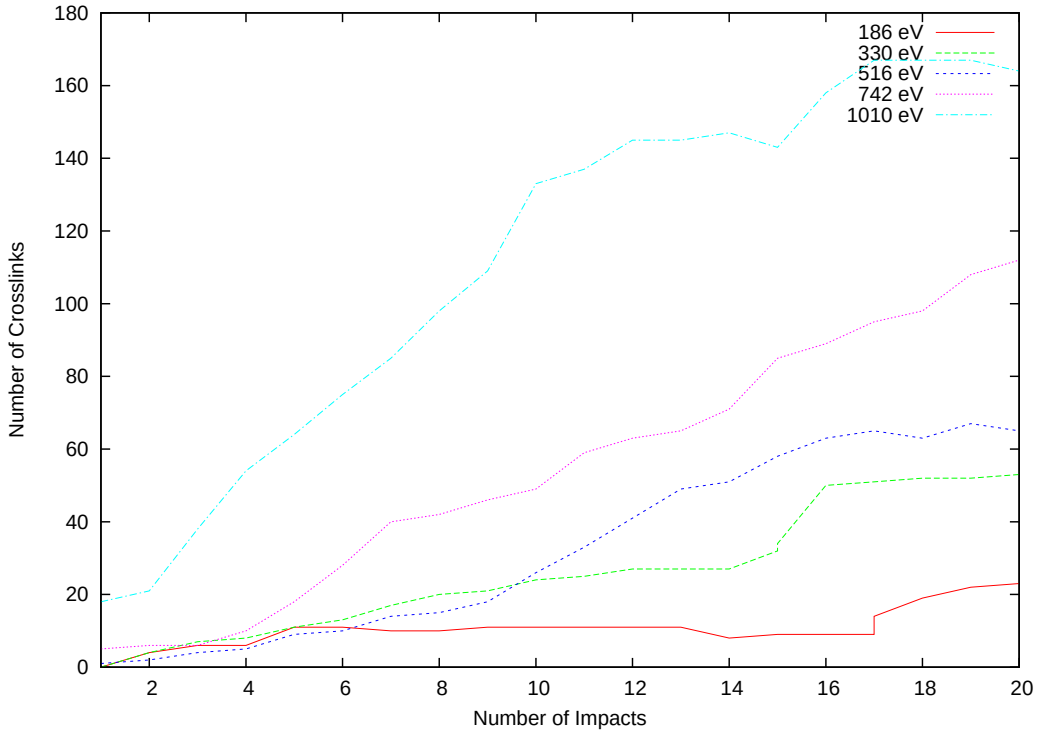

Figure 3.8 Evolution of cross-links in carbon nanotube junction formation for the (11,9)/(11,9) pair.

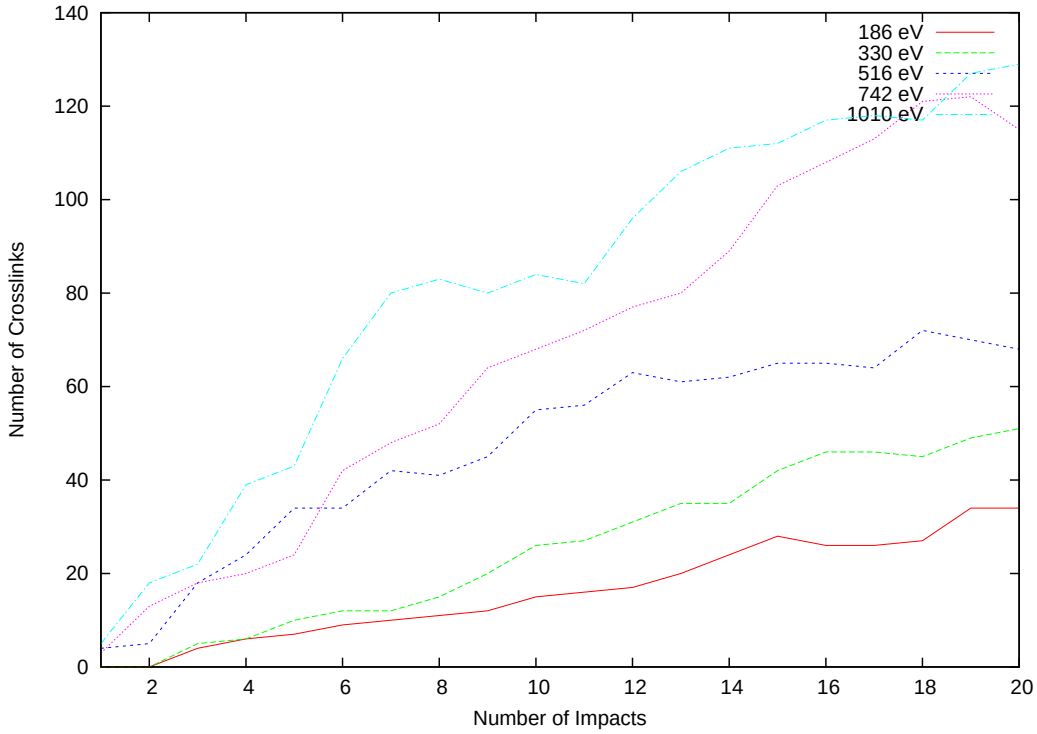

Figure 3.9 Evolution of cross-links in carbon nanotube junction formation for the (10,10)/(11,9) pair.

that the fluence of ion impacts is higher for (10,0)/(10,0) than other tubes (see Table 3.3). The same numbers of ion impacts on a smaller area will create more severe damage on the nanotube wall. For lower energies, this may not be that serious. But for higher energies like 742 eV and 1010 eV, the results are different. This phenomena is not a coincidence. The (9,0)/(9,0) combination has the second largest fluence in Table 3.3, and it has the second fewest cross-links in Figures 3.14 and 3.15.

Figures 3.16 to 3.20 show the change of *sp* carbon number with different nanotube combinations at 5 different impact energies. One important difference in the *sp* and cross-links data is that the number of *sp* carbons in larger nanotube junctions always exceed that in the smaller nanotube junctions after 20 impacts except (10,0) at 330 eV. This is probably because of the large number of carbons in the impact zone. Those carbons provide an abundant source for bond breaking reaction, and *sp* carbons are the most easily formed product of the bond breaking reaction.

The plateau of *sp* carbon number for smaller nanotubes at energies 516 eV, 742

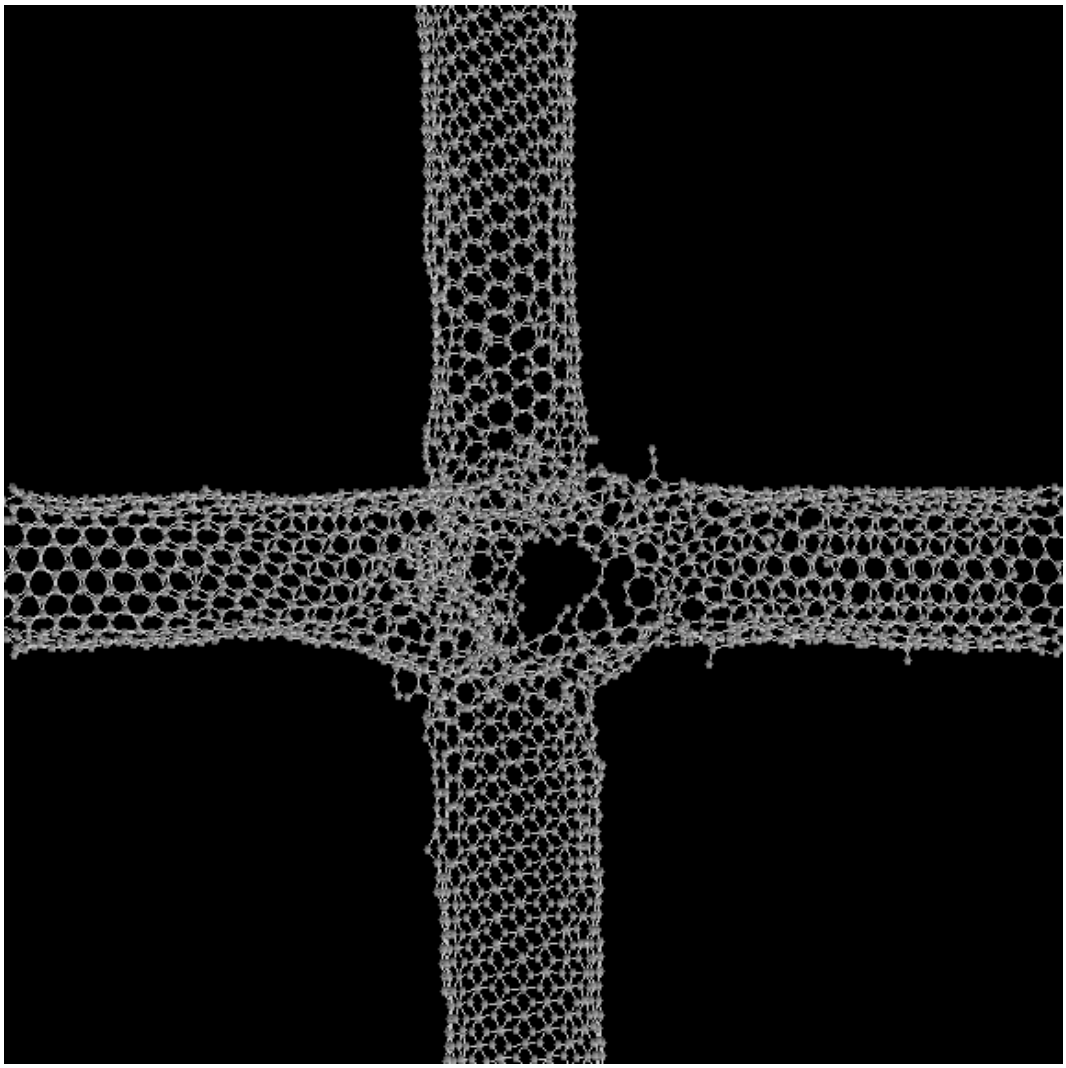

Figure 3.10 (10,10)-(10,10) carbon nanotube junction after 20 impacts at energy 742 eV.

eV and 1010 eV also starts as early as 4th impact, as in the case of cross-links. The number range in these plateaus is higher than that for cross-links. The range of *sp* carbons is as low as 60 at 186 eV , as high as 170 at 1010 eV.

The ratio of *sp* carbons and cross-links is a good indication of the nanotube junction quality. More *sp* carbons means more dangling bonds. More cross-links means more bond forming. Better nanotube junctions require a lot of cross-links. So a good nanotube junction can be indicated by a smaller *sp*/cross-links ratio.

Figure 3.21 shows the evolution of the *sp*/cross-links ratio for (10,0)/(10,0) nanotubes at 5 different impact energies. There is an apparent decrease of *sp*/cross-links

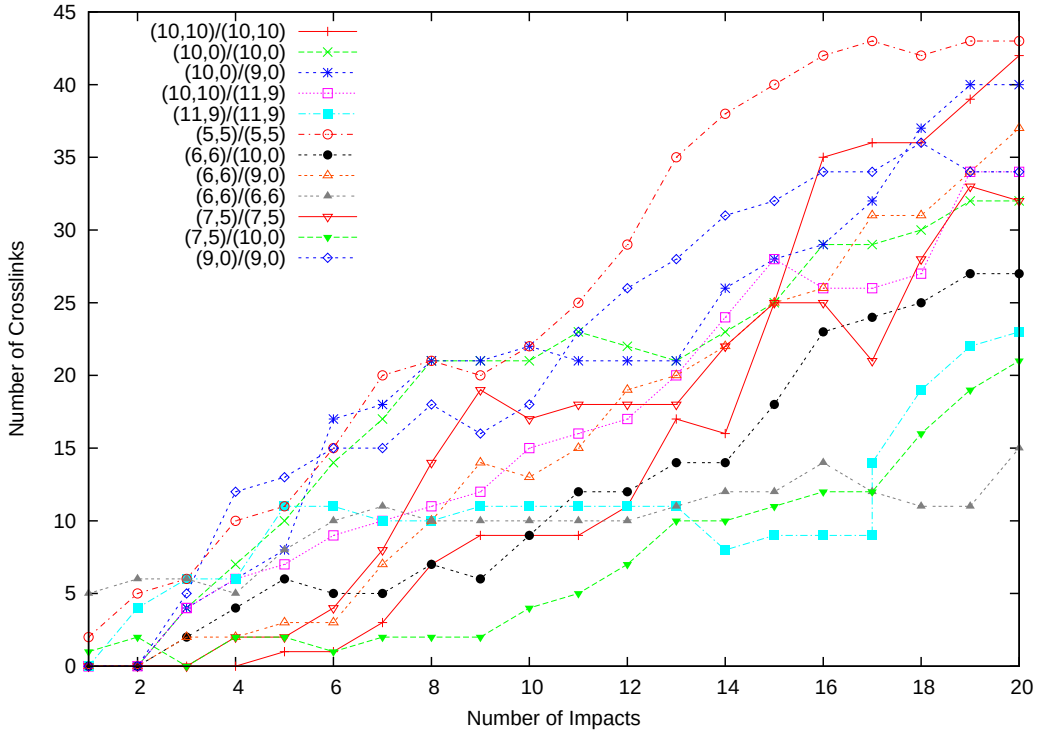

Figure 3.11 Evolution of cross-links at 186 eV for different combinations of nanotubes.

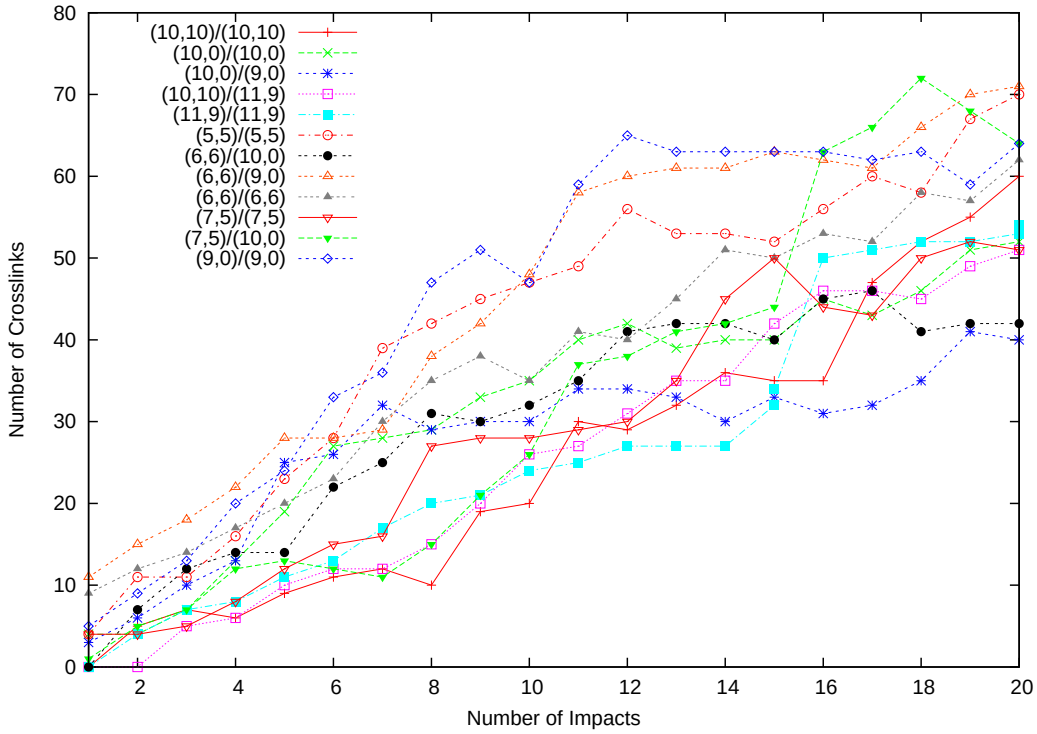

Figure 3.12 Evolution of cross-links at 330 eV for different combinations of nanotubes.

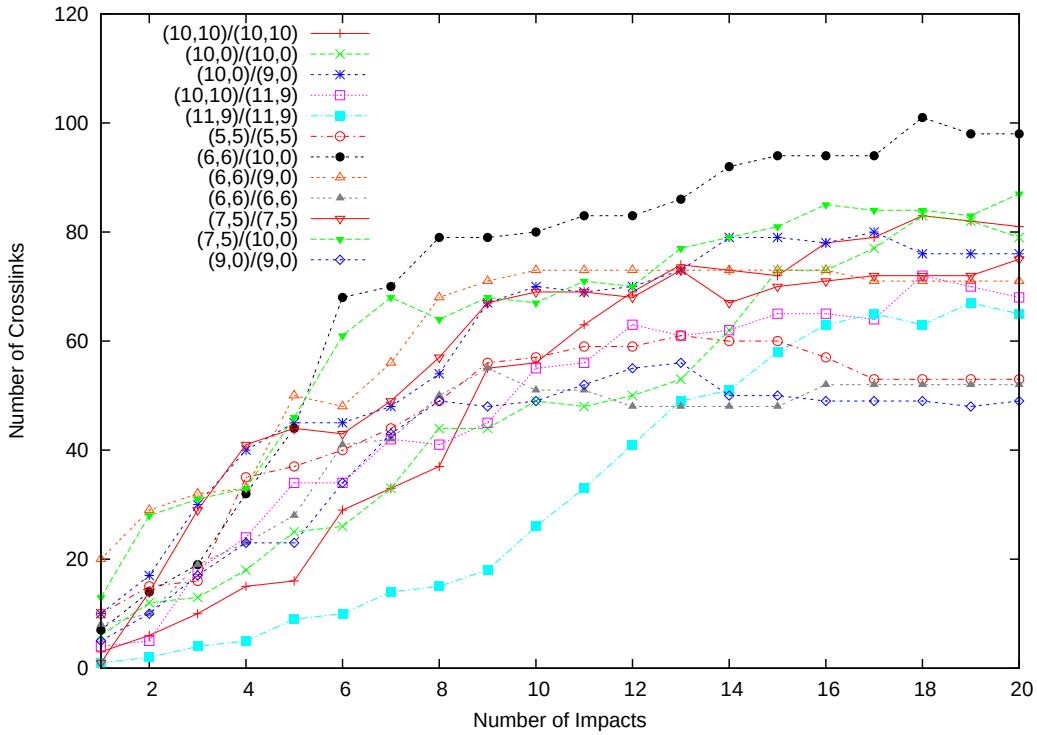

Figure 3.13 Evolution of cross-links at 516 eV for different combinations of nanotubes.

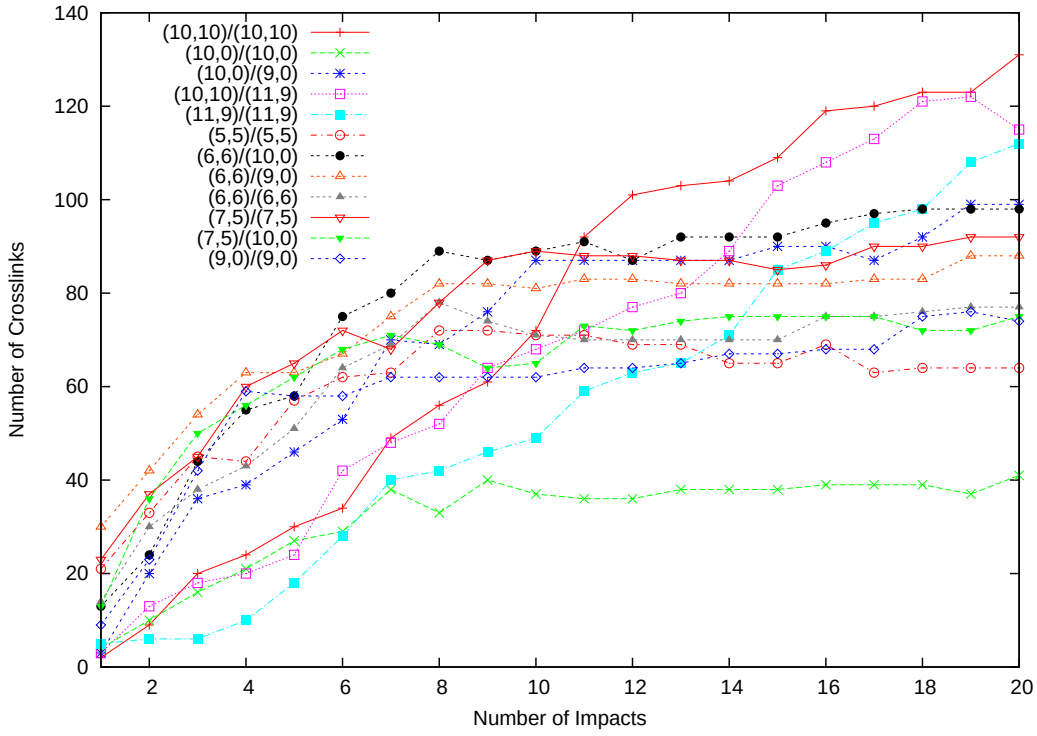

Figure 3.14 Evolution of cross-links at 742 eV for different combinations of nanotubes.

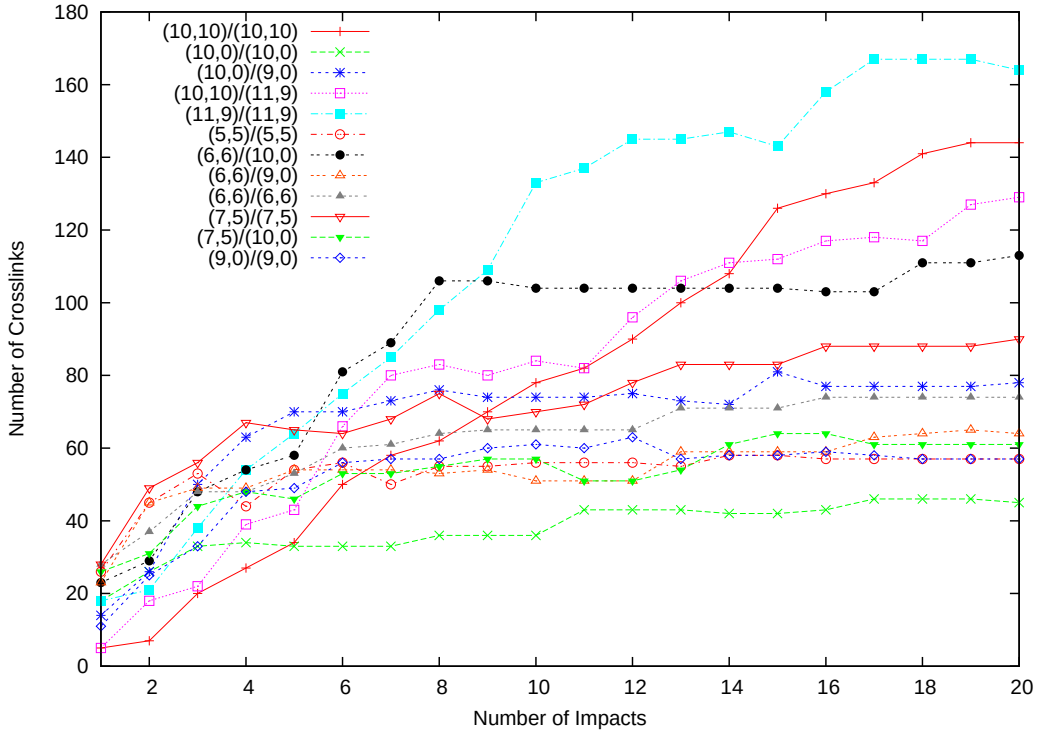

Figure 3.15 Evolution of cross-links at 1010 eV for different combinations of nanotubes.

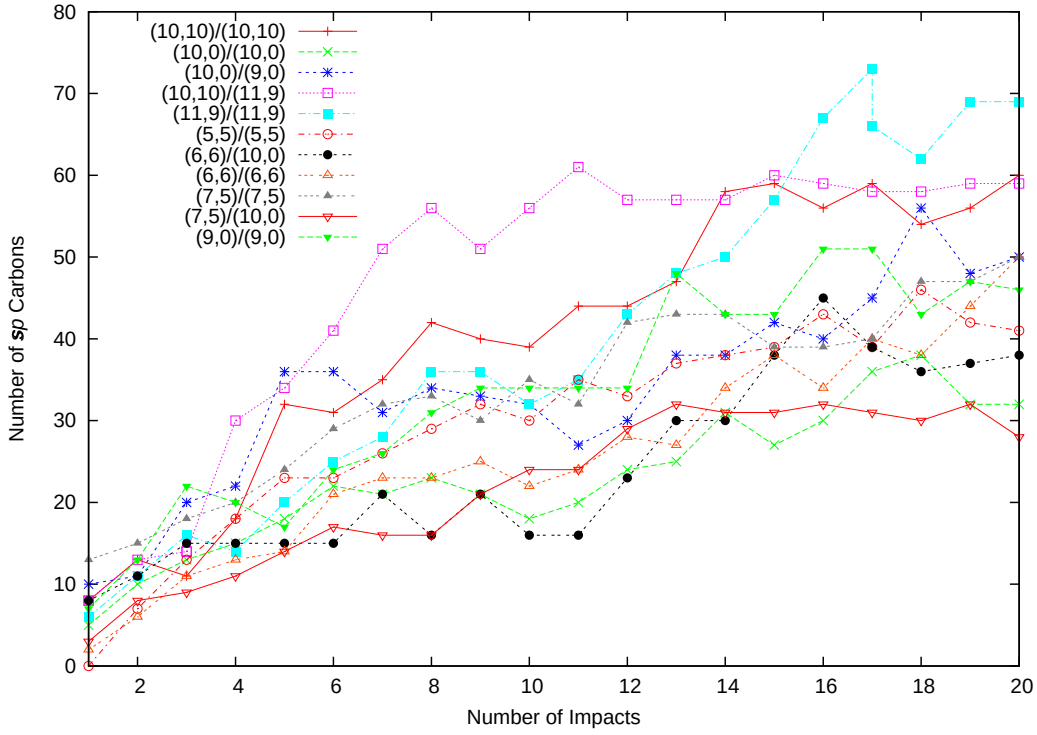

Figure 3.16 Evolution of *sp* carbon at 186 eV for different combinations of nanotubes.

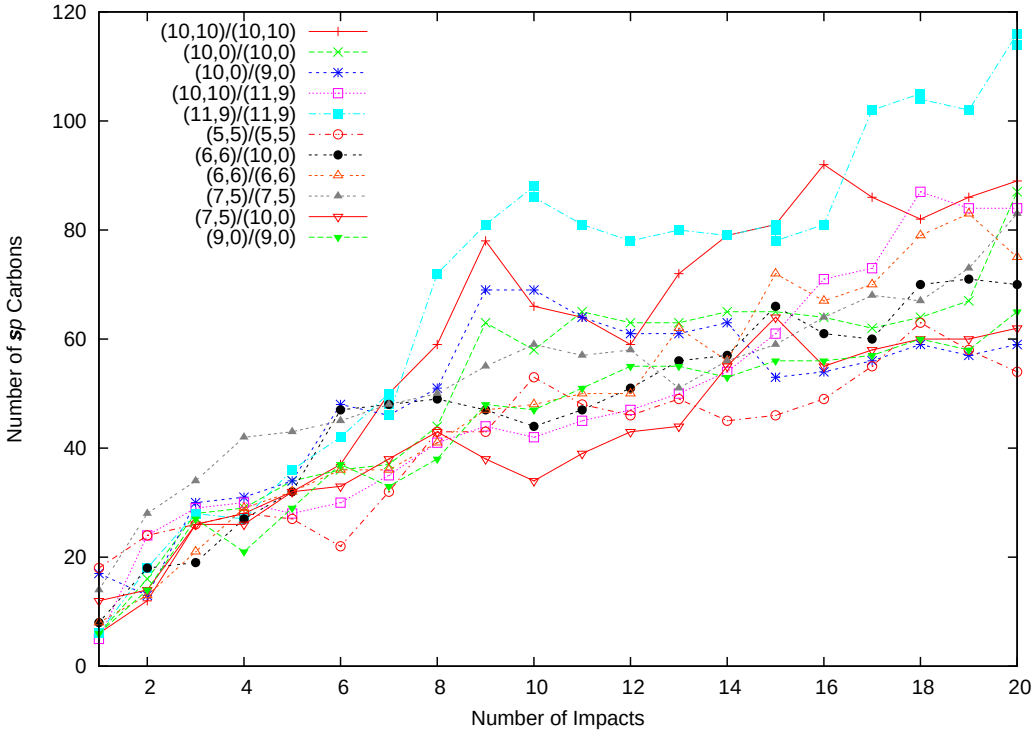

Figure 3.17 Evolution of *sp* carbon at 330 eV for different combinations of nanotubes.

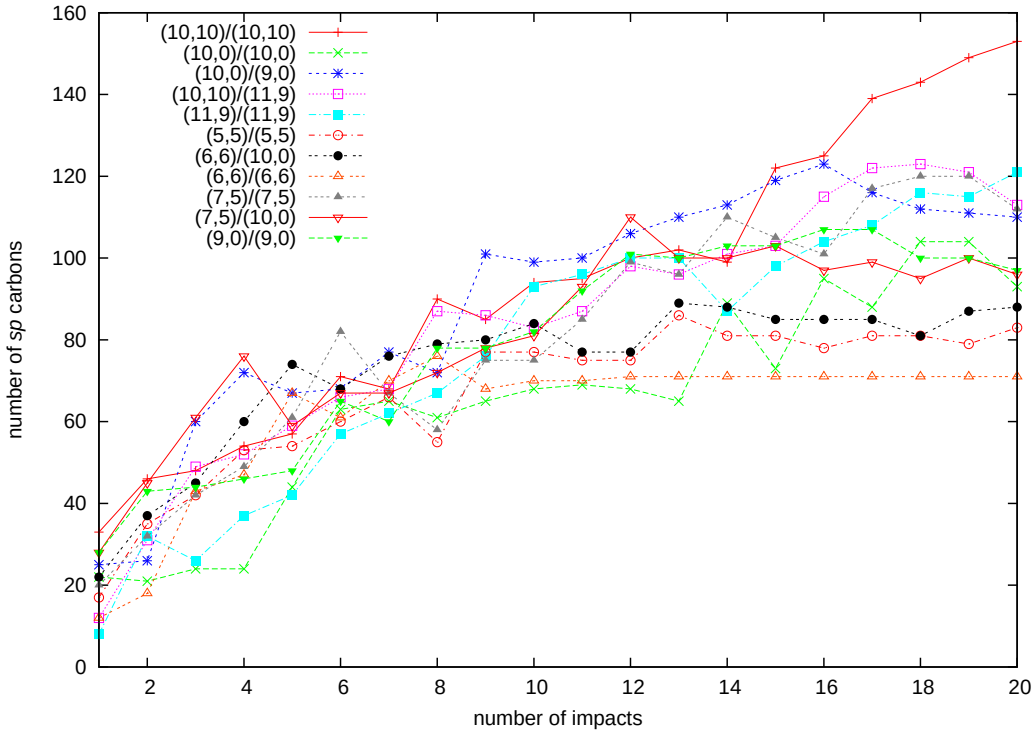

Figure 3.18 Evolution of *sp* carbon at 516 eV for different combinations of nanotubes.

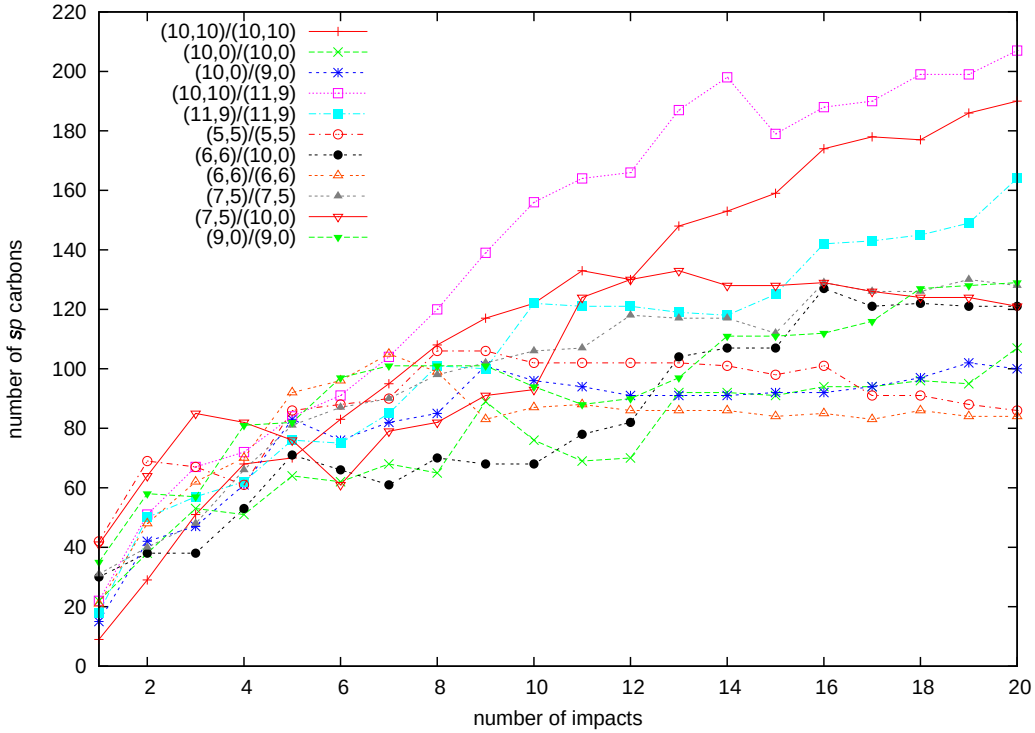

Figure 3.19 Evolution of *sp* carbon at 742 eV for different combinations of nanotubes.

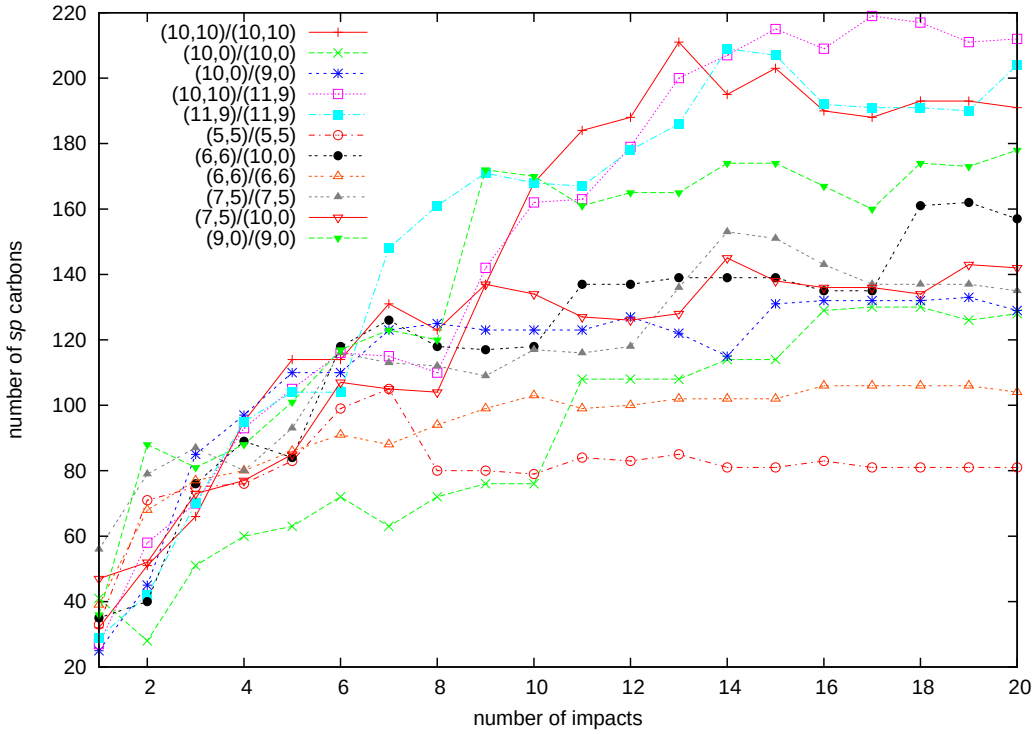

Figure 3.20 Evolution of *sp* carbon at 1010 eV for different combinations of nanotubes.

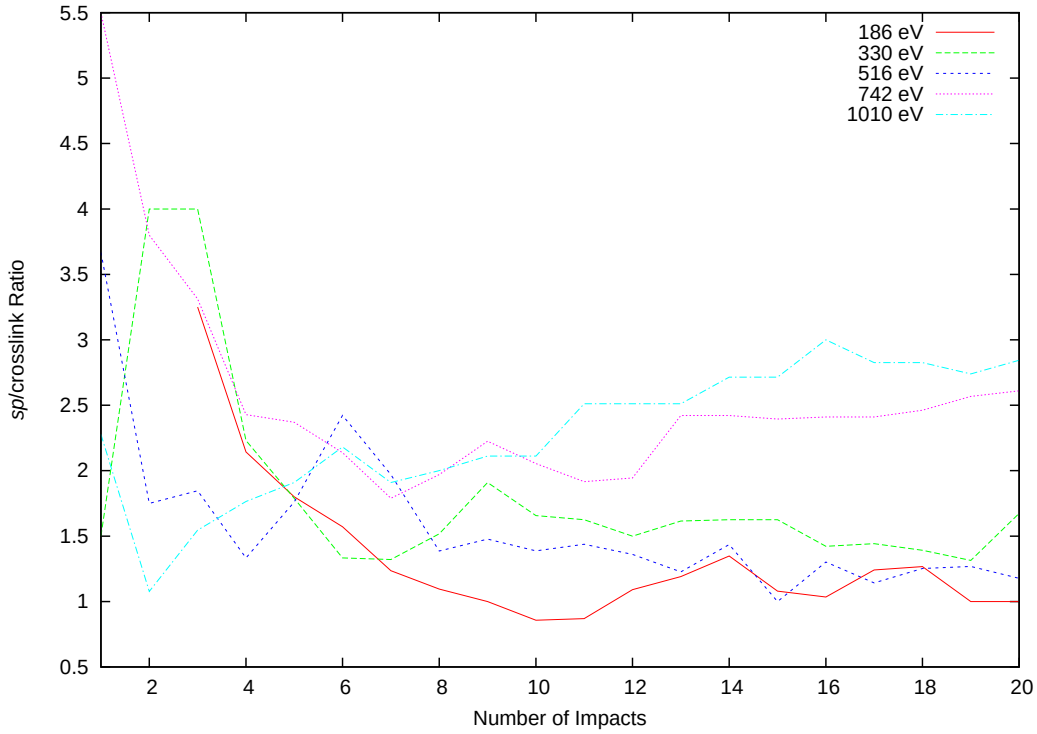

Figure 3.21 Evolution of the *sp*/cross-links ratio for (10,0)/(10,0) nanotubes at 5 different impact energies.

ratio at impact energy 186 eV. The final value is close to 1. At energy 330 eV, 516 eV, and 742 eV, similar trends can be found, except that the final value is higher than that of 186 eV. At energy 1010 eV, we actually see a initial decrease of ratio at the first several impacts, followed by a increase trend. This could signal a bad junction formation or continued damage to the junction. The detailed discussion of conductivity is conducted in section .

For large nanotubes, the situation is different. Figures 3.22, 3.23, and 3.24 all show a continued decrease of the *sp*/cross-links ratio at all 5 impact energies, except in the case of (11,9)/(11,9) at energy 186 eV. In general, for large nanotubes, more fluence is better. Further examination reveals that for impact energies 330 eV, 516 eV, 742 eV, and 1010 eV, the ratio becomes stable after the 16th impact in all three combinations.

The number of sp^3 carbons is shown in Figure 3.25 for all pairs at 330 eV. This is a typical sp^3 figure. Other figures under different energies are not shown because

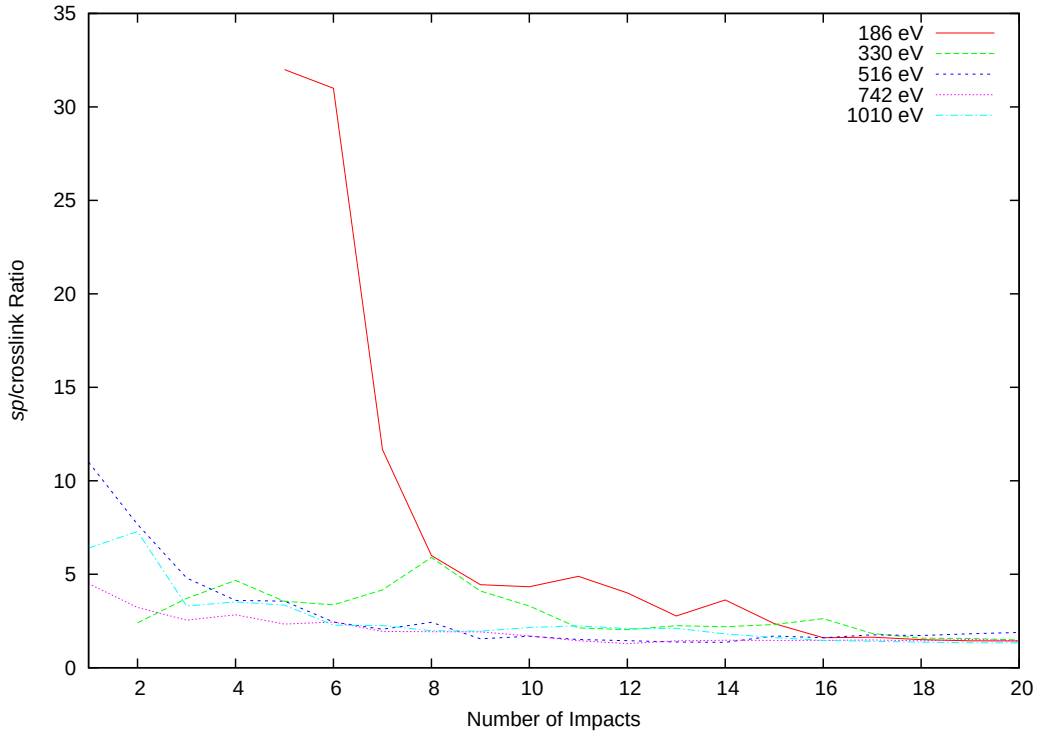

Figure 3.22 Evolution of the *sp*/cross-links ratio for (10,10)/(10,10) nanotubes at 5 different impact energies.

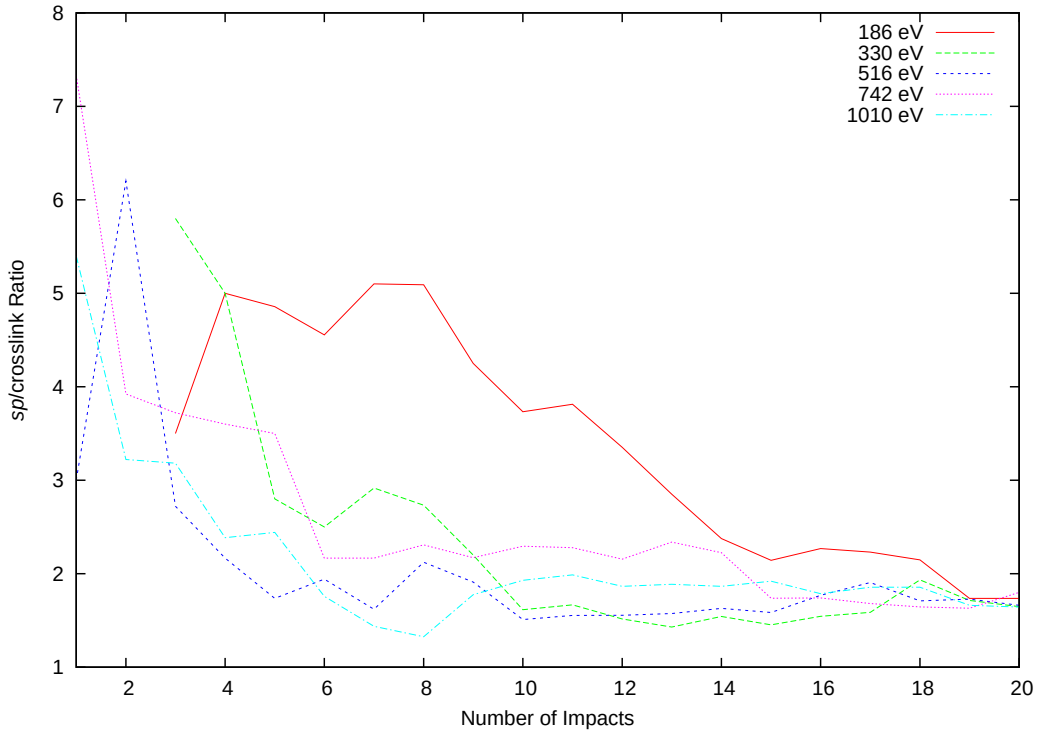

Figure 3.23 Evolution of the *sp*/cross-links ratio for (10,10)/(11,9) nanotubes at 5 different impact energies.

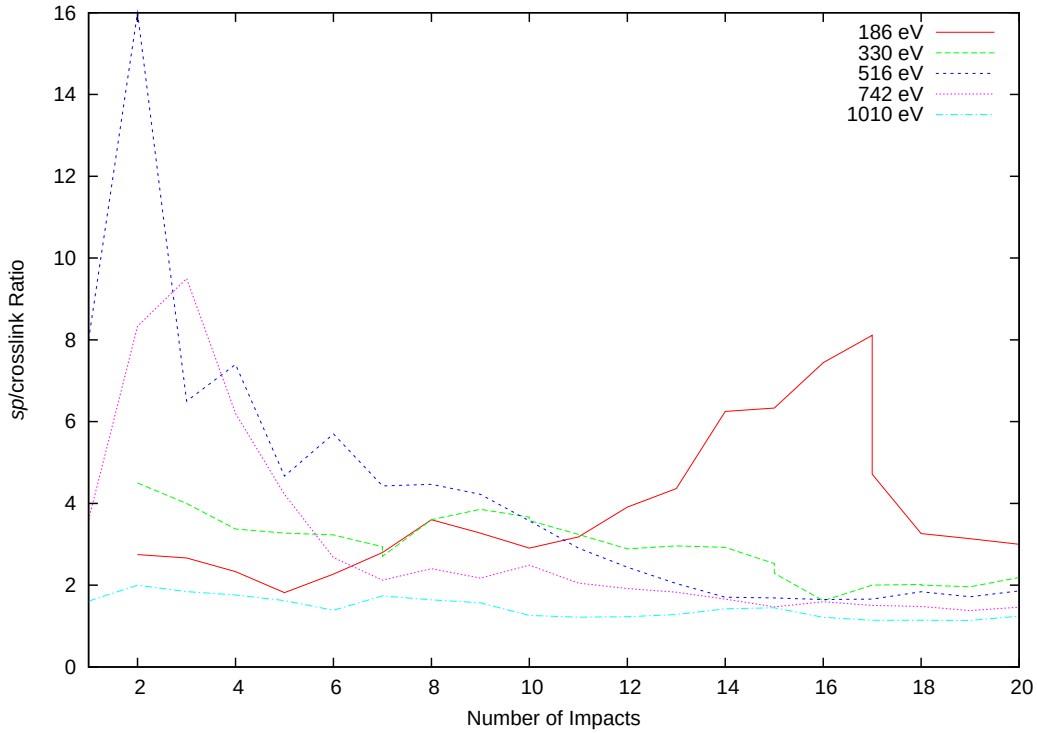

Figure 3.24 Evolution of the *sp*/cross-links ratio for (11,9)/(11,9) nanotubes at 5 different impact energies.

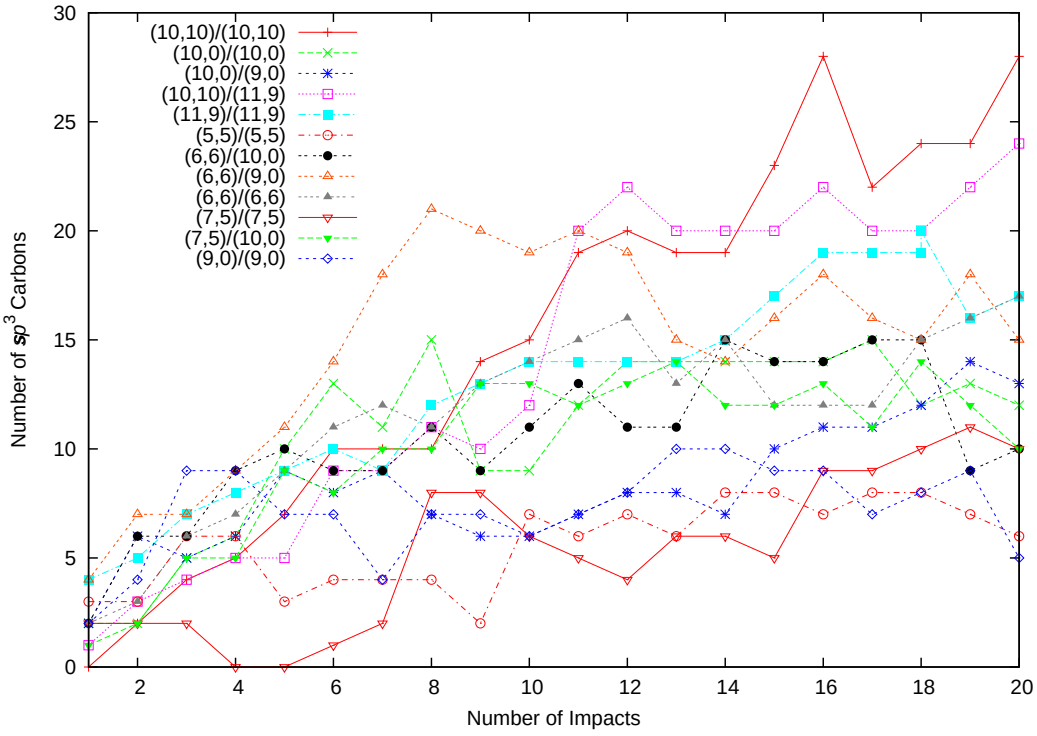

Figure 3.25 Evolution of sp^3 carbon at 330 eV for different combinations of nanotubes.

they are very similar to Figure 3.25. We can see from this figure that the number of sp^3 carbon species is much smaller than the number of sp carbon atoms. The number is mostly between 5-15 for small nanotubes and 15-25 for large nanotubes. Carbon atoms in the sp^3 hybridization state are stable in nature and do not easy to react with other carbons.

Effects of Relaxation and Cooling Time

Comparison of ion irradiation with different relaxing and cooling times is performed on the (10,0)/(10,0) combination. One combination uses the standard procedure, another one uses a procedure with longer cooling and relaxing period. Both periods are doubled from the standard procedure.

Figures 3.26 and 3.27 show the evolution of cross-links in these two cases. One observation at the low energy of 186 eV is that cross-links in standard procedure has a fast increase before 8th impact and a steady slow increase after that. The longer relaxation procedure starts from a slow increase and continues with a fast increase after 16th impact. After 20 impacts, the longer relaxation procedure has close to 50 cross-links vs. a little more than 30 cross-links in standard procedure. Note that in Figure 3.27, cross-links are formed after first impact, earlier than in Figure 3.26. For higher energy at 742 eV, we see a plateau of 35 in Figure 3.26 after 8th impact. But in Figure 3.27, a much higher plateau of 70 is found before 9th impact. A examination of coordinate files found that one nanotube half is disconnected from the rest after 9th impact in Figure 3.27. This confirms that higher impact energies and large fluence are dangerous for small nanotube welding. These observations demonstrate that longer relaxation and cooling time helps cross-links formation, but it cannot save the nanotube from high energy damage.

Figures 3.28 to 3.35 show evolution of various defects at 4 different energies. The most significant observation at 186 eV is the smaller number of sp^3 and s carbon defects with the larger relaxation and cooling periods than with the shorter ones. They are less than 10 compared to 20 in Figure 3.28. The reason may be that more time is allowed for carbons interact with other carbons in nanotube structure before

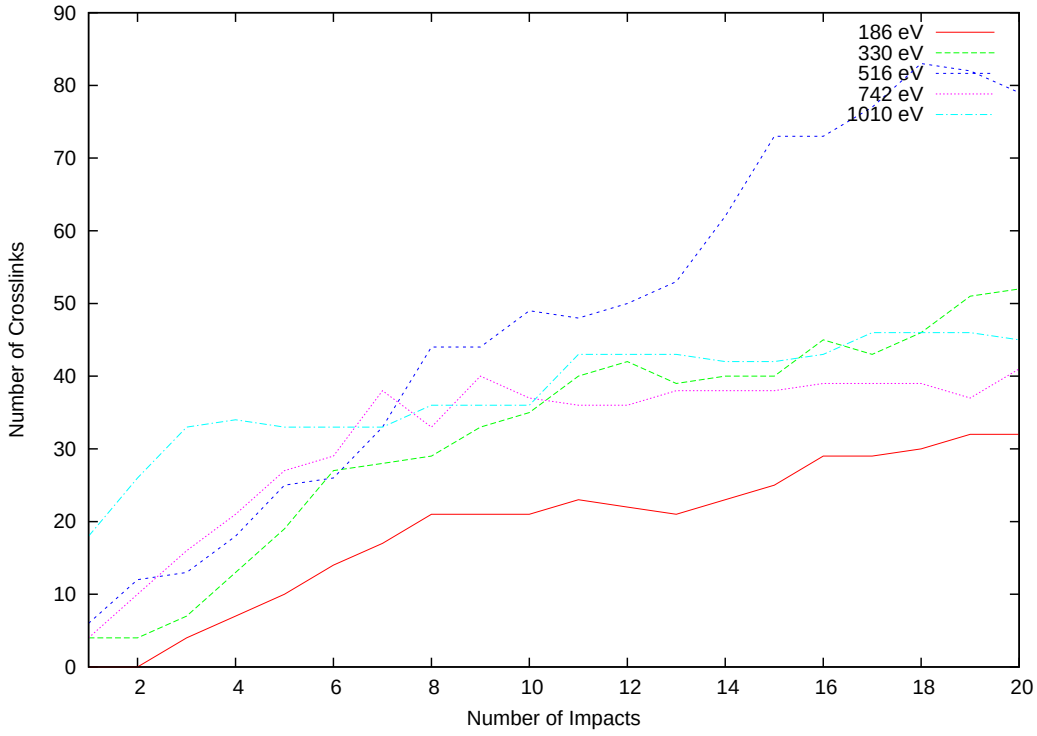

Figure 3.26 Evolution of cross-links in carbon nanotube junction formation for the (10,0)/(10,0) pair (standard relaxation and cooling time).

next impact. They will have better chance to form bond and stay in nanotube body. It also can explain the larger number of single carbons (10 compare to 5 in Figure 3.28) in Figure 3.29. Similar results can be found in Figure 3.30 and 3.31 at 330 eV.

The situation at higher energies is different. The number of single and *s* carbons are similar between the standard procedure and long relaxation time procedures. At 516 eV, there are 52 single carbons and 37 *s* carbons in the standard procedure simulation, and the corresponding numbers for the long relaxation time procedure are 51 and 43. At 742 eV, the numbers are 84 and 66 in standard procedure simulation, and 71 and 55 for long relaxation time procedure. This seems to imply that long relaxation time at high energy is not as important as at low impact energy.

Conductivity

The conductivity of the nanotube junction is another important diagnostic of the quality of the nanotube junction. Figures 3.36 through 3.39 show the evolution of the conductance of the (10,0)/(10,0) nanotube system under 5 different bombardment

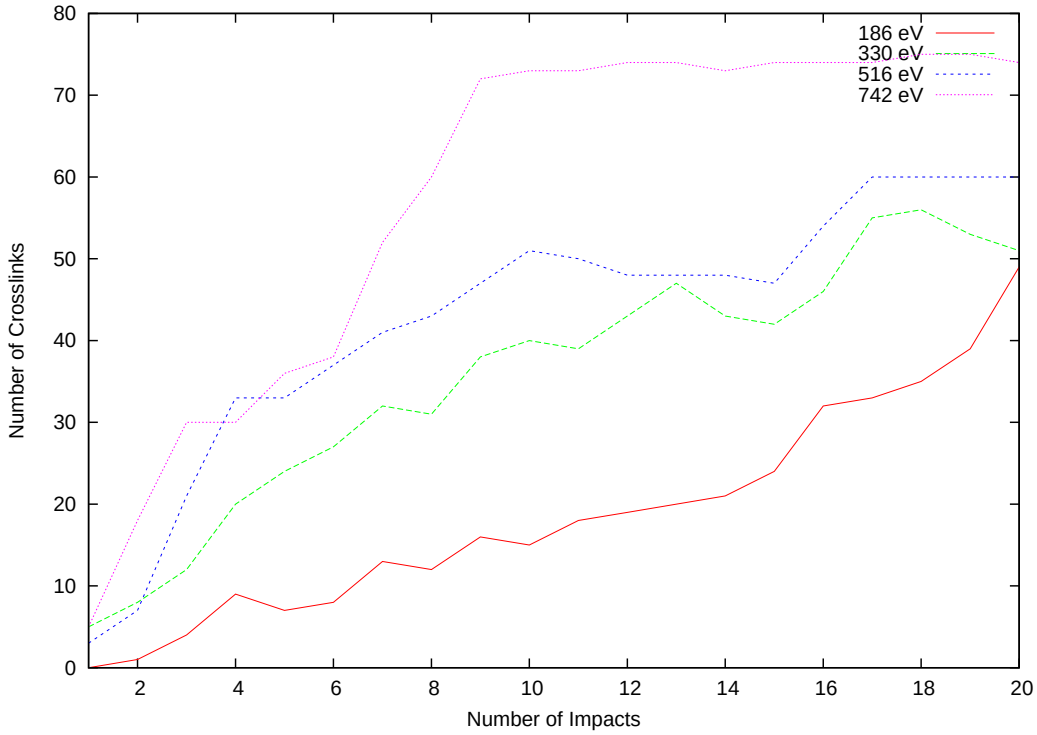

Figure 3.27 Evolution of cross-links in carbon nanotube junction formation for the (10,0)/(10,0) pair (longer relaxation and cooling time).

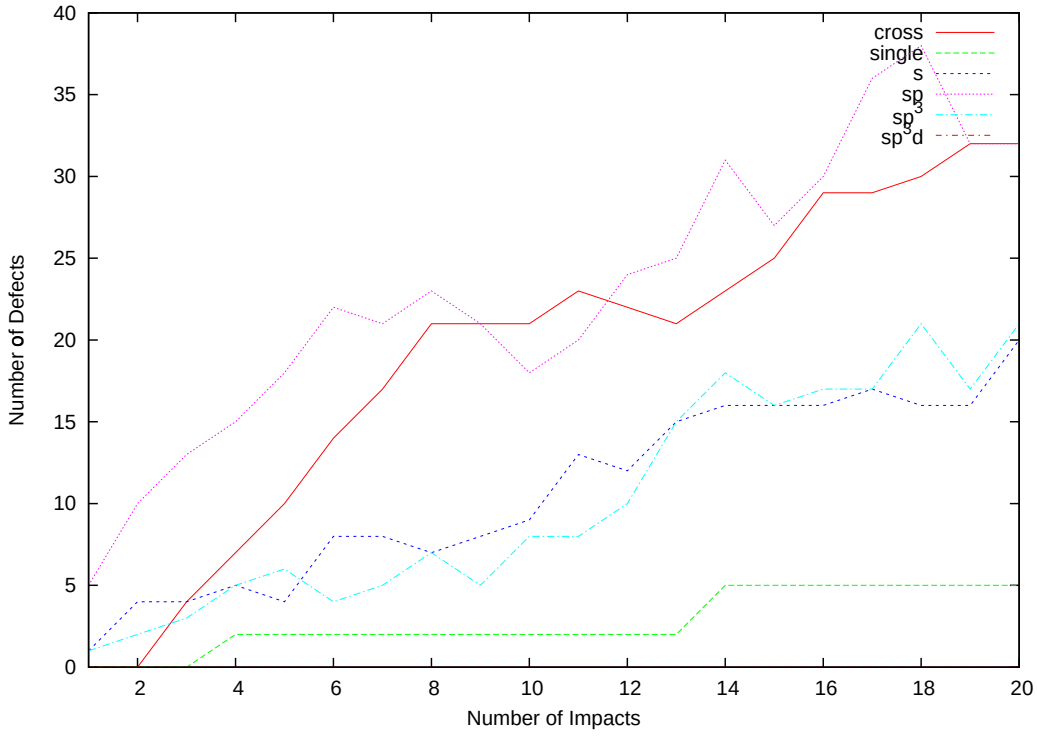

Figure 3.28 Evolution of defects in carbon nanotube junction formation for the (10,0)/(10,0) pair at 186 eV (standard relaxation and cooling time).

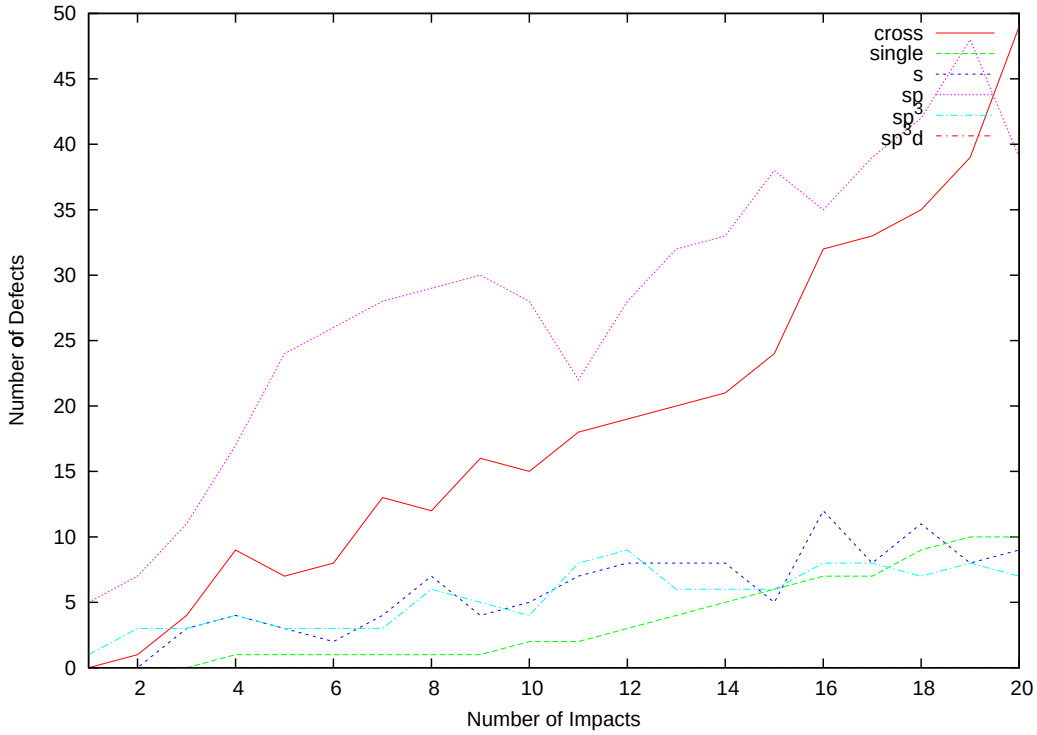

Figure 3.29 Evolution of defects in carbon nanotube junction formation for the (10,0)/(10,0) pair at 186 eV. (long relaxing and cooling time).

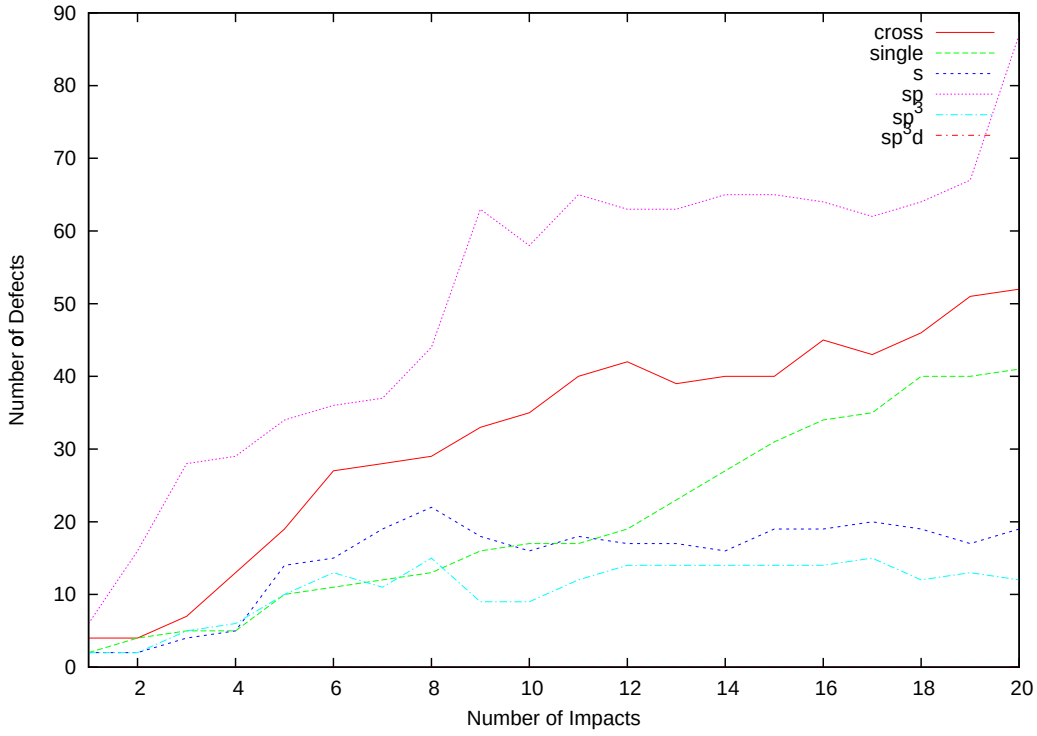

Figure 3.30 Evolution of defects in carbon nanotube junction formation for the (10,0)/(10,0) pair at 330 eV (standard relaxation and cooling time).

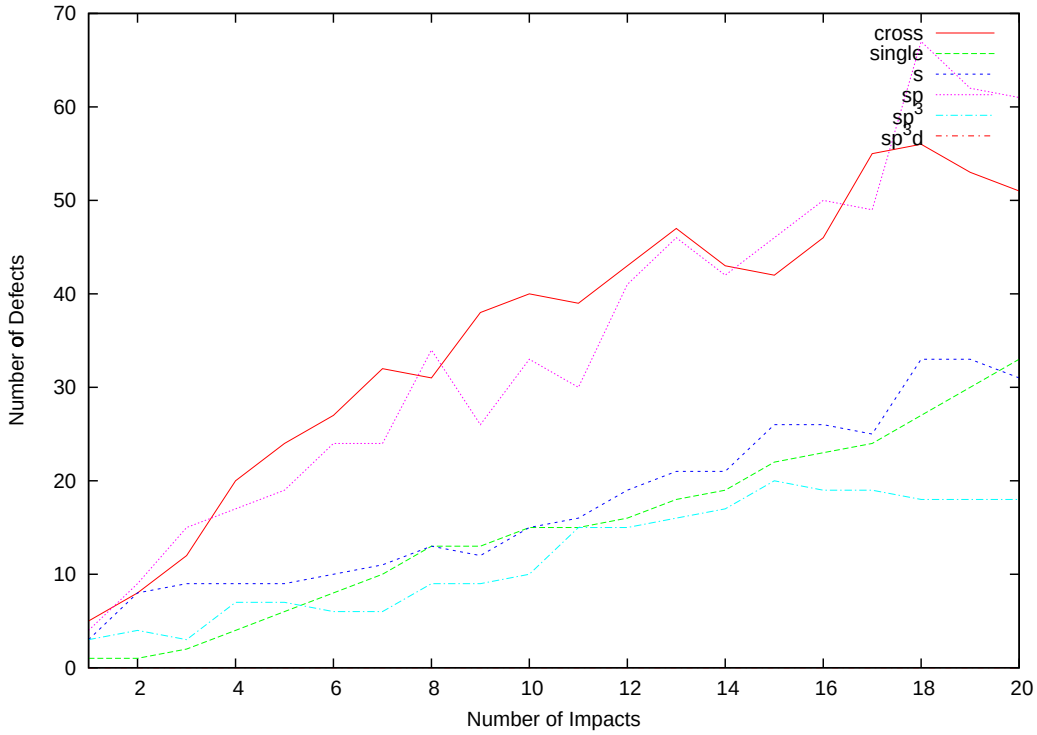

Figure 3.31 Evolution of defects in carbon nanotube junction formation for the (10,0)/(10,0) pair at 330 eV (long relaxing and cooling time).

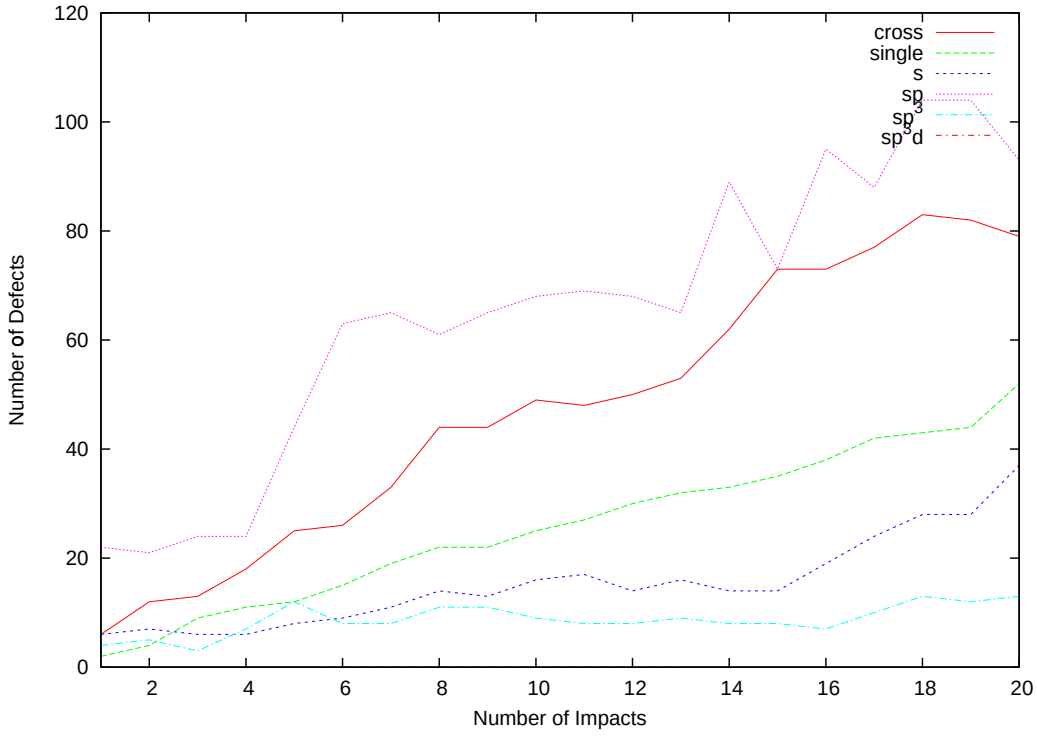

Figure 3.32 Evolution of defects in carbon nanotube junction formation for the (10,0)/(10,0) pair at 516 eV (standard relaxation and cooling time).

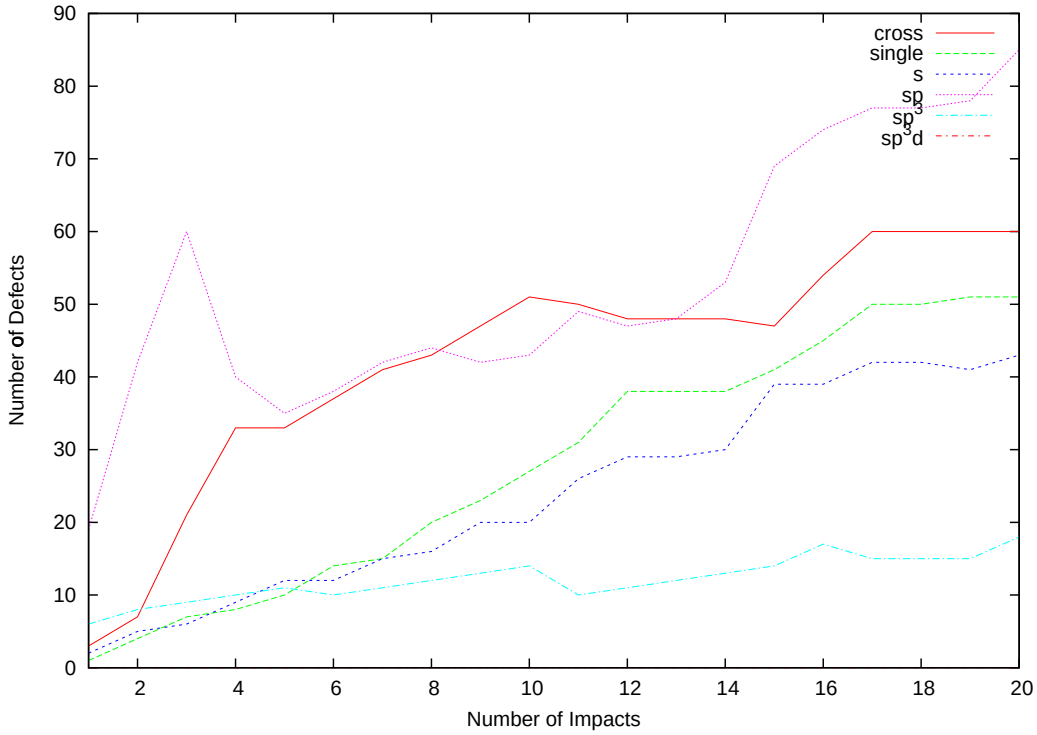

Figure 3.33 Evolution of defects in carbon nanotube junction formation for the (10,0)/(10,0) at pair 516 eV (long relaxing and cooling time).

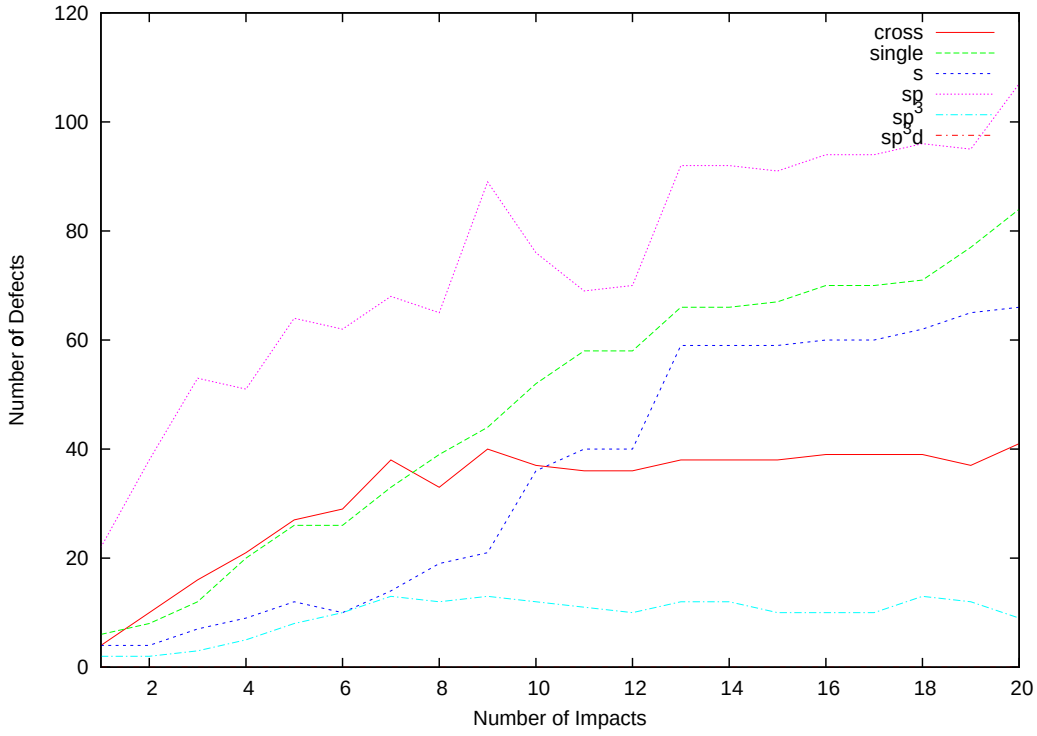

Figure 3.34 Evolution of defects in carbon nanotube junction formation for the (10,0)/(10,0) at pair 742 eV (standard relaxation and cooling time).

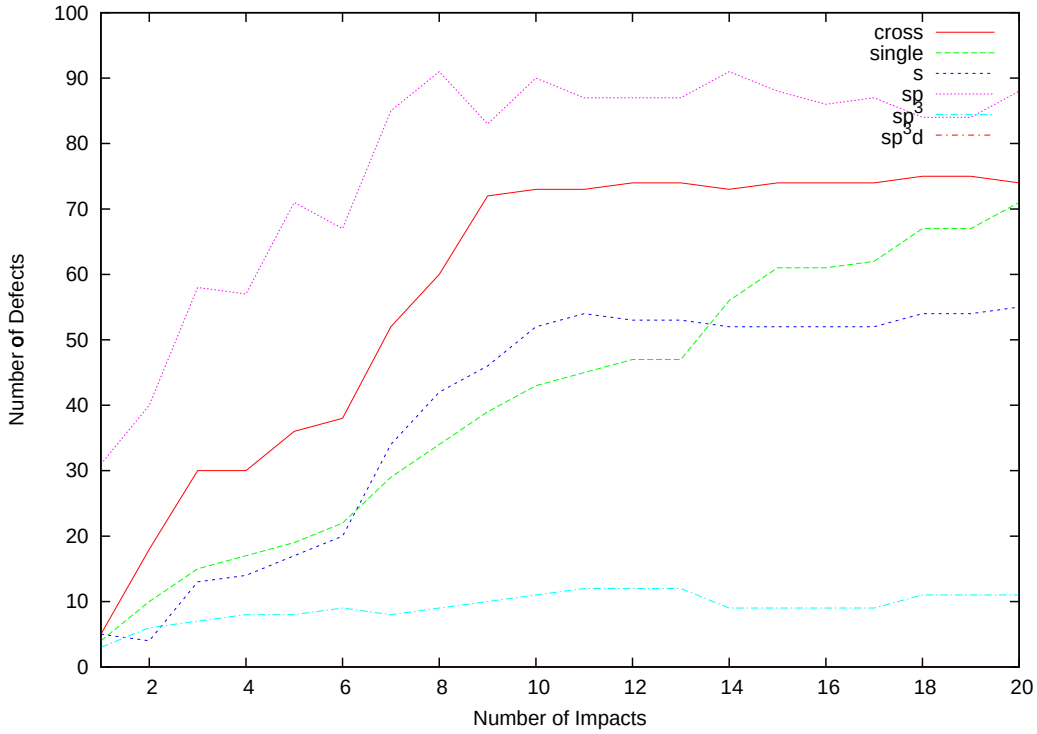

Figure 3.35 Evolution of defects in carbon nanotube junction formation for the (10,0)/(10,0) at pair 742 eV (long relaxing and cooling time).

energies. The terminals are labeled as shown in Figure 3.40. Terminals 1 and 2 are the two ends of same nanotube on the top. Terminals 3 and 4 are the two ends of same nanotube on the bottom. The conductance is calculated for each of the terminal pairs that had no electrical connection in the original unwelded pair: the 1-3, 1-4, 2-3, and 2-4 terminal pairs. Figures 3.36 to Figure 3.39 show the conductance between terminals 1-3, 1-4, 2-3, and 2-4 respectively. At the beginning of simulations, there is no connection between these two nanotubes. Thus the conductances in these graph at time 0 is 0 before first impact.

At 186 eV, the conductance becomes non-zero after 3 impacts. Close examination of nanotube structure found that during the first two impacts, no damage is made to the bottom nanotube. (The low incoming energy of the Ar ion creates a hole of 5 Å in size on the top nanotube.) After the third impact, a hole of ~ 4Å is created on bottom tube, and cross-links begin to appear (see Figure 3.26). After 6 impacts, conductance becomes stable at a value of 0.4 $(2e^2/h)$ to 0.7 $(2e^2/h)$ depending on the

terminal pair.

Conductances under 186 eV bombardment are always stable in all four combination of terminals. This proves that a continuous lower energy ion irradiation can successfully weld nanotubes together.

For the highest energy of 1010 eV, the first few impacts create conductivity in nanotube junction. The junction formed is of a high quality, as judged by conductance. For the 2-3 pair, the conductance ranges from 0.6-0.9 until the 10th impact, higher than for the junctions formed at lower energies. Figure 3.40 shows that the physical connection between these terminals is quite good. But after the 11th impact, we can see a sharp decrease of conductance (see Figures 3.38 and 3.39). There must be a high energy impact in the region where the junction formed. The connection between terminals 2 and 3 was completely cut off. After that, the junction disappeared and never recovered. The conclusion can be drawn that the bridge between terminal 2 and the rest of the junction was broken. Figure 3.41 confirms this conclusion. An examination of Figure 3.36 and 3.37 has similar results, except that the disconnection between terminal 1 and the rest of the junction happened after the 16th impact. From Figure 3.40 we can also find that terminal 1 connected with terminal 4 better than with terminal 3 and terminal 2 with terminal 3 better than with terminal 4. Thus the observation in Figure 3.36 and 3.37 that at the 10th impact, conductance between 1 and 4 is much larger (0.3) than that of 1 and 3 (0.1). The same thing is true for the 2-3 and 2-4 terminal pairs from Figure 3.38 and 3.39.

In the case of moderate energy impacts, conductivity is non-zero from the first impact. With increasing number of impacts, conductance fluctuates around 0.4 to 0.6. No clear pattern can be observed from the conductance data. None of them had a total disconnection between nanotubes. But a decrease of conductance at lower fluence can be found in some case. For example, in Figure 3.37, the conductance under 742 eV bombardment decreased after the 13th impact, and then remained at a low level. Similiar behaviors can be seen at energy 516 eV in Figure 3.37, 330 eV in Figure 3.38, and 742 eV in Figure 3.39.

In all four combination of terminals, only at the lowest energy of 186 eV, does the

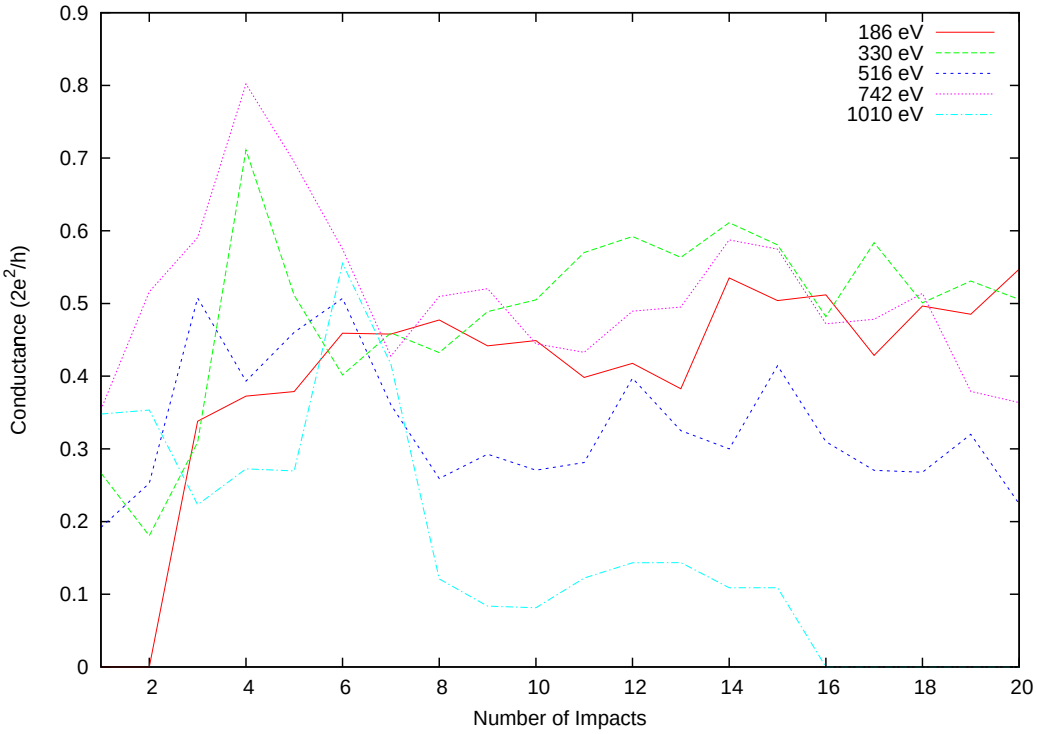

Figure 3.36 Evolution of conductance between terminals 1-3 for the (10,0)/(10,0) nanotube junction at different energies.

conductance remain constant increase for all 20 impacts. At the end of 20 impacts, the conductance at 186 eV was always the highest. The conclusion may be drawn that for the (10,0)/(10,0) combination, bombardmant at a low energy (186 eV) at a high fluence ($\sim 10 \times 10^{15} cm^{-2}$) ion irradiation will create the optimal junction and conductivity. A high energy at low dose may have similar result, although the results are more sensitive to stopping at the appropriate fluence.

Conclusion

From this work, a few conclusions can be drawn. The energy of impact ions plays an important role in nanotube reconstruction. If the energy is too high, damage caused by collisions between ions and carbons can become irreparable. This means the structure of the nanotube will be destroyed. We found that 742 eV and 1010 eV impact energies are appropriate for large diameter nanotubes (10,10), (11,9), based on the number of crosslinks created and ratio of *sp*/cross-links. Physical examinations confirmed that the nanotube structure retained its shape. For small nanotubes, a 186

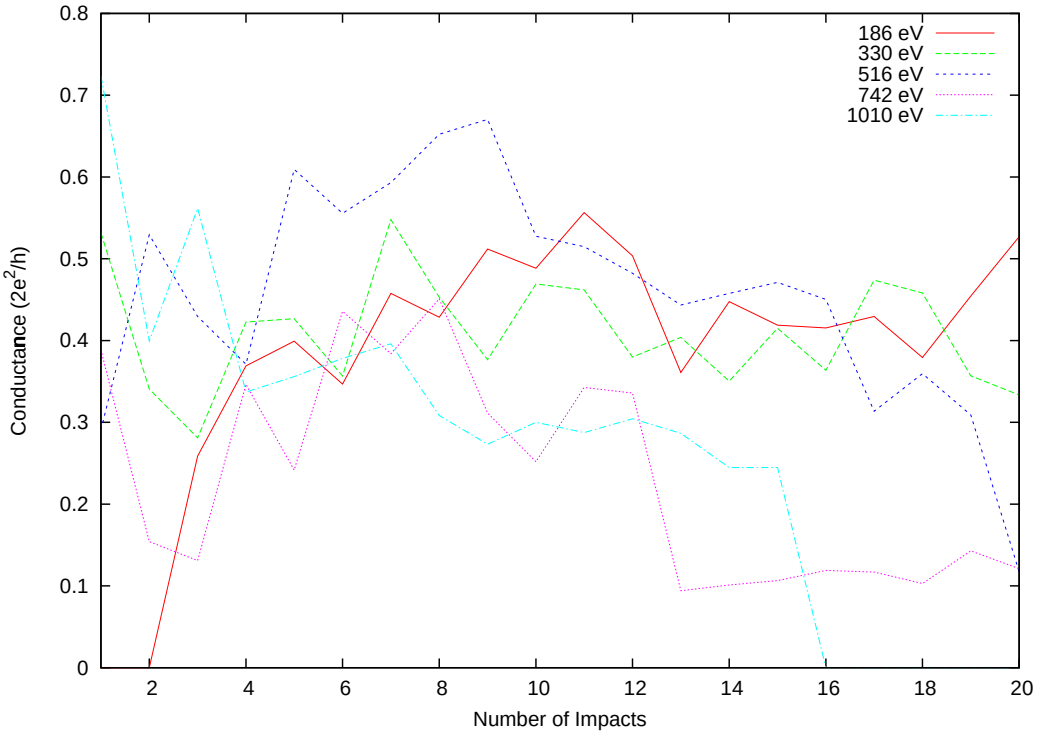

Figure 3.37 Evolution of conductance between terminals 1-4 for the (10,0)/(10,0) nanotube junction at different energies.

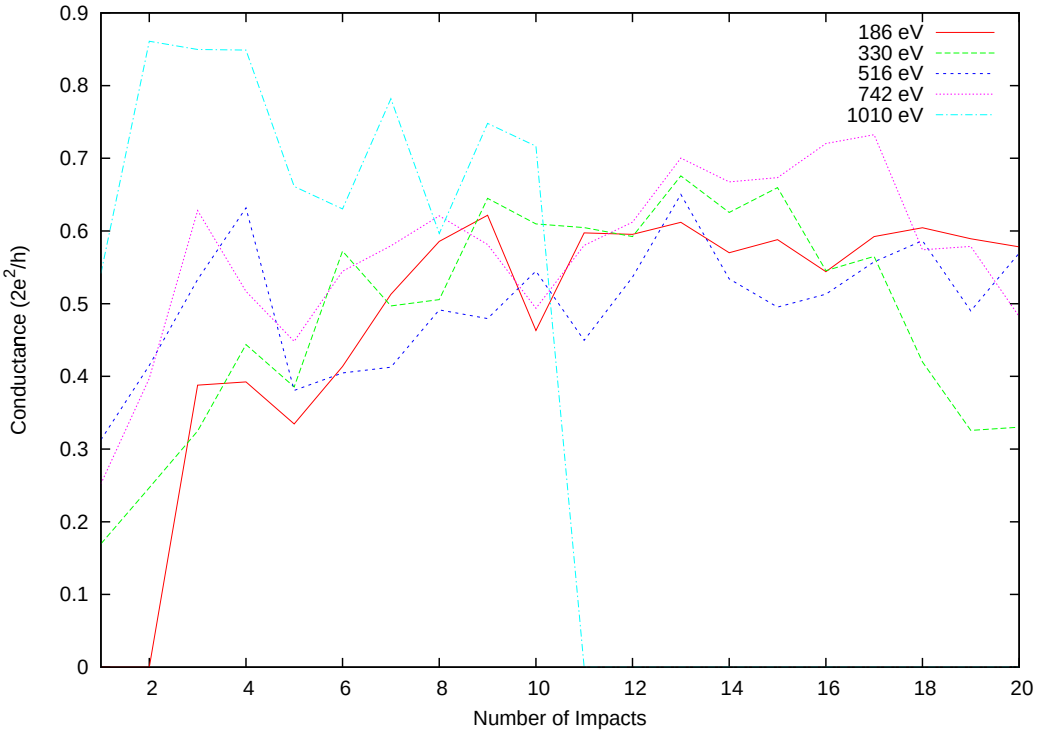

Figure 3.38 Evolution of conductance between terminals 2-3 for the (10,0)/(10,0) nanotube junction at different energies.

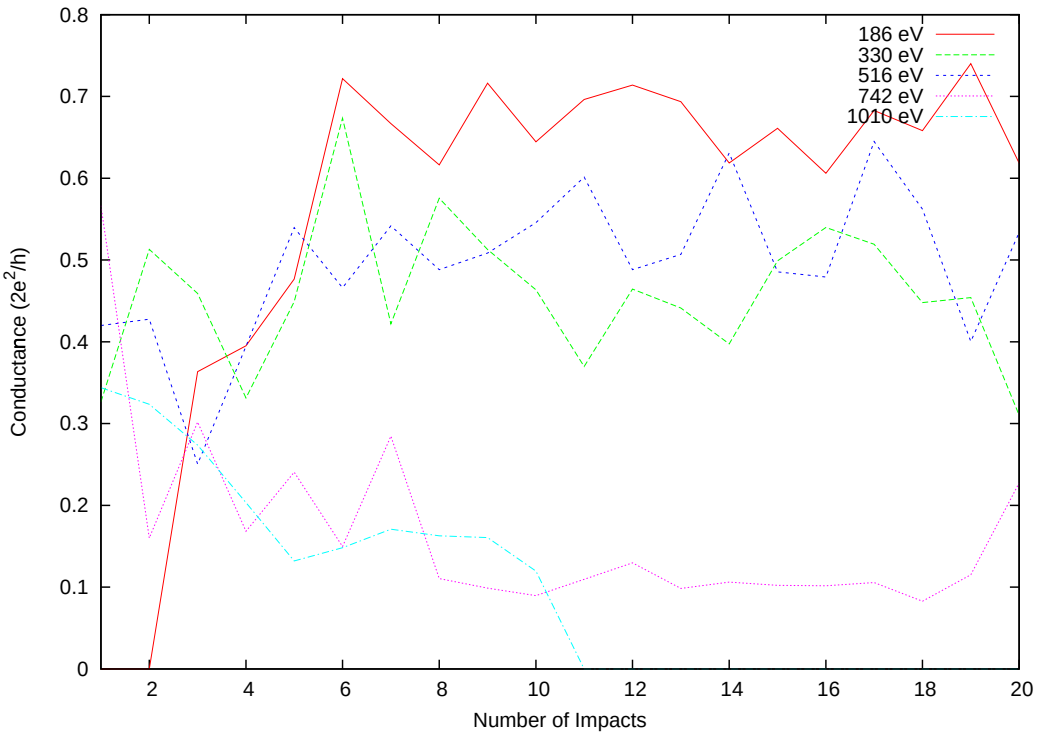

Figure 3.39 Evolution of conductance between terminals 2-4 for the (10,0)/(10,0) nanotube junction at different energies.

eV impact energy is most appropriate judging from Green's function calculations of conductivity.

The optimum fluence is associated with the size of nanotube and the impact energy. For small nanotubes with a diameter less than 10 Å, a fluence of $5 \times 10^{15}\text{cm}^{-2}$ is appropriate at lower energy (186 eV, 330 eV). A fluence of $2 - 3 \times 10^{15}\text{cm}^{-2}$ is appropriate at ion energies of 516 eV and 742 eV based on the plateau in cross-links figures. A fluence of $1 - 2 \times 10^{15}\text{cm}^{-2}$ may be used at 1010 eV, but it is not recommended to use this high energy for small nanotubes. For large nanotubes, the highest fluence in simulation is only $\sim 1.7 \times 10^{15}\text{cm}^{-2}$ due to the large size of intersection. Based on the nanotube defects created, we believe a much higher fluence will result in even better junction formation. The dose recommended in Krasheninnikov's research[42] is lower than ours. The reason could be that their impact zone is larger than ours. In their simulations, the nanotubes outside of contact zone is also bombarded by ions. Although in the contact zone the structure could hold

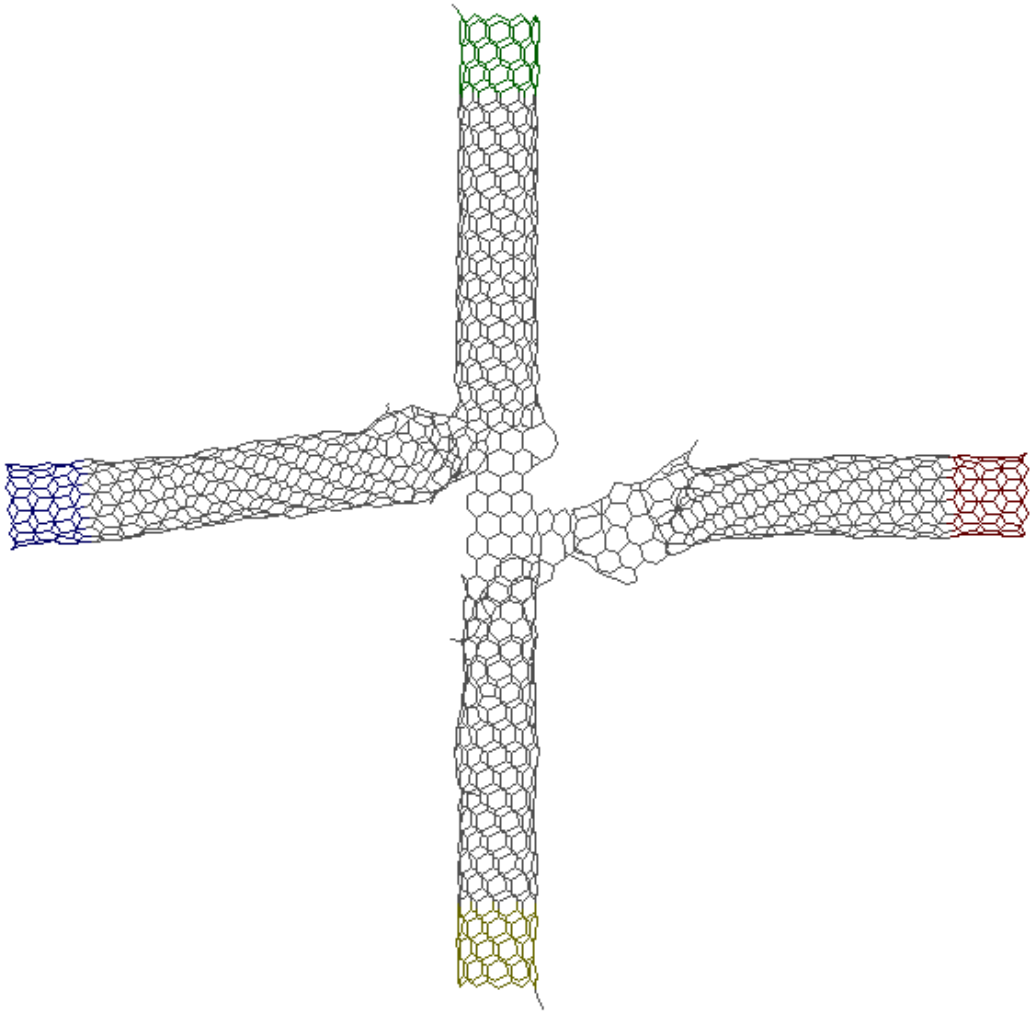

Figure 3.40 Carbon nanotube junction between (10,0)/(10,0) nanotubes after 10 impacts at 1010 eV. The four terminals used in the conductivity calculation are labeled in different colors. Terminals 1, 2, 3, 4 are shown in red, blue, green and yellow, respectively.

together due to two nanotubes, the area with only one nanotube is easy to be badly damaged by the same dose as shown in ref.[42]. That may be why they recommend a lower dose than in our research. If the ion irradiation can be focused in the contact zone, our recommended dose is appropriate. If a larger area including single nanotube is irradiated, a lower value as in Krasheninnikov's research may be better. Still the dose in this research is in the same order of magnitude as in their research.

With different combination of nanotubes investigated in this research, we did not observe any favorable trend in nanotube welding. Being chiral, zigzag or armchair

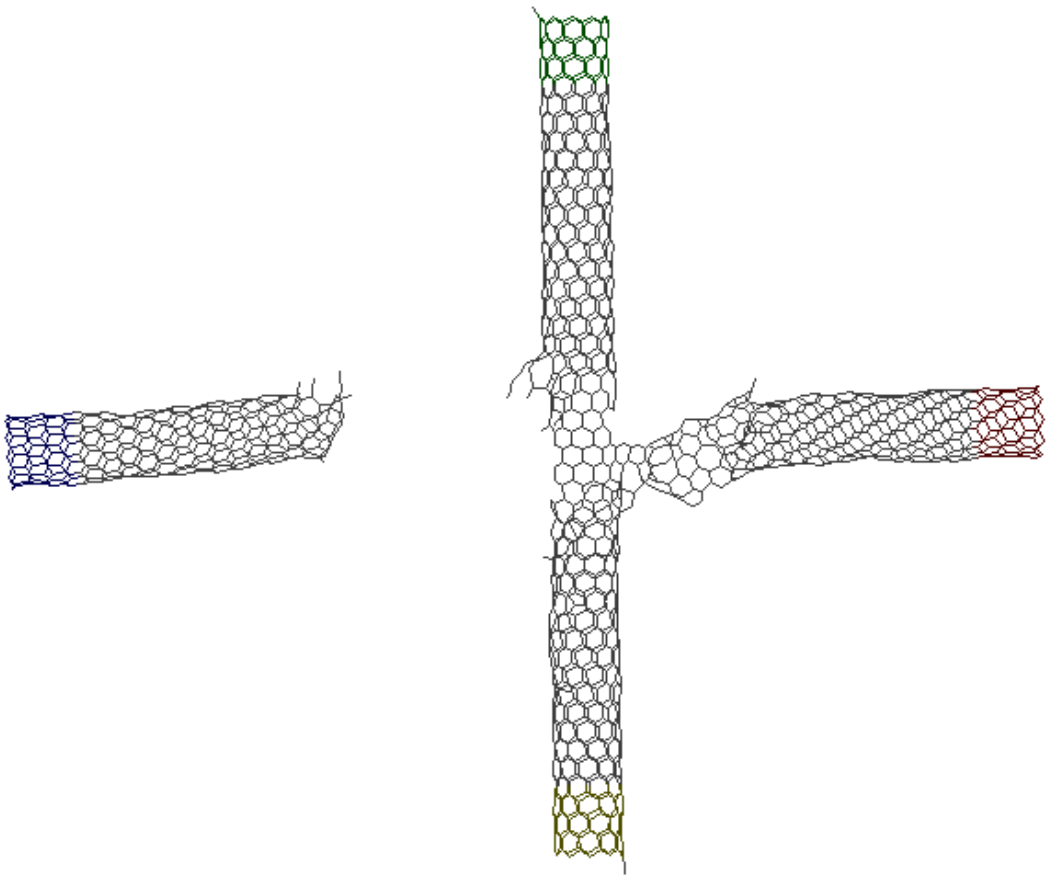

Figure 3.41 Carbon nanotube junction between (10,0)/(10,0) nanotubes after 11 impacts at 1010 eV. The four terminals used in the conductivity calculation are labeled in different colors. Terminals 1, 2, 3, 4 are shown in red, blue, green and yellow, respectively.

nanotubes seems to have little effect on how easy or difficult it is to form junction. In the figures of crosslinks for different combinations of nanotubes at different energies(Figures 3.11 through 3.15), all small nanotube combinations has similar behavior. The number of crosslinks is in a small range with no favor to any particular structure. The same is true for large nanotube combinations. The primary determining factors in junction formation are the energy and fluence of impact ions. Simulations of (5,5)/(5,5) and (10,0)/(10,0) did not show the trend suggested in Sinnott's reserach[41].

A comparison of longer relaxing and cooling periods reveals that at lower energies (186 eV and 330 eV), a significant increase of cross-links is observed. But at high energies (742 eV), it cannot prevent the nanotube system from being disassembled.

Our simulations show that cross-tube conductivity can be achieved by nanotube welding using ion irradiation. The structure of the nanotube intersection is crucial to its conductivity. Too much damage in the nanotube structure will cause significant loss of conductivity.

The AIREBO potential is used in this research instead of the REBO potential. One major difference between these two potentials is that AIREBO potential includes intermolecular interaction. Although intermolecular interaction may not be significant during an energetic process, such as ion particles colliding with a nanotube, it will have an effect in the long process of defect evolution and nanotube structure recovery after initial impact. A better description of intermolecular force is helpful to simulation. The new AIREBO potential with adaptive treatment of van der Waals interaction will have an even more accurate description of intermolecular interactions. During the junction formation, the chemical environment of carbons changes with bond breaking and bond forming. A lot of intermediate states could happen during this process. With the new parameter sets, the new AIREBO potential is expected to perform better than the old AIREBO potential.

Appendix

LENNARD-JONES FORM CALCULATION

Lennard-Jones Interaction Between Atoms i And j, V_{ij}

The Lennard-Jones contribution to the total energy for atom pair i-j in the AIREBO potential is given by

$$\begin{aligned} E_{ij}^{LJ} &= S(t_r(r_{ij}))S(t_b(b_{ij}))C_{ij}V_{ij} + [1 - S(t_r(r_{ij}))]C_{ij}V_{ij} \\ &= \{S(t_r(r_{ij}))S(t_b(b_{ij})) + [1 - S(tr(r_{ij}))]\}C_{ij}V_{ij} \\ &= \{S(t_r(r_{ij}))[S(t_b(b_{ij})) - 1] + 1\}C_{ij}V_{ij} \end{aligned} \tag{A.1}$$

where

$$S(t) = \Theta(-t) + \Theta(t)\Theta(1-t)[1 - t^2(3-2t)] \tag{A.2}$$

is a switching function characterized by ranges

$$t_r(r_{ij}) = \frac{r_{ij} - r_{ij}^{LJmin}}{r_{ij}^{LJmax} - r_{ij}^{LJmin}} \tag{A.3}$$

for the bond length and

$$t_b(b_{ij}) = \frac{b_{ij} - b_{ij}^{min}}{b_{ij}^{max} - r_{ij}^{min}} \tag{A.4}$$

for the bond order.

$$\begin{aligned} C_{ij} &= 1 - \max\{\omega_{ij}(r_{ij}), \\ &\quad \omega_{ik}(r_{ik})\omega_{kl}(r_{kl}), \forall k \\ &\quad \omega_{ik}(r_{ik})\omega_{kl}(r_{kl})\omega_{lj}(r_{lj}), \forall k, l\} \end{aligned} \tag{A.5}$$

is the bond weight, if the atoms i and j are not connected by two or fewer intermediate atoms

The traditional Lennard-Jones form is

$$V_{ij} = 4\epsilon_{ij}[(\frac{\sigma_{ij}}{r_{ij}})^{12} - (\frac{\sigma_{ij}}{r_{ij}})^{12}] \tag{A.6}$$

From the Lorentz-Berthelot combining rules, the heterogeneous parameters, σ_{ij} and ϵ_{ij}, are determined by

$$\epsilon_{ij} = (\epsilon_i \epsilon_j)^{\frac{1}{2}} \tag{A.7}$$

$$\sigma_{ij} = \frac{(\sigma_i + \sigma_j)}{2} \tag{A.8}$$

the distance between i and j is

$$r_{ij} = \sqrt{(x_i - x_j)^2 + (y_i - y_j)^2 + (z_i - z_j)^2)} \tag{A.9}$$

Derivative of E_{ij}^{LJ} With Respect To x_i

Taking the derivative of Eq.(A.1) with respect to a one-dimensional coordinate of atom i gives

$$\begin{aligned}
\frac{\partial E_{ij}^{LJ}}{\partial x_i} &= \{S(t_r(r_{ij}))[S(t_b(b_{ij})) - 1] + 1\} C_{ij} \frac{\partial V_{ij}}{\partial x_i} \\
&+ \{S(t_r(r_{ij}))[S(t_b(b_{ij})) - 1] + 1\} V_{ij} \frac{\partial C_{ij}}{\partial x_i} \\
&+ \frac{\partial S(t_r(r_{ij}))}{\partial x_i} [S(t_b(b_{ij})) - 1] C_{ij} V_{ij} \\
&+ S(t_r(r_{ij})) \frac{\partial S(t_b(b_{ij}))}{\partial x_i} C_{ij} V_{ij}
\end{aligned} \tag{A.10}$$

Derivative of V_{ij} with respect to x_i

$$\frac{\partial V_{ij}}{\partial x_i} = \frac{\partial V_{ij}}{\partial \epsilon_{ij}} \frac{\partial \epsilon_{ij}}{\partial x_i} + \frac{\partial V_{ij}}{\partial \sigma_{ij}} \frac{\partial \sigma_{ij}}{\partial x_i} + \frac{\partial V_{ij}}{\partial r_{ij}} \frac{\partial r_{ij}}{\partial x_i} \tag{A.11}$$

The following equations are detailed explainations of the above equation.

The first term $\frac{\partial V_{ij}}{\partial \epsilon_{ij}} \frac{\partial \epsilon_{ij}}{\partial x_i}$

From Eq.(A.6)

$$\frac{\partial V_{ij}}{\partial \epsilon_{ij}} = 4[(\frac{\sigma_{ij}}{r_{ij}})^{12} - (\frac{\sigma_{ij}}{r_{ij}})^6] \tag{A.12}$$

From Eq.(A.7)

$$\frac{\partial \epsilon_{ij}}{\partial x_i} = \frac{\partial \epsilon_{ij}}{\partial \epsilon_i} \frac{\partial \epsilon_i}{\partial x_i} \tag{A.13}$$

The first term in Eq.(A.13)

$$\frac{\partial \epsilon_{ij}}{\partial \epsilon_i} = \frac{1}{2} (\frac{\epsilon_j}{\epsilon_i})^{\frac{1}{2}} \tag{A.14}$$

In the new potential, the LJ well depth depends on the coordination numbers N_{ij}^C and N_{ij}^H, so the second term in Eq.(A.13)

$$\frac{\partial \epsilon_i}{\partial x_i} = \frac{\partial \epsilon_i}{\partial N_i^C}\frac{\partial N_i^C}{\partial x_i} + \frac{\partial \epsilon_i}{\partial N_i^H}\frac{\partial N_i^H}{\partial x_i} \tag{A.15}$$

where

$$N_i^C = (\sum_{k \neq i} \delta_{kC} W_{ik}(r_{ik})) - \delta_{jC} W_{ij}(r_{ij}) \tag{A.16}$$

is the carbon-only coordination numbers, and

$$N_i^H = (\sum_{k \neq i} \delta_{kH} W_{ik}(r_{ik})) - \delta_{jH} W_{ij}(r_{ij}) \tag{A.17}$$

is the hydrogen-only coordination numbers.

$W_{ik}(r_{ik})$ is a switching function for REBO interactions.

δ_{ij} represents a Kronecker delta

$\frac{\partial \epsilon_i}{\partial N_i^C}$ $\frac{\partial \epsilon_i}{\partial N_i^H}$ can be derived from bicubic spline

From Eq.(A.16) and Eq.(A.17), $\frac{\partial N_i^C}{\partial x_i}$ and $\frac{\partial N_i^H}{\partial x_i}$ in Eq.(A.15) can be calculated

$$\frac{\partial N_i^C}{\partial x_i} = \sum_{k=C} \frac{\partial N_i^C}{\partial r_{ik}}\frac{\partial r_{ik}}{\partial x_i} \tag{A.18}$$

$$\frac{\partial N_i^H}{\partial x_i} = \sum_{k=H} \frac{\partial N_i^H}{\partial r_{ik}}\frac{\partial r_{ik}}{\partial x_i} \tag{A.19}$$

$$\frac{\partial N_i^H}{\partial r_{ik}} = \frac{\partial W_{ik}}{\partial r_{ik}}\delta_{kH} \tag{A.20}$$

$$\frac{\partial N_i^C}{\partial r_{ik}} = \frac{\partial W_{ik}}{\partial r_{ik}}\delta_{kC} \tag{A.21}$$

Replacing j with k in Eq.(A.9) leads to derivative

$$\frac{\partial r_{ik}}{\partial x_i} = \frac{(x_i - x_k)}{r_{ik}} \tag{A.22}$$

The second item in Eq.(A.11) $\frac{\partial V_{ij}}{\partial \sigma_{ij}}\frac{\partial \sigma_{ij}}{\partial x_i}$:

$$\frac{\partial V_{ij}}{\partial \sigma_{ij}} = 4\epsilon_{ij}(\frac{12\sigma_{ij}^{11}}{r_{ij}^{12}} - \frac{6\sigma_{ij}^{5}}{r_{ij}^{6}}) \tag{A.23}$$

From Eq.(A.8)

$$\frac{\partial \sigma_{ij}}{\partial x_i} = \frac{\partial \sigma_{ij}}{\partial \sigma_i}\frac{\partial \sigma_i}{\partial x_i} \tag{A.24}$$

$$\frac{\partial \sigma_{ij}}{\partial \sigma_i} = \frac{1}{2} \tag{A.25}$$

$$\frac{\partial \sigma_i}{\partial x_i} = \frac{\partial \sigma_i}{\partial N_i^C}\frac{\partial N_i^C}{\partial x_i} + \frac{\partial \sigma_i}{\partial N_i^H}\frac{\partial N_i^H}{\partial x_i} \tag{A.26}$$

$\frac{\partial \sigma_i}{\partial N_i^C}$ $\frac{\partial \sigma_i}{\partial N_i^H}$ can be derived from bicubic spline.
$\frac{\partial N_i^C}{\partial x_i}$ and $\frac{\partial N_i^H}{\partial x_i}$ are given in Eq.(A.18) and Eq.(A.19).
The third term in Eq.(A.11) $\frac{\partial V_{ij}}{\partial r_{ij}}\frac{\partial r_{ij}}{\partial x_i}$:

$$\frac{\partial V_{ij}}{\partial r_{ij}} = 4\epsilon_{ij}\left(\frac{(-12)\sigma_{ij}^{12}}{r_{ij}^{13}} - \frac{(-6)\sigma_{ij}^{6}}{r_{ij}^{7}}\right) \tag{A.27}$$

$$\frac{\partial r_{ij}}{\partial x_i} = \frac{(x_i - x_j)}{r_{ij}} \tag{A.28}$$

Derivative of V_{ij} With Respect To x_j

$$\frac{\partial V_{ij}}{\partial x_j} = \frac{\partial V_{ij}}{\partial \epsilon_{ij}}\frac{\partial \epsilon_{ij}}{\partial x_j} + \frac{\partial V_{ij}}{\partial \sigma_{ij}}\frac{\partial \sigma_{ij}}{\partial x_j} + \frac{\partial V_{ij}}{\partial r_{ij}}\frac{\partial r_{ij}}{\partial x_j} \tag{A.29}$$

Followings are each term of the above equation.

$$\frac{\partial V_{ij}}{\partial \epsilon_{ij}} = 4[(\frac{\sigma_{ij}}{r_{ij}})^{12} - (\frac{\sigma_{ij}}{r_{ij}})^{6}] \tag{A.30}$$

$$\frac{\partial \epsilon_{ij}}{\partial x_j} = \frac{\partial \epsilon_{ij}}{\partial \epsilon_j}\frac{\partial \epsilon_j}{\partial x_j} \tag{A.31}$$

$$\frac{\partial \epsilon_{ij}}{\partial \epsilon_j} = \frac{1}{2}(\frac{\epsilon_i}{\epsilon_j})^{\frac{1}{2}} \tag{A.32}$$

$$\frac{\partial \epsilon_j}{\partial x_j} = \frac{\partial \epsilon_j}{\partial N_j^C}\frac{\partial N_j^C}{\partial x_j} + \frac{\partial \epsilon_j}{\partial N_j^H}\frac{\partial N_j^H}{\partial x_j} \tag{A.33}$$

where

$$N_j^C = (\sum_{l \neq j} \delta_{lC} W_{jl}(r_{jl})) - \delta_{jC} W_{jj}(r_{jj}) \tag{A.34}$$

is the carbon-only coordination numbers, and

$$N_j^H = (\sum_{l \neq j} \delta_{lH} W_{jl}(r_{jl})) - \delta_{jH} W_{jj}(r_{jj}) \tag{A.35}$$

is the hydrogen-only coordination numbers

$\frac{\partial \epsilon_j}{\partial N_j^C}$ $\frac{\partial \epsilon_j}{\partial N_j^H}$ can be derived from bicubic spline

$$\frac{\partial N_j^C}{\partial x_j} = \sum_{l=C} \frac{\partial N_j^C}{\partial r_{jl}} \frac{\partial r_{jl}}{\partial x_j} \tag{A.36}$$

$$\frac{\partial N_j^H}{\partial x_j} = \sum_{l=H} \frac{\partial N_j^H}{\partial r_{jl}} \frac{\partial r_{jl}}{\partial x_j} \tag{A.37}$$

$$\frac{\partial N_j^H}{\partial r_{jl}} = \frac{\partial W_{jl}}{\partial r_{jl}} \delta_{lH} \tag{A.38}$$

$$\frac{\partial N_j^C}{\partial r_{jl}} = \frac{\partial W_{jl}}{\partial r_{jl}} \delta_{lC} \tag{A.39}$$

$$\frac{\partial r_{jl}}{\partial x_j} = \frac{(x_j - x_l)}{r_{jl}} \tag{A.40}$$

The second item in Eq.(A.29):

$$\frac{\partial V_{ij}}{\partial \sigma_{ij}} = 4\epsilon_{ij}(\frac{12\sigma_{ij}^{11}}{r_{ij}^{12}} - \frac{6\sigma_{ij}^{5}}{r_{ij}^{6}}) \tag{A.41}$$

$$\frac{\partial \sigma_{ij}}{\partial x_j} = \frac{\partial \sigma_{ij}}{\partial \sigma_j} \frac{\partial \sigma_j}{\partial x_j} \tag{A.42}$$

$$\frac{\partial \sigma_{ij}}{\partial \sigma_j} = \frac{1}{2} \tag{A.43}$$

$$\frac{\partial \sigma_j}{\partial x_j} = \frac{\partial \sigma_j}{\partial N_j^C}\frac{\partial N_j^C}{\partial x_j} + \frac{\partial \sigma_j}{\partial N_j^H}\frac{\partial N_j^H}{\partial x_j} \tag{A.44}$$

$\frac{\partial \sigma_j}{\partial N_j^C}$ $\frac{\partial \sigma_j}{\partial N_j^H}$ can be derived from bicubic spline. $\frac{\partial N_j^C}{\partial x_j}$ and $\frac{\partial N_j^H}{\partial x_j}$ are given in Eq.(A.36) and Eq.(A.37).

The third term:

$$\frac{\partial V_{ij}}{\partial r_{ij}} = 4\epsilon_{ij}\left(\frac{(-12)\sigma_{ij}^{12}}{r_{ij}^{13}} - \frac{(-6)\sigma_{ij}^{6}}{r_{ij}^{7}}\right) \tag{A.45}$$

$$\frac{\partial r_{ij}}{\partial x_j} = \frac{(x_j - x_i)}{r_{ij}} \tag{A.46}$$

Derivative of V_{ij} With Respect To x_l

$$\frac{\partial V_{ij}}{\partial x_l} = \frac{\partial V_{ij}}{\partial \epsilon_{ij}}\frac{\partial \epsilon_{ij}}{\partial x_l} + \frac{\partial V_{ij}}{\partial \sigma_{ij}}\frac{\partial \sigma_{ij}}{\partial x_l} + \frac{\partial V_{ij}}{\partial r_{ij}}\frac{\partial r_{ij}}{\partial x_l} \tag{A.47}$$

Followings are each term of the above equation.

$$\frac{\partial V_{ij}}{\partial \epsilon_{ij}} = 4\left[\left(\frac{\sigma_{ij}}{r_{ij}}\right)^{12} - \left(\frac{\sigma_{ij}}{r_{ij}}\right)^{6}\right] \tag{A.48}$$

$$\frac{\partial \epsilon_{ij}}{\partial x_l} = \frac{\partial \epsilon_{ij}}{\partial \epsilon_j}\frac{\partial \epsilon_j}{\partial x_l} \tag{A.49}$$

$$\frac{\partial \epsilon_{ij}}{\partial \epsilon_j} = \frac{1}{2}\left(\frac{\epsilon_i}{\epsilon_j}\right)^{\frac{1}{2}} \tag{A.50}$$

$$\frac{\partial \epsilon_j}{\partial x_l} = \frac{\partial \epsilon_j}{\partial N_j^C}\frac{\partial N_j^C}{\partial x_l} + \frac{\partial \epsilon_j}{\partial N_j^H}\frac{\partial N_j^H}{\partial x_l} \tag{A.51}$$

$\frac{\partial \epsilon_j}{\partial N_j^C}$ $\frac{\partial \epsilon_j}{\partial N_j^H}$ can be derived from bicubic spline

$$\frac{\partial N_j^C}{\partial x_l} = \frac{\partial N_j^C}{\partial r_{jl}}\frac{\partial r_{jl}}{\partial x_l} \tag{A.52}$$

$$\frac{\partial N_j^H}{\partial x_l} = \frac{\partial N_j^H}{\partial r_{jl}}\frac{\partial r_{jl}}{\partial x_l} \tag{A.53}$$

$$\frac{\partial N_j^H}{\partial r_{jl}} = \frac{\partial W_{jl}}{\partial r_{jl}} \delta_{lH} \tag{A.54}$$

$$\frac{\partial N_j^C}{\partial r_{jl}} = \frac{\partial W_{jl}}{\partial r_{jl}} \delta_{lC} \tag{A.55}$$

$$\frac{\partial r_{jl}}{\partial x_l} = \frac{(x_l - x_j)}{r_{jl}} \tag{A.56}$$

The second item:

$$\frac{\partial V_{ij}}{\partial \sigma_{ij}} = 4\epsilon_{ij}\left(\frac{12\sigma_{ij}^{11}}{r_{ij}^{12}} - \frac{6\sigma_{ij}^{5}}{r_{ij}^{6}}\right) \tag{A.57}$$

$$\frac{\partial \sigma_{ij}}{\partial x_l} = \frac{\partial \sigma_{ij}}{\partial \sigma_j} \frac{\partial \sigma_j}{\partial x_l} \tag{A.58}$$

$$\frac{\partial \sigma_{ij}}{\partial \sigma_j} = \frac{1}{2} \tag{A.59}$$

$$\frac{\partial \sigma_j}{\partial x_l} = \frac{\partial \sigma_j}{\partial N_j^C} \frac{\partial N_j^C}{\partial x_l} + \frac{\partial \sigma_j}{\partial N_j^H} \frac{\partial N_j^H}{\partial x_l} \tag{A.60}$$

$\frac{\partial \sigma_j}{\partial N_j^C}$ $\frac{\partial \sigma_j}{\partial N_j^H}$ can be derived from bicubic spline.
$\frac{\partial N_j^C}{\partial x_l}$ and $\frac{\partial N_j^H}{\partial x_l}$ are given in Eq.(A.52) and Eq.(A.53).

The third term:

$$\frac{\partial V_{ij}}{\partial r_{ij}} = 4\epsilon_{ij}\left(\frac{(-12)\sigma_{ij}^{12}}{r_{ij}^{13}} - \frac{(-6)\sigma_{ij}^{6}}{r_{ij}^{7}}\right) \tag{A.61}$$

$$\frac{\partial r_{ij}}{\partial x_l} = 0 \tag{A.62}$$

Derivative of V_{ij} With Respect To x_k

x_k is a neighbor of i.

$$\frac{\partial V_{ij}}{\partial x_k} = \frac{\partial V_{ij}}{\partial \epsilon_{ij}} \frac{\partial \epsilon_{ij}}{\partial x_k} + \frac{\partial V_{ij}}{\partial \sigma_{ij}} \frac{\partial \sigma_{ij}}{\partial x_k} + \frac{\partial V_{ij}}{\partial r_{ij}} \frac{\partial r_{ij}}{\partial x_k} \tag{A.63}$$

Followings are the each term of the above equation.

$$\frac{\partial V_{ij}}{\partial \epsilon_{ij}} = 4[(\frac{\sigma_{ij}}{r_{ij}})^{12} - (\frac{\sigma_{ij}}{r_{ij}})^{6}] \tag{A.64}$$

$$\frac{\partial \epsilon_{ij}}{\partial x_k} = \frac{\partial \epsilon_{ij}}{\partial \epsilon_i}\frac{\partial \epsilon_i}{\partial x_k} \tag{A.65}$$

$$\frac{\partial \epsilon_{ij}}{\partial \epsilon_i} = \frac{1}{2}(\frac{\epsilon_j}{\epsilon_i})^{\frac{1}{2}} \tag{A.66}$$

$$\frac{\partial \epsilon_i}{\partial x_k} = \frac{\partial \epsilon_i}{\partial N_i^C}\frac{\partial N_i^C}{\partial x_k} + \frac{\partial \epsilon_i}{\partial N_i^H}\frac{\partial N_i^H}{\partial x_k} \tag{A.67}$$

$\frac{\partial \epsilon_i}{\partial N_i^C}$ $\frac{\partial \epsilon_i}{\partial N_i^H}$ can be derived from bicubic spline

$$\frac{\partial N_i^C}{\partial x_k} = \frac{\partial N_i^C}{\partial r_{ik}}\frac{\partial r_{ik}}{\partial x_k} \tag{A.68}$$

$$\frac{\partial N_i^H}{\partial x_k} = \frac{\partial N_i^H}{\partial r_{ik}}\frac{\partial r_{ik}}{\partial x_k} \tag{A.69}$$

$$\frac{\partial N_i^H}{\partial r_{ik}} = \frac{\partial W_{ik}}{\partial r_{ik}}\delta_{kH} \tag{A.70}$$

$$\frac{\partial N_i^C}{\partial r_{ik}} = \frac{\partial W_{ik}}{\partial r_{ik}}\delta_{kC} \tag{A.71}$$

$$\frac{\partial r_{ik}}{\partial x_k} = \frac{(x_k - x_i)}{r_{ik}} \tag{A.72}$$

The second item:

$$\frac{\partial V_{ij}}{\partial \sigma_{ij}} = 4\epsilon_{ij}(\frac{12\sigma_{ij}^{11}}{r_{ij}^{12}} - \frac{6\sigma_{ij}^{5}}{r_{ij}^{6}}) \tag{A.73}$$

$$\frac{\partial \sigma_{ij}}{\partial x_k} = \frac{\partial \sigma_{ij}}{\partial \sigma_i}\frac{\partial \sigma_i}{\partial x_k} \tag{A.74}$$

$$\frac{\partial \sigma_{ij}}{\partial \sigma_i} = \frac{1}{2} \tag{A.75}$$

$$\frac{\partial \sigma_i}{\partial x_k} = \frac{\partial \sigma_i}{\partial N_i^C}\frac{\partial N_i^C}{\partial x_k} + \frac{\partial \sigma_i}{\partial N_i^H}\frac{\partial N_i^H}{\partial x_k} \tag{A.76}$$

$\frac{\partial \boldsymbol{\sigma}_i}{\partial N_i^C}$ $\frac{\partial \boldsymbol{\sigma}_i}{\partial N_i^H}$ can be derived from bicubic spline.

$\frac{\partial N_i^C}{\partial x_k}$ and $\frac{\partial N_i^H}{\partial x_k}$ are given in Eq.(A.68) and Eq.(A.69).

The third term:

$$\frac{\partial V_{ij}}{\partial r_{ij}} = 4\epsilon_{ij}\left(\frac{(-12)\sigma_{ij}^{12}}{r_{ij}^{13}} - \frac{(-6)\sigma_{ij}^{6}}{r_{ij}^{7}}\right) \tag{A.77}$$

$$\frac{\partial r_{ij}}{\partial x_k} = 0 \tag{A.78}$$

BIBLIOGRAPHY

[1] Stuart, S. J., Tutein, A. B., and Harrison, J. A., A Reactive Potential for Hydrocarbons with Intermolecular Interactions, *J. Chem. Phys.*, **112**:6472–6486 (2000).

[2] Habenschuss, A., Johnson, E., and Narten, A. H., X-ray diffraction study and models of liquid methane at 92 K, *J. Chem. Phys.*, **74**:5234–5241 (1981).

[3] Narten, A. H., X-ray diffraction pattern and models of liquid benzene, *J. Chem. Phys.*, **67**:2102–2108 (1977).

[4] Sandler, S. I., Lombardo, M. G., Wong, D. S.-H., Habenschuss, A., and Narten, A. H., X-ray diffraction study and models of liquid ethane at 105 and 181 K, *J. Chem. Phys.*, **77**:2144–2152 (1982).

[5] Tersoff, J., New empirical approach for the structure and energy of covalent systems, *Phys. Rev. B*, **37**:6991–7000 (1988).

[6] Tersoff, J., Modeling solid-state chemistry: Interatomic potentials for multicomponent systems, *Phys. Rev. B*, **39**:5566–5568 (1989).

[7] Daw, M. S. and Baskes, M. I., Embedded-atom method: Derivation and application to impurities, surfaces, and other defects in metals, *Phys. Rev. B*, **29**:6443–6453 (1984).

[8] Tersoff, J., Empirical Interatomic Potential for Carbon, with Applications to Amorphous Carbon, *Phys. Rev. Lett.*, **61**:2879–2882 (1988).

[9] Brenner, D. W., Shenderova, O. A., Harrison, J. A., Stuart, S. J., Ni, B., and Sinnott, S., A second-generation reactive empirical bond order (REBO) potential energy expression for hydrocarbons, *J. Phys.: Condens. Matter*, **14**:783–802 (2002).

[10] Pettifor, D. G. and Oleinik, I. I., Analytic bond-order potentials beyond Tersoff-Brenner. I. Theory, *Phys. Rev. B*, **59**:8487–8499 (1999).

[11] Oleinik, I. I. and Pettifor, D. G., Analytic bond-order potentials beyond Tersoff-Brenner. II. Application to the hydrocarbons, *Phys. Rev. B*, **59**:8500–8507 (1999).

[12] Harrison, J. A., Stuart, S. J., Robertson, D. H., and White, C. T., Properties of Capped Nanotubes When Used as SPM Tips, *J. Phys. Chem. B*, **101**:9682–9685 (1997).

[13] Perry, M. D. and Harrison, J. A., Molecular Dynamics Studies of the Frictional Properties of Hydrocarbon Materials, *Langmuir*, **12**:4552–4556 (1996).

[14] Brenner, D. W., Harrison, J. A., White, C. T., and Colton, R. J., Molecular dynamics simulations of the nanometer-scale mechanical properties of compressed Buckminsterfullerene, *Thin Solid Films*, **206**:220–223 (1991).

[15] Mikulski P.T, H. J., Packing-density effects on the friction of n-alkane monolayers, *J. Am. Chem. Soc.*, **123**:6873–6881 (2001).

[16] Stuart S.J, Knippenberg M.T, K. O., Simulation of amorphous carbon with a bond-order potential, *PHYSICA SCRIPTA*, **124**:58–64 (2006).

[17] Cheng H.S, Cooper A.C, P. G., Molecular dynamics simulations on the effects of diameter and chirality on hydrogen adsorption in single walled carbon nanotubes, *J. Phys. Chem. B*, **109**:3780–3786 (2005).

[18] Lennard-Jones, J. E., Cohesion, *Proceedings of the Physical Society*, **43**:461–482 (1931).

[19] Iijima, S., Helical microtubules of graphitic carbon, *Nature*, **354**:56 (1991).

[20] Iijima, S. and Ichihashi, T., Single-shell carbon nanotubes of 1-nm diameter, *Nature*, **363**:603–604 (1993).

[21] Bethune D.S, Klang C.H, V. M., Cobalt-catalysed growth of carbon nanotubes with single-atomic-layer walls, *Nature*, **363**:605–606 (1993).

[22] Saito, R., Fujita, M., Dresselhaus, G., and Dresselhaus, M. S., Electronic structure of chiral graphene tubules, *Appl. Phys. Lett.*, **60**:2204 (1992).

[23] Halgren, T. A., Merck Molecular Force Field. II. MMFF94 van der Waals and Electrostatic Parameters for Intermolecular Interactions, *J. Comput. Chem.*, **17**:520–552 (1996).

[24] Taylor, R. S. and Garrison, B. J., Molecular Dynamics Simulations of Reactions between Molecules: High-Energy Particle Bombardment of Organic Films, *Langmuir*, **11**:1220–1228 (1995).

[25] Brooks, B. R., Bruccoleri, R. E., Olafson, B. D., States, D. J., Swaminathan, S., and Karplus, M., CHARMM: A program for macromolecular energy, minimization, and dynamics calculations, *J. Comput. Chem.*, **4**:187–217 (1983).

[26] Rappe, A. K., Casewit, C. J., Colwell, K. S., Goddard, W. A., and Skiff, W. M., UFF, a Full Periodic Table Force Field for Molecular Mechanics and Molecular Dynamics Simulations, *J. Am. Chem. Soc.*, **114**:10024 (1992).

[27] Cornell, W. D., Cieplak, P., and etc, C. I. B., A Second Generation Force Field for the Simulation of Proteins, Nucleic Acids, and Organic Molecules, *J. Am. Chem. Soc.*, **117**:5179 (1995).

[28] Allinger, N. L., Yuh, Y. H., and Lii, J.-H., Molecular mechanics. The MM3 force field for hydrocarbons, *J. Am. Chem. Soc.*, **111**:8551C8566 (1989).

[29] Sun, H. and Rigby, D., Polysiloxanes: ab initio force field and structural, conformational and thermophysical properties, *Spectrochim. Acta A*, **53**:1301–1323 (1997).

[30] Sun, H., COMPASS: An ab Initio Force Field Optimized for Condensed-Phase Applications " Overview with Details on Alkane and Benzene Compounds, *J. Phys. Chem. B*, **102**:7338–7364 (1998).

[31] Hudson, G. H. and McCoubrey, J. C., Intermolecular Forces between Unlike Molecules. A More Complete Form of the Combining Rules, *Trans. Faraday Soc.*, **56**:761–766 (1959).

[32] Press, W. H., Flannery, B. P., Teukolsky, S. A., and Vetterling, W. T., *Numerical Recipes*, Cambridge University Press, Cambridge, 1986.

[33] Adelman, S. A. and Doll, J. D., Generalized Langevin equation approach for atom/solid-surface scattering: General formulation for classical scattering off harmonic solids, *J. Chem. Phys.*, **64**:2375–2388 (1976).

[34] Allen, M. P. and Tildesley, D. J., *Computer Simulation of Liquids*, Oxford University Press, London, 1987.

[35] Lide, D. R., editor, *CRC Handbook of Chemistry and Physics*, Chemical Rubber, Boca Raton, 2004.

[36] Dean, J., editor, *Lange's Handbook of Chemistry*, McGraw-Hill, 1999.

[37] Majer, V. and Svoboda, V., *Enthalpies of Vaporization of Organic Compounds: A Critical Review and Data Compilation*, Blackwell Scientific Publications, Oxford, 1985.

[38] Terrones, M., Banhart, F., Grobert, N., Charlier, J.-C., Terrones, H., and Ajayan, P. M., Molecular Junctions by Joining Single-Walled Carbon Nanotubes, *Phys. Rev. Lett.*, **89**:075505 (2002).

[39] Banhart, F., The Formation of a Connection between Carbon Nanotubes in an Electron Beam, *Nano Lett.*, **1**:329–332 (2001).

[40] Ni, B., Andrews, R., Jacques, D., Qian, D., Wijesundara, M. B. J., Choi, Y., Hanley, L., and Sinnott, S. B., A Combined Computational and Experimental

Study of Ion-Beam Modification of Carbon Nanotube Bundles, *J. Phys. Chem. B*, **105**:12719 (2001).

[41] Jang, I. and Sinnott, S. B., Molecular Dynamics Simulation Study of Carbon Nanotube Welding under Electron Beam Irradiation, *Nano Lett.*, **4**:109–114 (2004).

[42] Krasheninnikov, A. V., Nordlund, K., and Keinonen, J., Ion-irradiation-induced welding of carbon nanotubes, *Phys. Rev. B*, **66**:245403 (2002).

[43] Landauer, R., Spatial variation of currents and fields due to localized scatterers in metallic conduction, *IBM J. Res. Dev.*, **36**:306–316 (1988).

[44] M., N., Electronic transport in extended systems: Application to carbon nanotubes, *Phys. Rev. B*, **60**:7828–7833 (1999).

[45] Meunier V., S. B., Amphoteric doping of carbon nanotubes by encapsulation of organic molecules: Electronic properties and quantum conductance, *J. Chem. Phys.*, **123**:024705 (2005).

[46] Rocquefelte X, Rignanese GM, M. V., How to Identify Haeckelite Structures: A Theoretical Study of Their Electronic and Vibrational Properties, *Nano Lett.*, **4**:805–810 (2004).